A flow-informed strategy for ballistic capture trajectory design

Matteo Manzi

Delft University of Technology

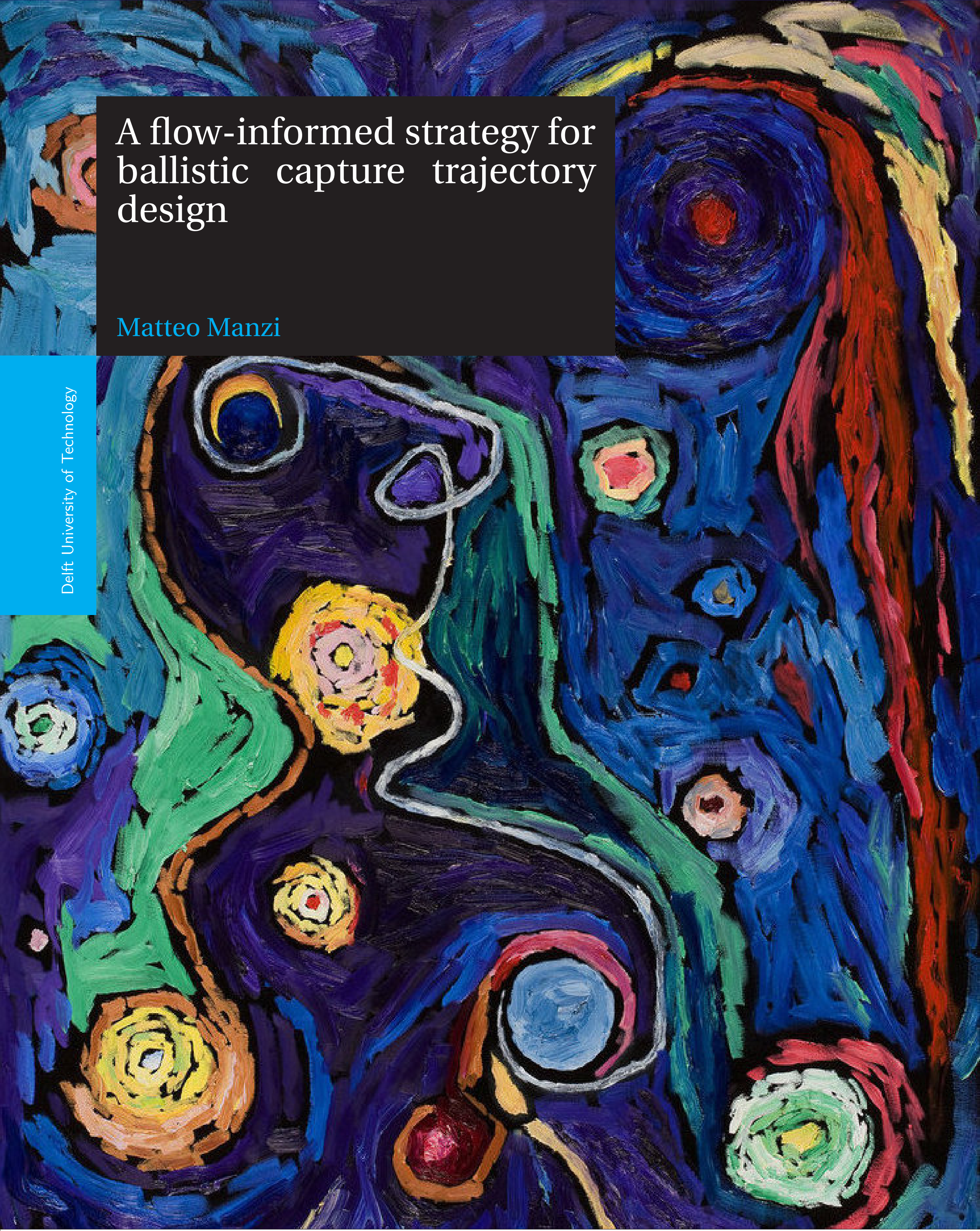

Delft University of Technology

Challenge the future

A FLOW-INFORMED STRATEGY FOR BALLISTIC CAPTURE TRAJECTORY DESIGN

by

Matteo Manzi

in partial fulfillment of the requirements for the degree of

Master of Science
in Aerospace Engineering

at the Delft University of Technology,
to be defended publicly on Thursday, October 31st, 2019

Supervisor:	Prof. dr. F. Topputo
Thesis committee:	Prof. dr. ir. P.N.A.M. Visser
	Dr. M.J. Heiligers
	Dr. S. Speretta

Cover image: Edward Belbruno, Cosmic Orbit, Oil on Canvas, 30 x 40 inches, July 2009

PREFACE

Alla rinnovata forza di mia madre,
al Romano che è in mio padre, quindi in me.

With my brother, remembering to do push-ups...sure, also that "*Hybris* is our whole attitude to nature nowadays, our violation of nature with the help of machinery, and all the unscrupulous ingenuity of our scientists and engineers", but mainly push-ups.

Professore: it has been a real pleasure. Thank you for your inspiring busyness and, at the same time, for your flexibility and patience. Also thank you for welcoming me at PoliMi for the last couple of months: I hope to be able to come back, one day. But first, see you soon, among asteroids and space debris!

Matteo Manzi
Milano, October 2019

Nunquam praescriptos transibunt sidera fines.

Never will heavenly bodies
transgress their prescribed bounds.

Henri Poincaré
1890

CONTENTS

LIST OF FIGURES

LIST OF TABLES

LIST OF ABBREVIATIONS

3D	Three-Dimensional
BME@Epoch	Body Mean Equator Frame at Epoch
CG	Cauchy–Green
(P)CR3BP	(Planar) Circular Restricted Three-Body Problem
EME2000	Earth Mean Equator and Equinox of J2000
EPHE	Full Ephemeris model
ER3BP	Elliptic Restricted 3-Body Problem
ESA	European Space Agency
FILE	Finite-Iteration Lyapunov Exponent
FTLE	Finite-Time Lyapunov Exponent
GNC	Guidance, Navigation and Control
GRATIS	GRAvity TIdal Slide
ICRF	International Celestial Reference Frame
JPL	Jet Propulsion Laboratory
LCS	Lagrange Coherent Structures
LU	Length Unit
NAIF	Navigation and Ancillary Information Facility
NASA	National Aeronautics and Space Administration
NSG	Non-Spherical Gravity
ODE	Ordinary Differential Equation
RK	Runge–Kutta
RnBP	Restricted n-Body Problem
RPRnBP	Roto-pulsating Restricted n-Body Problem
RTN@t_0	Radial-Tangential-Normal frame at epoch t_0
SMART	Small Missions for Advanced Research in Technology
SOI	Sphere of Influence
SRP	Solar Radiation Pressure
STM	State Transition Matrix
TDB	Barycentric Dynamic Time (Temps Dynamique Baricentrique)
TU	Time Unit
TUDAT	TU Delft Astrodynamics Toolbox
UTC	Universal Time Coordinated
WSB	Weak Stability Boundary

List of Symbols

a	Semi-major axis
$\mathcal{C}$	Set of initial conditions that produce capture orbits
C	Jacobi constant
C_R	Reflectivity coefficient
c	Speed of light
$\mathcal{D}$	Set of initial conditions that cannot be classified under $\mathcal{X}$, $\mathcal{K}$, $\mathcal{W}$
e	Eccentricity
e_p	Eccentricity of P_1 and P_2 in the Elliptic Restricted Three-Body Problem
f	True anomaly
i	Inclination
$\mathcal{K}$	Set of initial conditions that produce collision orbits
L_i	Lagrangian points
L_S	Sun luminosity
l	Half-line used in the algorithmic definition of the Stable Set
m	Mass of the spacecraft
n	Number of revolutions
$\mathbf{r}$	Position vector; r denotes its norm
r_0^*	Initial periapsis radius defining a boundary between stability and instability
$\mathcal{R}_c$	Capture Ratio
r_p	Osculating periapsis radius of the spacecraft
R_s	Radius of the sphere of influence
$\mathcal{S}$	Stability index
$\mathcal{S}_{min}$	Minimum value of $\mathcal{S}$ in a given $\mathcal{C}$
$\mathcal{W}$	Weakly stable set of initial conditions
$\mathcal{X}$	Set of initial conditions that produce escape orbits

α	Right Ascension
δ	Declination
ΔV	Impulsive Velocity Increment
$\partial\mathcal{W}$	Weak Stability Boundary
θ	Angle between l and the P_1P_2 line
μ_i	Gravitational parameter of body i
μ	Mass-ratio of the P_1–P_2 system
Φ	State Transition Matrix
$\phi_{t_0}^t$	Flow map
Ω	Right ascension of the ascending node
ω	Argument of periapsis

EXECUTIVE SUMMARY

In interplanetary mission design, ballistic capture is the phenomenon by which a spacecraft approaches its target body, and performs a number of revolutions around it, *without* requiring manoeuvres in between. For a spacecraft to be captured, its gravitational interaction with at least two celestial bodies has to be taken into account. Because of their fail-safe nature (eliminating the possibility of single point failures), their fuel efficiency and their wider launch windows, ballistic capture trajectories are of particular scientific and engineering interest. Capture orbits are characterized by a specific qualitative dynamics, defining almost-invariant regions in a given space, guiding transport phenomena; the introduction of structures, defining and bounding such domains, naturally follows.

Traditionally, the set of initial conditions leading to capture, the *Capture Set*, has been computed by sampling the domain of interest, and hence analysing the forward and backward behaviour of the orbit associated to each sample. The main limitations of this approach reside in its large computational cost and, even for a dense grid, in the non-smooth approximation of the aforementioned boundary regions; the theory of Lagrangian Coherent Structures (LCS) has the potential of overcoming both limitations, allowing at the same time for a more insightful description of the phenomenon. In fact, Lagrangian Coherent Structures identify transport barriers in dynamical systems, separating regions with qualitatively different dynamics. The development of heuristics applicable to ballistic capture trajectory design *and* informed by such theory (i.e. flow-informed) appears desirable.

In this research, different flow-informed approaches are presented and their relations with ballistic capture are discussed: following, a new heuristic, the *Stroboscopic Strainline*, is introduced. This new tool is therefore applied to different case studies at Mars, in order to approximate the capture sets associated to different numbers of revolutions and geometries. While a real-ephemerides model has been used to describe the dynamical environments, different levels of fidelity have been investigated: perturbing forces have been introduced not only to obtain more accurate results, but also to test the robustness of the proposed technique with respect to different features of the underlying dynamical model.

Finally, it is shown how Stroboscopic Strainlines are a good candidate for characterizing the qualitative behaviour of ballistic capture trajectories, both forward and backward in time.

Keywords— Ballistic capture, Weak Stability Boundary, Low-energy transfers, Lagrangian Coherent Structures, Lyapunov exponents

1

INTRODUCTION

1.1. CONTEXT

In astrodynamics, the goal of the trajectory design process is to obtain a solution that satisfies a number of constraints and is, in some sense, the optimal one. The objective is often the minimization of the cost associated to a certain mission, and hence the reduction of the spacecraft propellent necessary to reach its destination; reducing the ΔV associated to a transfer trajectory leads to an exponential reduction of the spacecraft mass and, therefore, of the cost associated to its launch.

While optimization is an important component of the design process, another key aspect is trying to incorporate in the problem definition new features, allowing for new available solutions to arise. It is because of this consideration that the aerospace community is focusing on the exploitation of dynamical nuances of the solar system: aerobraking and solar sailing are, together with low-energy transfers discussed in this work, some examples of new design ingredients made available by the presented approach.

As stated, this work is focused on the application of low-energy transfers in trajectory design: such nomenclature should not be confused with "low-energy propulsion". It simply underlines the low value of the cumulative ΔV associated to the mission phase, without specifying the kind of propulsion used to generate it.

1.1.1. BALLISTIC CAPTURE

A family of low-energy transfer trajectories is given by the ones making use of *ballistic capture*. The phenomenon has been considered for the first time because of extraordinary circumstances. In 1991, the Japanese Hiten mission used a low-energy transfer with a ballistic capture at the Moon, based on the works by Belbruno and Miller (among others, [1]): the spacecraft was not designed to reach the natural satellite, so a standard Hohmann transfer was not feasible in terms of available fuel, and, therefore, ΔV. [2]

Indeed, this kind of low-energy trajectories are characterized by a small velocity w.r.t. the target, and the spacecraft does not have to perform a manoeuvre in its vicinity; while, compared to a Hohmann transfer, travel takes longer (Figure 1.1), ballistic capture orbits are interesting from a space mission design point of view. In fact, making use of more traditional approaches, some designs are excluded in an early stage (mostly because of high ΔV requirements); moreover, in order to deal with the possibility of single point failures, strict robustness requirements have to be satisfied. Ballistic capture orbits are attractive also because of their wider launch windows, since space missions using Hohmann transfers must wait for the Earth alignment with the target body to occur.

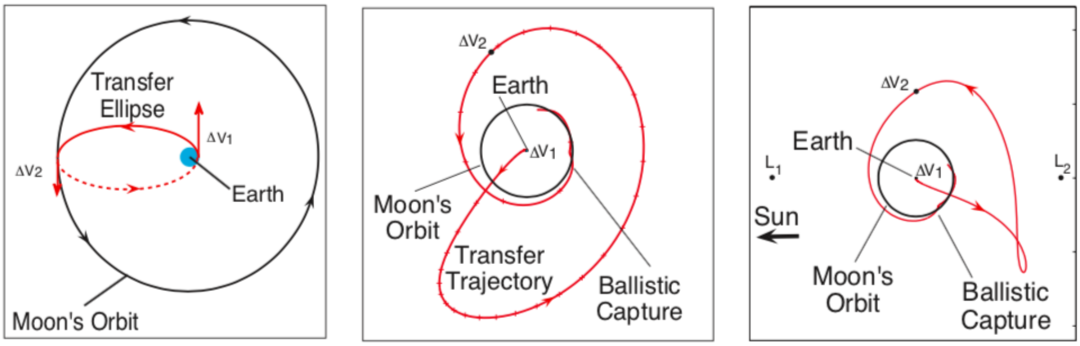

(a) (b) (c)

Figure 1.1: (a) Hohmann transfer. Low-energy transfer in the geocentric inertial frame (b), and in the Sun-Earth rotating frame (c). [3]

Since Hiten, many other missions used ballistic capture; one example is given by SMART-1, the first ESA mission to the Moon (Figure 1.2). A trajectory involving capture was used because the mission could not impose launch window constrains: this underlines the flexibility of such mission design. Also, the risk evaluation of the mission highlighted many positive aspects (e.g., [4]), both before and after capture:

- collision or close encounters with the target body, in the presence of problems with the propulsion system, can be avoided;
- the mission design allows for navigation corrections;
- the absence of single point failures allows for recovery.

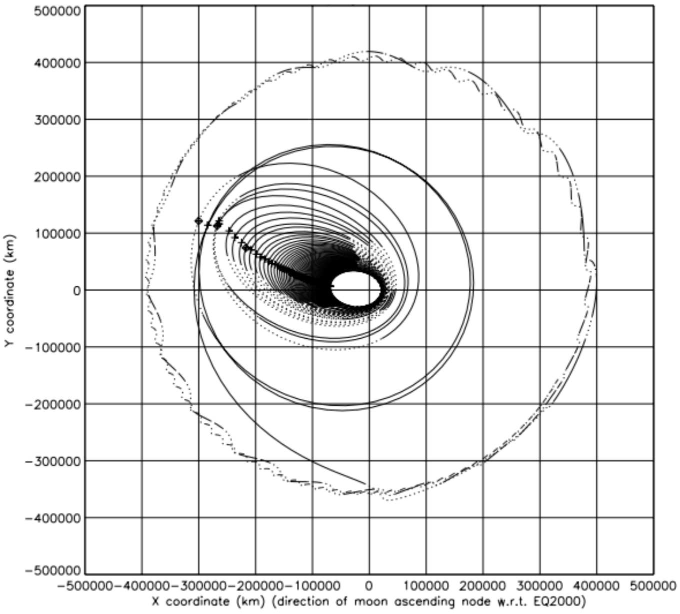

Figure 1.2: SMART-1 trajectory. The mission made use of low-thrust propulsion (spiralling phase) and ballistic capture. [4]

Other missions exploiting the ballistic capture phenomenon have been proposed. In this way, for the BepiColombo mission to Mercury, [5], solar electric propulsion can be used, avoiding once again the possibility of single point failures. For the Lunette mission to the Moon, the tranfer trajectory would have the benefit of avoiding eclipses during cruise: [6]. The use of low-energy transfers has been proposed for missions to the moons of Jupiter, to Mars and in the context of asteroid retrieval as well ([7], [8], [9]). Other possible applications can be found in small-satellite missions to the Moon, relying on low-thrust propulsion and/or solar sails, such as LunaH-Map and Lunar IceCube: [10].

1.1.2. FLOW-INFORMED STRATEGIES

Mission design is a trade-off between model accuracy and design feasibility. With the development of tools to tackle complex systems, their understanding is expanded and new solutions are revealed. In the Circular Restricted 3-Body Problem (CR3BP), for example, *invariant manifolds* follow from the analysis of the qualitative dynamics in the vicinity of unstable equilibrium points, as outlined for the first time in [11], and could not be found with a patched-conic view of the mission design process. Figure 1.3, showing the projection of such structures onto position space, is a result of more recent works (e.g. [12], [13]).

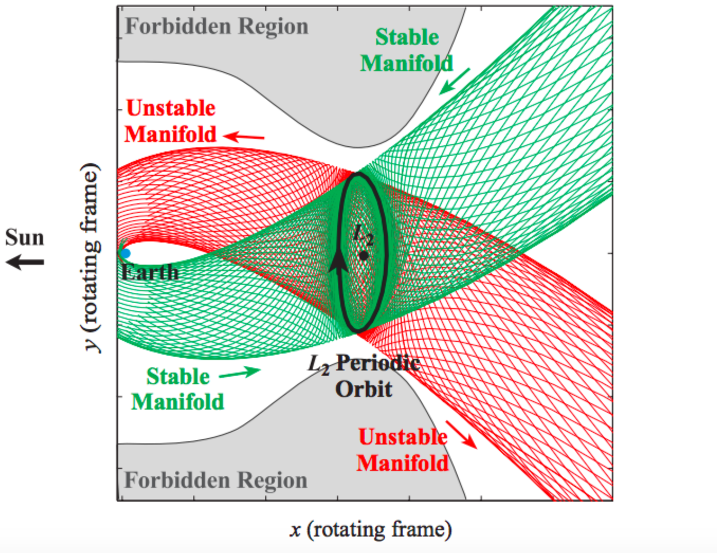

Figure 1.3: Projection of stable and unstable invariant manifolds onto position space. [12]

As a general consideration, the elimination of environmental features, triggering particular behaviours, limits available solutions.

In an analogous manner, *ballistic capture* trajectories make use of the chaotic nature and, in general, of the nuances of the dynamical system influencing the motion: [14]. In order to make their implementation feasible, the introduction of flow-informed strategies appears desirable. Developed in works focused on hyperbolic Lagrangian Coherent Structures (e.g. [15], [16]), this research project will focus on building from the Finite-Time Lyapunov Exponent (FTLE) and the Finite-Iteration Lyapunov Exponent (FILE) scalar fields: [17]. Such structures are an attempt to generalize the concept of invariant manifolds, separating regions of the phase space associated to qualitatively different behaviours.

1.2. MOTIVATIONS

Multiple reasons justify the use of Lagrangian Coherent Structures (LCS) in ballistic capture trajectory design, together with the development of related tools and heuristics. The application of analytical, differential instruments leads to high-accuracy results, as opposed to the ones coming from brute-force sampling techniques. Another important advantage, with respect to previous approaches, resides in a direct applicability in different phase spaces, justifying the increasing interest of their use for design and analysis in astrodynamics; the investigation of structures in specific spaces allows for a clearer understanding of the phenomenon and of its features; these can then be leveraged to construct low-energy trajectories. The potential reduction of computational cost can increase the applicability of the technique for the Guidance, Navigation and Control (GNC) system of autonomous missions. At the same time, the proposed flow-informed approach can be superimposed onto models of different fidelities, allowing to take into account n-body perturbations, Solar Radiation Pressure (SRP) and Non-Spherical Gravity (NSG), among others.

From a more abstract point of view, the *secondary theoretical comparison* between traditional methods related to the ballistic capture literature and the ones coming from the Lagrangian Coherent Structures field of research, makes it possible to contribute building an encompassing theory.

1.3. RESEARCH QUESTION

At the end of the *Literature Study* [18] conducted prior to this work, the following research question has been formulated:

Is it possible to characterize the ballistic capture mechanism, based on the initial osculating orbital parameters of the target-relative geometry, making use of the theory of Lagrangian Coherent Structures?

In the question formulation process, a number of secondary (sub-)questions have also been identified:

1. which variables define the phase space in which the features of the capture set are best described?
    (a) Which variables and methods allow for a fast computation of the capture set?
    (b) Which variables make visualization straightforward?
2. Can new mathematical tools, developed in the context of time-dependent dynamical systems, be used in the trajectory design process?
    (a) Can the use of stroboscopic maps help in the identification of features of the capture set?
    (b) Which Lagrangian method(s) is (are) best suited for Coherent Structures detection in Astrodynamics?

Question 2.a was triggered by [19] - Section 5.1 and [17] - Section 2; question 2.b by [20] and [21].

1.4. OBJECTIVE

Related to such questions, the objective of this work, expressed in high level terms, deals with further developing the theoretical underpinning of low-energy transfer orbits, by making use of Lagrangian Coherent Structures in non-periodic (and, more in general, time-dependent) dynamical systems in Astrodynamics. Following from the formulation of the main research question given above, it reads:

by looking at Lagrangian Coherent Structures in Astrodynamics time-dependent dynamical systems, the research objective is to further develop a theoretical framework in which the behaviour of ballistic capture orbits, as a function of the initial target-relative osculating orbital parameters of the spacecraft, can be explained.

Existing views on low-energy transfers in Astrodynamics (i.e. the Lagrangian Coherent Structures and the Ballistic Capture approaches) have been compared: because of the synthetic nature of this work, an important focus has been to look for contradictory and/or inconsistent aspects of the different approaches, when applied to specific problems.

1.5. STRUCTURE

- Chapter 2 will present the various reference frames used in the work, together with their relations; it will than outline the equations of motion of the dynamical systems of interest, with particular focus on perturbing forces, such as Non-Spherical Gravity (NSG) and Solar Radiation Pressure (SRP). The implementation of the variational equations, leading to the Cauchy–Green Strain Tensor, is also discussed here. The *GRATIS* toolbox will then be introduced, focusing on those features related to the theoretical content of the chapter; its main routines will finally be validated.
- Chapter 3 will focus on the ballistic capture phenomenon, giving definitions of objects of interest, such as the *Capture Set* and the *Weak Stability Boundary* (WSB), and presenting relevant results of previous works. The second part of the chapter will again focus on the numerical implementation and on the description of the main algorithms, used to compute such objects.
- Chapter 4 will describe various fields related to hyperbolic Lagrangian Coherent Structures[1]; from there, *Stroboscopic Strainlines*, the core idea of this work, will be presented and discussed. In conclusion, a flow-informed strategy, applicable to study the ballistic capture phenomenon, will be outlined.
- Chapter 5 will present the results, comparing traditional algorithms with the ones coming from the given flow-informed approach. This will be applied to different case studies, both forward and backward in time. The geometry of the resulting trajectories will be given and discussed.
  In conclusion, results associated to different 2D subsets of the phase space, will be given.
- Chapter 6 will summarise the conclusions of the work, underlining areas in which future developments appear desirable.
- Appendix A will present the SPICE system, used to retrieve the ephemerides and the features of different celestial bodies.

---

[1] Their definition is given in Section 4.5.

2

BACKGROUND

2.1. REFERENCE FRAMES

2.1.1. EARTH MEAN EQUATOR AND EQUINOX OF J2000

In order to introduce the first reference frame, it is necessary to define J2000: it is the epoch corresponding to $12:00$ at Greenwich, on January 1^{st}2000, Barycentric Dynamic Time (TDB).

As given in [22] and discussed in Appendix A, the ephemerides are defined in the *Earth Mean Equator and Equinox of J2000* (EME2000) reference frame. This is an Earth centered inertial reference frame, where, as given in [23], p. 245:

- the +x-axis (x_e) points at the mean equinox at J2000;
- the +z-axis (z_e) points at the celestial North Pole;
- the +y-axis (y_e) completes the right-handed reference frame.

In literature, sometimes, EME2000 is identified only by the direction of its axis, without specifying the location of the origin. It is therefore important to underline that, as stated in [24], the discrepancy between the International Celestial Reference Frame (ICRF) and the "Dynamical Mean Equator and Equinox of J2000" reference frame is negligible (when the latter is considered to be barycentric: [23], p.148)[1].

2.1.2. RADIAL-TANGENTIAL-NORMAL FRAME

In literature, the ballistic capture phenomenon has mainly been studied with respect to reference frames related to the orbit of the target body. In the Radial-Tangent-Normal frame at epoch t_0 (RTN@t_0, for brevity), centred at the target body:

- the z-axis (z_r) is perpendicular to the plane of the Sun orbit;
- the x-axis (x_r) is aligned with the Sun-planet line, pointing from the Sun to the planet;
- the y-axis (y_r) completes the dextral orthonormal triad.

As stated in [25], the transformation from RTN@t_0 to EME2000 (Figure 2.1) is given by the following:

$$\begin{pmatrix} x_e \\ y_e \\ z_e \end{pmatrix} = \begin{bmatrix} \sin\theta\sin\Omega\cos i - \cos\theta\cos\Omega & \sin\theta\cos\Omega + \cos\theta\sin\Omega\cos i & \sin\Omega\sin i \\ -\cos\theta\sin\Omega - \sin\theta\cos\Omega\cos i & \sin\theta\sin\Omega - \cos\theta\cos\Omega\cos i & -\cos\Omega\sin i \\ -\sin\theta\sin i & -\cos\theta\sin i & \cos i \end{bmatrix} \begin{pmatrix} x_r \\ y_r \\ z_r \end{pmatrix} \tag{2.1}$$

where i, Ω, ω and f are the inclination, the right ascension of the ascending node, the argument of periapsis and the true anomaly of the Sun in the EME2000 frame, respectively; $\theta = \omega + f$.

---

[1] For more details: https://naif.jpl.nasa.gov/pub/naif/toolkit_docs/Tutorials/pdf/individual_docs/17_frames_and_coordinate_systems.pdf (visited on 03-10-2019).

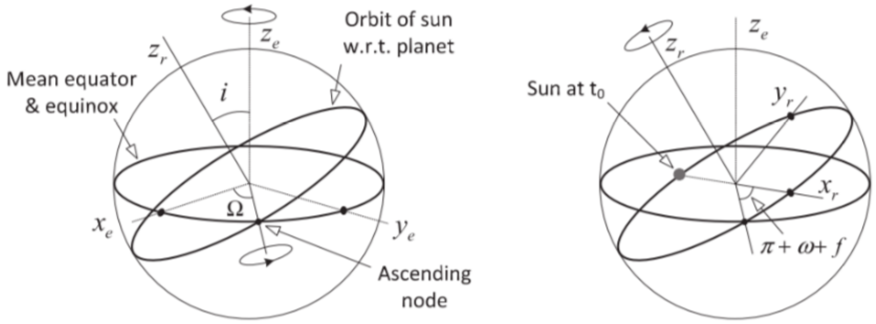

Figure 2.1: Geometry of EME2000 and RTN@t_0 frames. [25]

2.1.3. BODY MEAN EQUATOR FRAME

While the main results of this work are going to be presented in the Radial-Tangential-Normal Frame, the *Body Mean Equator Frame at Epoch* (BME@Epoch) frame is nevertheless introduced. This is because

- minor results, presented in Section 5.7, make use of this frame;
- the reference frame is an input of the simulator used for this work. The implementation of the proposed technique allows avoiding loss of generality, and future works may easily make use of this reference frame.

This frame is centred at the target body and (x_b, y_b, z_b) is defined such that:

- the z_b-axis is aligned with the target spin axis;
- the x_b-axis points to the ascending node of the target mean equator;
- the y_b-axis completes the dextral orthonormal triad.

The relation between EME2000 and BME@Epoch (Figure 2.2), as given in [22], reads as follows:

$$\begin{pmatrix} x_e \\ y_e \\ z_e \end{pmatrix} = \begin{bmatrix} -\sin\alpha & -\cos\alpha\sin\delta & \cos\alpha\cos\delta \\ \cos\alpha & -\sin\alpha\sin\delta & \sin\alpha\cos\delta \\ 0 & \cos\delta & \sin\delta \end{bmatrix} \begin{pmatrix} x_b \\ y_b \\ z_b \end{pmatrix} \tag{2.2}$$

where α and δ are the right ascension and declination, used to obtain the target spin axis direction.

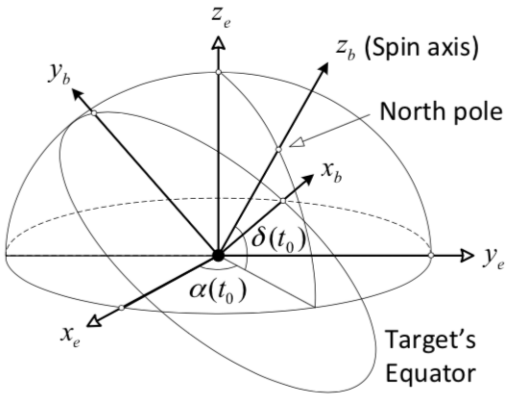

Figure 2.2: Geometry of EME2000 and BME@Epoch frames. [22]

2.2. EQUATIONS OF MOTION

As previously stated, the proposed flow-informed technique can be superimposed onto models of different fidelities: because of this, a restricted n-body problem, with the addition of Solar Radiation Pressure and Non-Spherical Gravity, will be used to formulate the equations of motion. This is, on the one hand, necessary, in order to take into account the fact that the ballistic capture phenomenon is chaotic in nature, and small perturbing forces may change the behaviour of an initial condition. On the other hand, simpler models (e.g. CR3BP) allow for for the use of more specific and more powerful tools, such as invariant manifolds.

Considering a system of n bodies, $n-1$ of which called primaries, it is interesting to study the motion of a particle of negligible mass w.r.t. them. From [22], the following differential equation can be used:

$$\ddot{\mathbf{r}} + \frac{\mu_t}{r^3}\mathbf{r} = -\sum_{i\in\mathbb{P}} \mu_i \left(\frac{\mathbf{r}_i}{r_i^3} + \frac{\mathbf{r}-\mathbf{r}_i}{||\mathbf{r}-\mathbf{r}_i||^3} \right) \tag{2.3}$$

where, as also shown in Figure 2.3:

- $\mathbf{r}$ identifies the position of the spacecraft with respect to the origin of the reference frame, in which the target body is located;
- r is the magnitude of the same vector;
- μ_t is the gravitational parameter of the target body and μ_i the one of body i;
- $\mathbf{r}_i$ is the position vector of body i and r_i is its magnitude;
- $\mathbb{P}$ is the set of $n-2$ perturbing bodies.

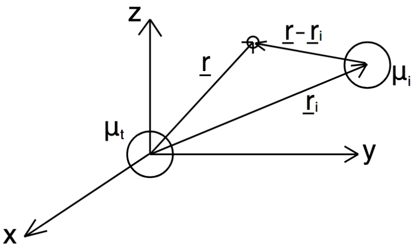

Figure 2.3: Geometry associated to the n-body problem.

In the context of this work, however, the following form, given in [25], underlines the hierarchy of influence of the bodies on the motion of the particle:

$$\ddot{\mathbf{r}} + \frac{\mu_t}{r^3}\mathbf{r} + \mu_s \left(\frac{\mathbf{r}_s}{r_s^3} + \frac{\mathbf{r}-\mathbf{r}_s}{||\mathbf{r}-\mathbf{r}_s||^3} \right) = -\sum_{i\in\mathbb{Q}} \mu_i \left(\frac{\mathbf{r}_i}{r_i^3} + \frac{\mathbf{r}-\mathbf{r}_i}{||\mathbf{r}-\mathbf{r}_i||^3} \right) \tag{2.4}$$

Here $\mathbb{Q}$ is the set of $n-3$ perturbing bodies, Sun excluded. From the same work, when Solar Radiation Pressure and the Non-Spherical Gravity of the target body are taken into account, the following differential equation governs the dynamics:

$$\ddot{\mathbf{r}} + \frac{\mu_t}{r^3}\mathbf{r} + \mu_s \left(\frac{\mathbf{r}_s}{r_s^3} + \frac{\mathbf{r}-\mathbf{r}_s}{||\mathbf{r}-\mathbf{r}_s||^3} \right) + Q_{f\to i}(t)\nabla U_{NSG} = \mathbf{f}_{SRP} - \sum_{i\in\mathbb{Q}} \mu_i \left(\frac{\mathbf{r}_i}{r_i^3} + \frac{\mathbf{r}-\mathbf{r}_i}{||\mathbf{r}-\mathbf{r}_i||^3} \right) \tag{2.5}$$

where U_{NSG} is an approximation of the potential function given in Section 2.2.2 and $Q_{f\to i}$ is a matrix, relating the planet-fixed reference frame (in which the function U_{NSG} is defined) and the (pseudo-)inertial reference frame, in which the equations of motion are written. More, about this, is given in Appendix A.

2.2.1. SOLAR RADIATION PRESSURE

In Equation (2.5), the effect of Solar Radiation Pressure (SRP) can be taken into account by virtue of ([23], p. 152):

$$\mathbf{f}_{SRP} = \frac{C_R L_S}{4\pi c} \frac{A}{m} \frac{\mathbf{r}-\mathbf{r}_s}{||\mathbf{r}-\mathbf{r}_s||^3} \tag{2.6}$$

where L_S is the luminosity of the Sun (W), c is the speed of light (m/s), C_r is the reflectivity of the spacecraft and A and m are its effective area (m^2) and mass (kg); $\mathbf{r}$ and $\mathbf{r}_s$ are the position vectors of the spacecraft and of the Sun, respectively. When A is assumed to be constant and independent of the orientation of the spacecraft (as it is the case in this work), the acceleration model is called *cannonball* Solar Radiation Pressure.

2.2.2. NON-SPHERICAL GRAVITY

As given in [23], p. 527, general potential theory shows that, assuming a static behaviour (therefore neglecting phenomena like ocean and pole tides), the gravitational potential of a given planet of arbitrary geometry and mass distribution, at a point outside the planet itself, is described by

$$U = -\frac{\mu}{r}\left[1 + \sum_{n=2}^{\infty}\sum_{m=0}^{n}\left(\frac{R}{r}\right)^n P_{n,m}(\sin\phi)\left(C_{n,m}\cos m\Lambda + S_{n,m}\sin m\Lambda\right)\right] \tag{2.7}$$

with

$$P_n(x) = \frac{1}{(-2)^n n!}\frac{\mathrm{d}^n}{\mathrm{d}x^n}(1-x^2)^n \tag{2.8}$$

$$P_{n,m}(x) = (1-x^2)^{m/2}\frac{\mathrm{d}^m P_n(x)}{\mathrm{d}x^m} \tag{2.9}$$

and where R is the reference radius, r the distance from the body center of mass and μ its standard gravitational parameter; ϕ is the geocentric latitude, Λ is the geographic longitude. These spherical coordinates are relative to a target-fixed reference frame, centred at its barycenter.
An alternative and more commonly used formulation of Equation (2.7) is given by

$$U = -\frac{\mu}{r}\left[1 - \sum_{n=2}^{\infty} J_n \left(\frac{R}{r}\right)^n P_n(\sin\phi) + \sum_{n=2}^{\infty}\sum_{m=1}^{n} J_{n,m}\left(\frac{R}{r}\right)^n P_{n,m}(\sin\phi)\cos m(\Lambda - \Lambda_{n,m})\right] \tag{2.10}$$

Equation (2.10) can hence be used to obtain the potential of the non-spherical components of the gravity field, used in (2.5), and given by:

$$U_{NSG} = U + \frac{\mu}{r} \tag{2.11}$$

For the specific case of Mars, numerical values associated to Equation (2.10) are given in Appendix A, Section A.1.1.

2.2.3. IMPLEMENTATION

In order to integrate the equations of motion and implement all the methodology outlined, making use of the SPICE ephemerides, the *GRAvity Tidal Slide* (*GRATIS*) toolbox has been used. Written in MATLAB and developed at PoliMi, its name comes from the fact that the toolbox's purpose is to make use of natural potential energy, analogous to the way in which submarines rely on tides to save fuel. GRATIS also means gratuitously, i.e., only making use of potential energy offered by the Solar system.

Numerical integration of the equations of motion is performed, making use of the *ode113* integrator: [26]. This function makes use of an Adams-Bashforth-Moulton variable step size integration routine. A Cowell propagator is used: the integrator propagates the Cartesian state of the spacecraft. These choices come from the analysis performed in [27] (Section 4.8), whose results will be used as a starting point for this work.

Another important feature of GRATIS is the implementation of dimensionless quantities. Physical quantities are normalized, making use of the following units:

- the unit of length DU is given by the mean radius of the central body. In the case of Mars, this is equal to 3396 km;
- the unit of time is given by

$$TU = \sqrt{\frac{DU^3}{\mu}}$$

  where μ is the gravitational parameter of the central body; in the case of Mars, this unit is approximately equal to 16 minutes.

The spacecraft has been modelled as a point mass with a mass-to-area ratio of 40 kg/m^2, and a reflectivity of 1.1.
While many regularization techniques have been introduced in [18], GRATIS makes use of both the positions and sizes of celestial bodies of interest (both planets and moons) to compute when a trajectory intersects them (more about this, in Section 3.3.1). The propagation is therefore stopped before any need to map the propagated state onto a singularity-free space.

LOSS OF SIGNIFICANCE

The formulation of the equations of motion has a direct impact on the efficiency of the numerical integration. In particular, considering the motion of a spacecraft in the vicinity of its target body, undergoing the gravitational attraction of other celestial objects, let's recall the last term of equation (2.3):

$$\frac{\mathbf{r}_i}{r_i^3} + \frac{\mathbf{r}-\mathbf{r}_i}{||\mathbf{r}-\mathbf{r}_i||^3}, \quad r \to 0 \tag{2.12}$$

Particularly when the spacecraft is located inside the Sphere of Influence (SOI) of the target body, the r-condition holds. The two terms can be re-written as:

$$\frac{\mathbf{p}}{p^3} - \frac{\mathbf{d}}{d^3} \tag{2.13}$$

where:

- $\mathbf{p} = \mathbf{r}_i$ is the position vector of body y;
- $\mathbf{d} = \mathbf{r}_i - \mathbf{r}$ is the position vector of body i, relative to the spacecraft (Figure 2.3).

Since, studying ballistic capture, the spacecraft is often located in the vicinity of the target body, the terms $\mathbf{p}/p^3$ and $\mathbf{d}/d^3$ are nearly equal: storing their difference in a computer would lead to a large rounding error, because of the limited number of significant digits available for its representation.
In order to avoid such *loss of significance*, following [28] (Section 8.4), Equation (2.13) can be replaced by:

$$\frac{1}{d^3}\left(\mathbf{r}+f(q)\mathbf{p}\right) \tag{2.14}$$

with

$$f(q) = q\frac{3+3q+q^2}{1+(1+q)^{3/2}}$$

$$q = \frac{\mathbf{r}\cdot(\mathbf{r}-2\mathbf{p})}{\mathbf{p}\cdot\mathbf{p}}$$

Loss of significance can therefore be avoided, at the expense of the simulator computational complexity.

ROTO-PULSATING REFERENCE FRAME

In order to be able to switch from a low-fidelity model to an n-body problem model, the latter can be written as a perturbed CR3BP in a non-uniformly rotating, pulsating reference frame (RPRnBP - [29]); the geometry of the problem is given in Figure 2.4.

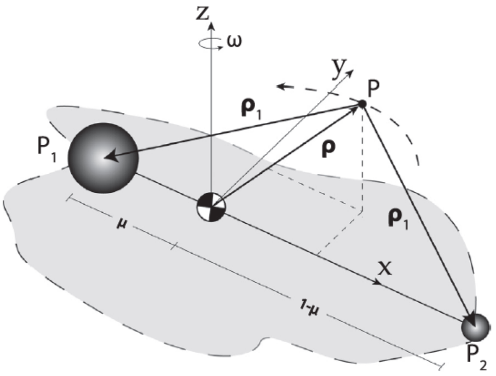

Figure 2.4: Roto-pulsating reference frame. [29]

The position of the spacecraft in the inertial reference frame, $\mathbf{r}$(t), can be related to the one in the new reference frame, $\boldsymbol{\rho}$(t), by means of:

$$\mathbf{r}(t) = \mathbf{b}(t) + k(t)\mathcal{C}(t)\boldsymbol{\rho}(\tau) \tag{2.15}$$

where

$$\mathbf{b}(t) = \frac{m_1\mathbf{r}_1(t)+m_2\mathbf{r}_2(t)}{m_1+m_2}, \qquad k(t) = ||\mathbf{r}_2(t)-\mathbf{r}_1(t)||$$

$$\mathcal{C} = [\mathbf{e}_1(t), \mathbf{e}_2(t), \mathbf{e}_3(t)], \qquad \mathbf{e}_1 = \frac{\mathbf{r}_2(t)-\mathbf{r}_1(t)}{k(t)}$$

$$\mathbf{e}_3(t) = \frac{(\mathbf{v}_2(t)-\mathbf{v}_1(t))\times(\mathbf{r}_2(t)-\mathbf{r}_1(t))}{||(\mathbf{v}_2(t)-\mathbf{v}_1(t))\times(\mathbf{r}_2(t)-\mathbf{r}_1(t))||}$$

$$\mathbf{e}_2(t) = \mathbf{e}_3(t)\times\mathbf{e}_1(t), \qquad \tau = \sqrt{\frac{G(m_1+m_2)}{\overline{a}^3}}(t-t_0)$$

In the relation between t and τ, $\overline{a}$ is the mean distance of the two primaries over a long time span. By means of such transformation, it is possible to compare the results of the full ephemeris model with the ones related to a simplified dynamical model, understanding the effect of the refinement step on the results. A number of results, given in Section 5.6, are going to make use of this reference frame.

2.3. VARIATIONAL EQUATIONS

Independently of the terms considered in Section 2.2, once the reference frame is given, the motion of the massless body can be described by:

$$\begin{cases} \dot{\mathbf{x}}(t) & = & \mathbf{f}(\mathbf{x}(t), t) \\ \mathbf{x}(t_0) & = & \mathbf{x}_0 \end{cases} \tag{2.16}$$

with $\mathbf{x}(t) \in \Omega \subseteq \mathbb{R}^6$. As usual, the first order differential equation (the *velocity map*) can be obtained at the expenses of doubling the number of independent variables of the system[2]. Because of the nature of the (perturbed) n-body problem presented above, there is a direct dependence with respect to time in the velocity: the system is non-autonomous.
The integration of this set of equations allows to compute the *flow map* of the system,

$$\begin{aligned} \phi_{t_0}^{t} &: \Omega \to \Omega \\ &\mathbf{x}_0 \mapsto \phi_{t_0}^{t}(\mathbf{x}_0) = \mathbf{x}(t; t_0, \mathbf{x}_0) \end{aligned}$$

giving its state at time t for each initial state $\mathbf{x}_0$ and initial time t_0.
Moreover, once the *State transition Matrix* (STM)

$$\Phi := \Phi(t; t_0, \mathbf{x}_0) = D_{\mathbf{x}_0}\phi_{t_0}^{t}(\mathbf{x}_0) = D_{\mathbf{x}_0}\mathbf{x}(t; t_0, \mathbf{x}_0) \tag{2.17}$$

is defined, it can be propagated by means of

$$\begin{cases} \dot{\Phi} & = & D_{\mathbf{x}}\mathbf{f}(\mathbf{x}, t)\Phi & = & \mathbf{A}(\mathbf{x}, t)\Phi \\ \Phi(t_0; t_0, \mathbf{x}_0) & = & \mathbf{I}_n \end{cases} \tag{2.18}$$

where $\mathbf{A}$ is the Jacobian of the velocity field and $\mathbf{I}_n$ is the identity matrix of size n. The derivation is given, among others, in [31]. The joint system, characterized by $n^2 + n$ independent variables, defines the *Variational equations*, allowing to propagate the State Transition Matrix of the dynamical system.

2.3.1. CAUCHY-GREEN STRAIN TENSOR

The Finite-time Cauchy-Green (CG) Strain Tensor can now be introduced:

$$\Delta(T, \mathbf{x}_0, t_0) := \Phi^T(t_0 + T; \mathbf{x}_0, t_0) \cdot \Phi(t_0 + T; \mathbf{x}_0, t_0) \tag{2.19}$$

It allows to quantify the relative stretching of nearby trajectories for a given time interval.
The CG tensor Δ, symmetric and positive definite, is therefore characterized by n real positive eigenvalues; it relates the final state offset, with respect to the initial one, by means of the following Taylor expansion:

$$||\delta\mathbf{x}(t_0 + T)||^2 \approx ||\Phi(\mathbf{t_0} + \mathbf{T}; \mathbf{x_0}, \mathbf{t_0}) \cdot \delta\mathbf{x}_0||^2 = \delta\mathbf{x}_0^T \cdot \Phi(\mathbf{t_0} + \mathbf{T}; \mathbf{x_0}, \mathbf{t_0})^T \cdot \Phi(\mathbf{t_0} + \mathbf{T}; \mathbf{x_0}, \mathbf{t_0}) \cdot \delta\mathbf{x}_0 = \delta\mathbf{x}_0^T \cdot \Delta(T, \mathbf{x}_0, t_0) \cdot \delta\mathbf{x}_0$$

Extensive use of this object will be made in Chapter 4; in particular, its eigendecomposition is a powerful tool to enable the study of the underlying dynamics. The result of the process, allowing to obtain the eigenvalues $0 \leq \lambda_1 \leq \cdots \leq \lambda_n$ and the associated eigenvectors, ξ_i, is shown in Figure 2.5.

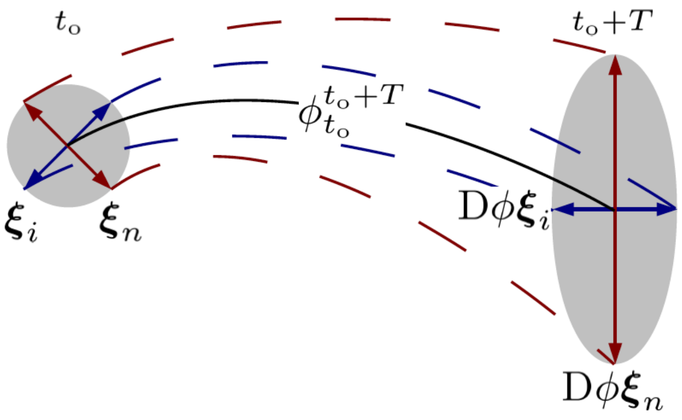

Figure 2.5: Stretching Associated with Eigenvectors of the Cauchy-Green Tensor. [19]

2.3.2. IMPLEMENTATION

While the computation of the State Transition Matrix, and hence of the Cauchy-Green Strain Tensor, has been implemented by means of integrating the variational equations given above, it is worth mentioning alternative approaches, proposed in [19].

---

[2] See [30] for Ordinary Differential Equations (ODE).

- Finite differencing allows to estimate the STM, by propagating initial state vectors separated by small perturbations. The State Transition Matrix could be computed (e.g. 2D problem) using

$$\Phi(t;t_0,\mathbf{x}_0)=\begin{bmatrix} \dfrac{x_{i+1,j}(t)-x_{i-1,j}(t)}{x_{i+1,j}(t_0)-x_{i-1,j}(t_0)} & \dfrac{x_{i,j+1}(t)-x_{i,j-1}(t)}{y_{i,j+1}(t_0)-y_{i,j-1}(t_0)} \\ \dfrac{y_{i+1,j}(t)-y_{i-1,j}(t)}{x_{i+1,j}(t_0)-x_{i-1,j}(t_0)} & \dfrac{y_{i,j+1}(t)-y_{i,j-1}(t)}{y_{i,j+1}(t_0)-y_{i,j-1}(t_0)} \end{bmatrix} \tag{2.20}$$

  with (i,j) representing the initial perturbation in (x,y). While this is an efficient technique to estimate the State Transition Matrix, it leads to less accurate results, compared to the Variational Equations integration. Nevertheless, finite differencing has been used in this work, in order to compute the Jacobian of the velocity field $\mathbf{A}$ given in Equation (2.18).

- Making use of an auxiliary grid (as the one given in [16]) allows to increase the accuracy of the computation, by bracketing each of the primary grid points.

2.4. Validation

In the validation of the various routines implemented in GRATIS, the TU Delft Astrodynamics Toolbox (TUDAT) has been used as a reference; with this, it has been possible to propagate the state of the spacecraft and, propagating the variational equations, obtain the State Transition Matrix of the problem, for a given initial state/epoch.

The simulation has been initialized at '08 MAY 2015 12:36:08.640 (UTC)', corresponding to 4.84360635825×10^8 seconds after $J2000$; the final time is given by $t_f=5.23686894807\times10^8$ s, and it corresponds to the epoch at which the spacecraft completes one revolution around its central body, Mars.

Other bodies are included in the simulation, in order to validate the correct implementation of SPICE: together with Mars, also the Sun, the Earth, Jupiter and Saturn (and, therefore, their ephemerides) are considered.

The spacecraft is assumed to be characterized by:

- Mass: 400 kg;
- Surface: 10 m^2;
- C_R: 1.1;

Together with the central gravity introduced by the mentioned bodies, the motion of the spacecraft is influenced also by (cannonball) solar radiation pressure and by the non-spherical components of Mars' gravity field, up to degree and order 10.

The initial state of the spacecraft is implicitly given by its Kepler elements, expressed with respect to a Mean Earth Equatorial frame (at J2000), centred at Mars:

$$a=1.37753631448\times10^9\ m,\qquad e=0.99$$

$$i=\omega=\Omega=f=0.0\ rad \tag{2.21}$$

where a and e are the semi-major axis and eccentricity of the orbit, respectively.

This initial condition is in the Weak Stability Boundary[3] of the problem, where third-body perturbations are known to play an important role in the dynamics of the spacecraft.

The equations have been propagated using a Cowell propagator and an Adams-Bashforth-Moulton variable step size integrator, with a minimum step-size of *machine epsilon*[4] and a maximum step-size of *positive infinity*[5]; relative and absolute tolerances have been set to 10^{-10}. The same integration settings have been used to propagate the variational equations of the system.

Figure 2.6 and 2.7 present the results of both propagations, looking at the position and velocity of the spacecraft, respectively, during approximately 19 months. The final state of the GRATIS propagation is given by

$$\mathbf{x}=10^9\times\begin{pmatrix} 1.094339216379882 \\ 0.000000000000940 \\ -0.114790390419061 \\ 0.000000200931406 \\ 0.000000131982575 \\ 0.000000044718382 \end{pmatrix} \tag{2.22}$$

where the units are meters and meters per second. The final state (same units) of the TUDAT propagation is given by

---

[3] Chapter 3 will define this object, together with presenting an algorithm to compute it accurately.

[4] Machine epsilon is the difference between 1.0 and the next value representable by the floating-point (in this case type *double*).

[5] The positive infinity is the value with all bits of the exponent set and all bits of the fraction cleared.

$$\mathbf{x} = 10^9 \times \begin{pmatrix} 1.094584254790360 \\ 0.000796871130608 \\ -0.114435163769937 \\ 0.000000200749525 \\ 0.000000132084634 \\ 0.000000044784178 \end{pmatrix} \tag{2.23}$$

Leading to the following position and velocity offsets:

$$||\Delta\mathbf{r}|| = 9.0622 \times 10^5 \quad m$$

$$||\Delta\mathbf{v}|| = 0.2187 \quad m/s$$

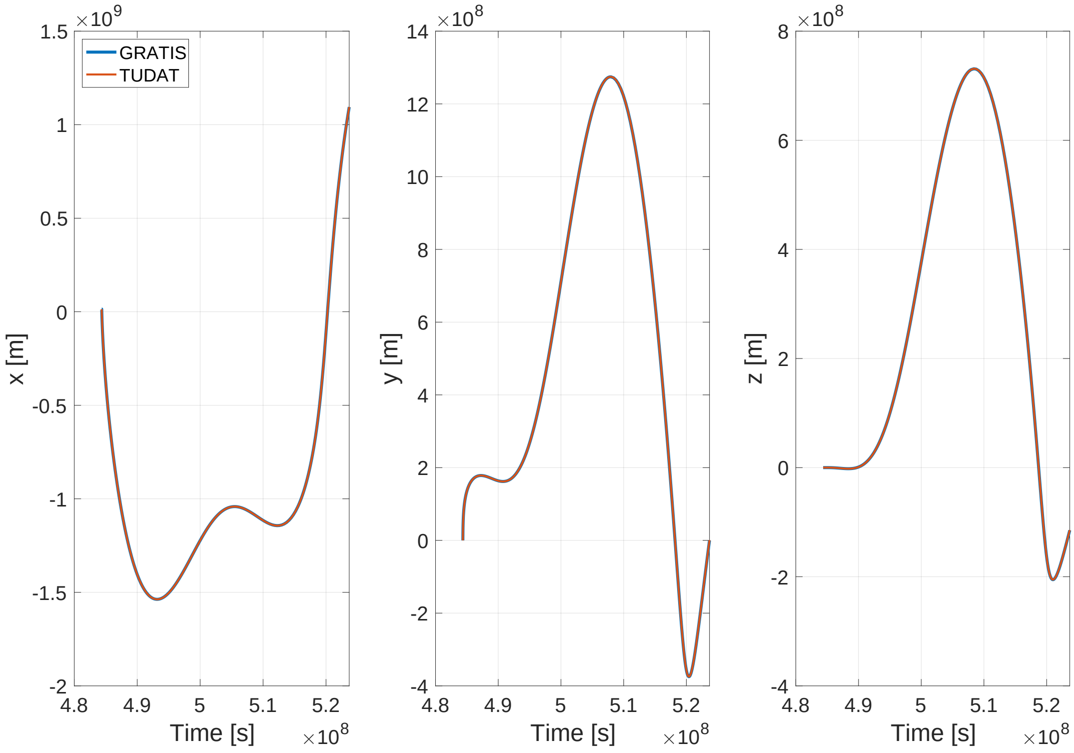

Figure 2.6: GRATIS-TUDAT Position verification

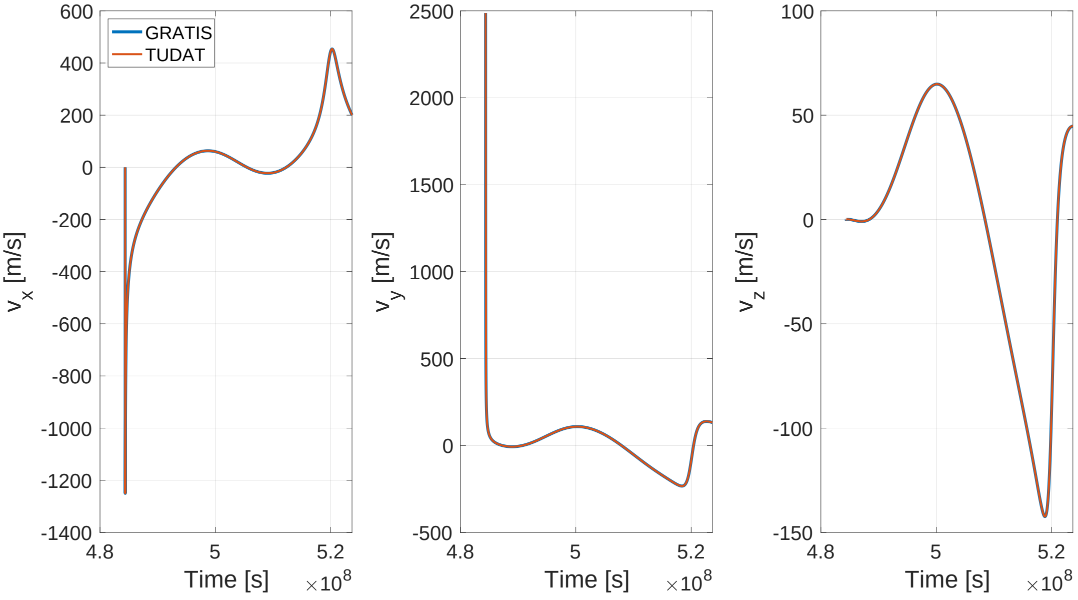

Figure 2.7: GRATIS-TUDAT Velocity verification

Figure 2.8 represents the GRATIS propagation of the State Transition Matrix, while Figure 2.9 the one obtained with TUDAT:

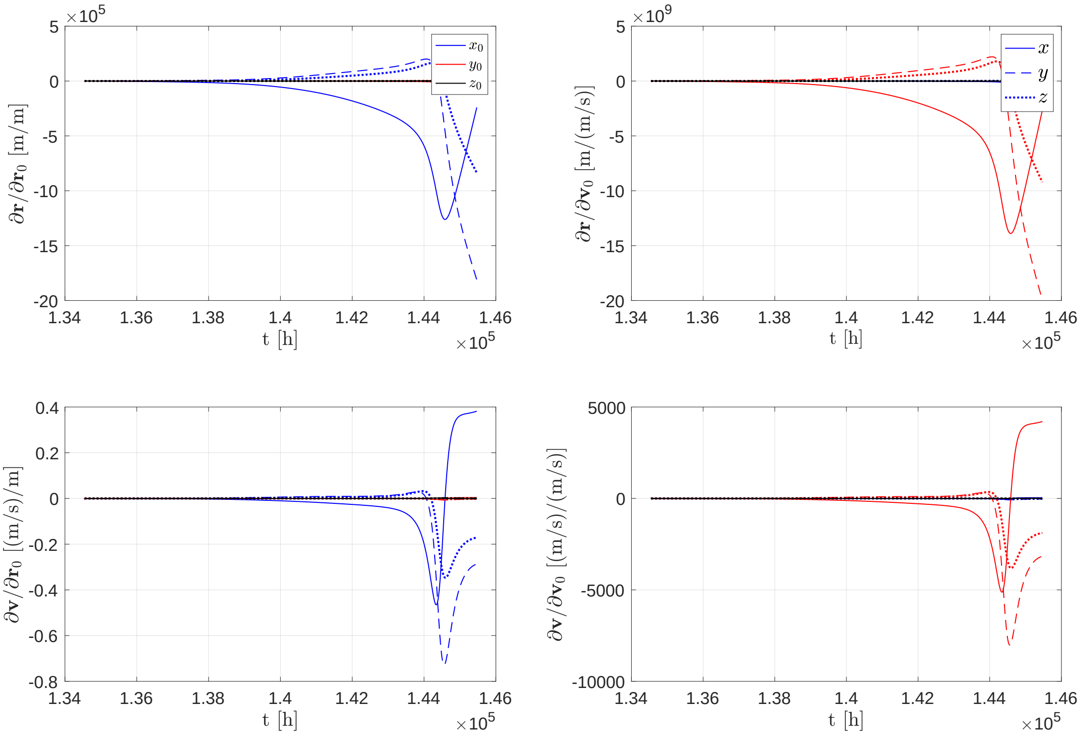

Figure 2.8: GRATIS State Transition Matrix propagation

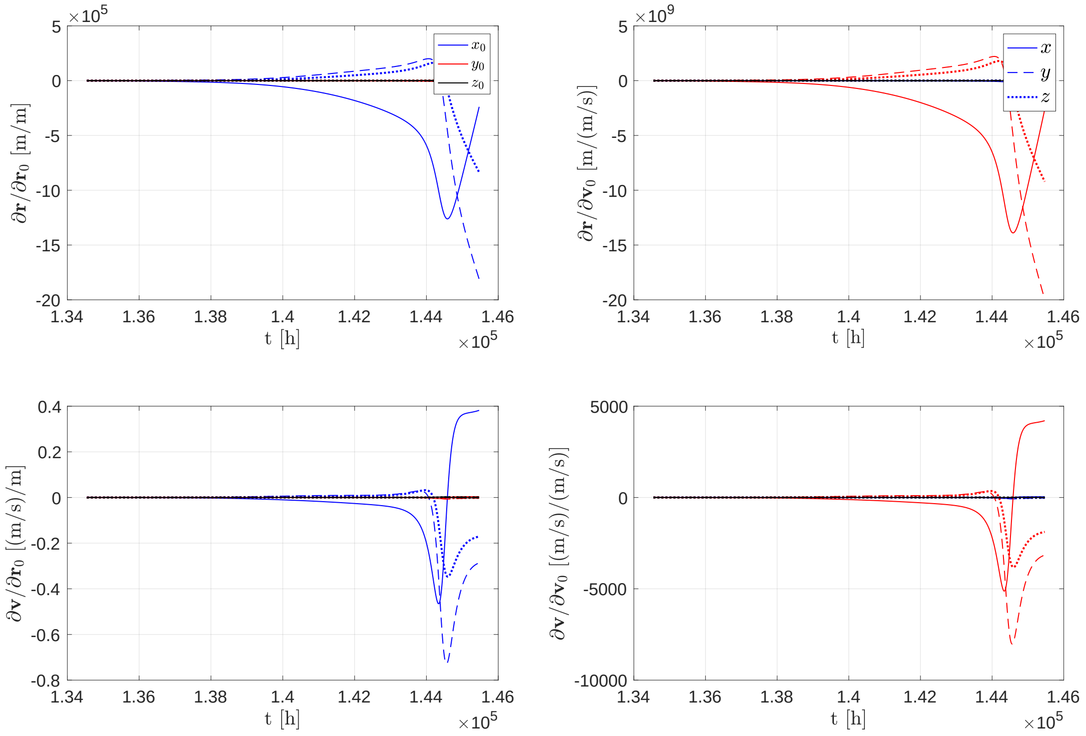

Figure 2.9: TUDAT State Transition Matrix propagation

The values associated to the final epoch of the propagations are given by:

$$10^{-7} \times \Phi_T =$$

$$= \begin{bmatrix} -0.023874355942 & -0.000212656418 & 0.000091293292 & -2.365332506253 & -262.983692323880 & -0.038614800048 \\ -0.181154966786 & -0.001767440578 & 0.000779600869 & -19.643441629881 & -1995.363165428160 & -0.346397908475 \\ -0.083636818291 & -0.000824513982 & 0.000345355469 & -9.162896434402 & -921.229930603506 & -0.158034356618 \\ 0.000000038181 & 0.000000000369 & -0.000000000161 & 0.000004096363 & 0.000420558619 & 0.000000071259 \\ -0.000000028656 & -0.000000000283 & 0.000000000125 & -0.000003145076 & -0.000315636210 & -0.000000055712 \\ -0.000000017109 & -0.000000000169 & 0.000000000071 & -0.000001882088 & -0.000188445639 & -0.000000033054 \end{bmatrix}$$

$$10^{-7} \times \Phi_G =$$

$$= \begin{bmatrix} -0.024011594350 & -0.000213986636 & 0.000091876199 & -2.380117508339 & -264.495336581092 & -0.038872952120 \\ -0.181094384438 & -0.001766863755 & 0.000779349446 & -19.637030175254 & -1994.695855677720 & -0.346290091969 \\ -0.083595664423 & -0.000824117517 & 0.000345191466 & -9.158489967907 & -920.776624795710 & -0.157957959607 \\ 0.000000038170 & 0.000000000368 & -0.000000000161 & 0.000004095160 & 0.000420437566 & 0.000000071238 \\ -0.000000028673 & -0.000000000283 & 0.000000000125 & -0.000003146894 & -0.000315819095 & -0.000000055745 \\ -0.000000017116 & -0.000000000169 & 0.000000000071 & -0.000001882883 & -0.000188524799 & -0.000000033067 \end{bmatrix}$$

where the units are the ones given in the associated Figures above. While TUDAT is more efficient in performing the propagation, GRATIS contains a number of subroutines that make it a preferable toolbox, in the context of this thesis work.

3

BALLISTIC CAPTURE

3.1. INTRODUCTION

It is important to start by defining *what* ballistic capture is: it is a phenomenon by means of which the spacecraft approaches a target celestial body and starts revolving around it only by means of gravitational interactions with two or more celestial bodies [32]. Because the process is reversible (i.e., the spacecraft can also escape from the target gravity field) other forces, such as thrust or interaction with the target atmosphere, need to take place in order to make the capture permanent.

An alternative definition is given in [3]: "ballistic capture by a planet occurs when an object enters, under natural dynamics, within the sphere of influence of that planet and makes at least one complete revolution around it". While this definition may be preferable, because it allows to take into account non-spherical gravity and solar radiation pressure, as it is done in this work, the Sphere Of Influence (SOI) constraint has been relaxed in more recent works.

The study of the phenomenon allows to use low-energy transfers to reach a celestial body, eliminating the need for an injection manoeuvre, and, therefore, the possibility of single-point failures.

3.2. STABLE SET & WEAK STABILITY BOUNDARY

3.2.1. ALGORITHMIC DEFINITION

Considering, in the context of a perturbed n-body problem, the motion of the particle P_3 with respect to the target body P_2, its relative Kepler energy H_2 can be introduced:

$$H_2 = \frac{1}{2}v_2^2 - \frac{\mu}{r_2} \tag{3.1}$$

from this it is easy to understand why at least one perturbing body is necessary, in order for capture to be possible: the relative energy of the spacecraft has to go from positive to negative. In studying ballistic capture, the initial condition of the motion is such that P_3 starts at the periapsis of an osculating ellipse[1] (Figure 3.1), therefore

$$r_2 = a(1-e), \quad v_2 = \sqrt{\frac{\mu(1+e)}{r_2}} \tag{3.2}$$

---

[1] Because of this, the nomenclature *(peri)apse map* can be introduced. [10]

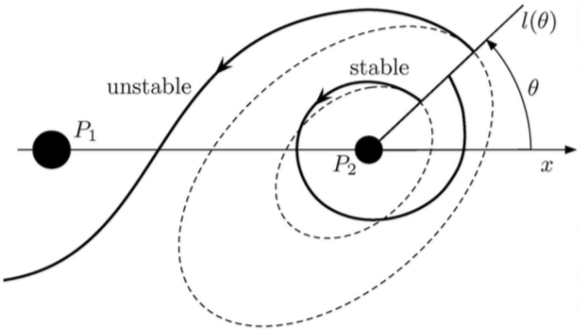

Figure 3.1: Geometry of 1-stable and unstable trajectories relative to P_2. [2]

Recalling the idea of Poincaré section (presented in Section 4.3), the initial position is on a radial segment emanating from P_2 and forming an angle θ with the P_1P_2 line: the search space is sampled, together with changing the value of θ in $[0,2\pi]$, also considering different initial distances from the target and different values of the eccentricity. In [2], for example, the grid is given by

$$r = \{0, 2\cdot 10^{-3}, \dots, 1.5\}, \quad \theta = \{0, 2\pi/1000, \dots, 2\pi\}, \quad e = \{0, 0.05, \dots, 0.95\} \tag{3.3}$$

The resulting orbit is considered to be stable if P_3 makes a complete turn around P_2 maintaining a negative Kepler energy after a revolution and without revolving around P_1. From the analysis of the orbits associated to each $l(\theta)$, the set of stable points, countable union of open intervals, can be introduced:

$$\mathcal{W}(\theta, e) = \bigcup_{k\geq 1} (r^*_{2k-1}, r^*_{2k})$$

In this definition, the various r^* are endpoints of stable intervals. As anticipated, varying θ in $[0,2\pi]$ allows to introduce the following set:

$$\mathcal{W}(e) = \bigcup_{\theta\in[0,2\pi)} \mathcal{W}(\theta, e)$$

Finally, considering all the eccentricities associated to a negative energy (i.e., $e \in [0,1)$), the *Stable Set* can be introduced:

$$\mathcal{W} = \bigcup_{e\in[0,1)} \mathcal{W}(e) \tag{3.4}$$

From $\mathcal{W}$, the *Weak Stability Boundary* (WSB) $\partial\mathcal{W}$ can be defined. It is the locus of points $r^*(\theta, e)$, for each radial line $l(\theta)$, in which a change of stability in the associated trajectory occurs:

$$\partial\mathcal{W} = \{r^*(\theta, e) | \theta \in [0,2\pi], e \in [0,1]\} \tag{3.5}$$

Roughly speaking, the Weak Stability Boundary identifies the separatrix between those points in the phase space (defining the state of the spacecraft) leading to capture orbits and those leading to different behaviours, such as escape orbits. For illustration purposes, fixing the eccentricity leads to the introduction of a particular subset of the WSB:

$$\partial\mathcal{W}(e) = \{r^*(\theta, e) | \theta \in [0,2\pi]\}. \tag{3.6}$$

Dealing with its computation, [2] introduced a bisection method, in order to identify the exact location of the boundary condition. The same has been done in this work: such method will be introduced in Section 3.5.

It is finally worth mentioning that relatively old works, like [32] and [33], presented an analytical definition/approximation of the Stable Set and of the Weak Stability Boundary. Such elegant formulation has been abandoned in later works. The too much conservative nature of this definition and its relations with the algorithmic one are deeply investigated in [34]. In fact, since only inside the target Sphere of Influence a two-body analysis is meaningful, the use of Kepler energy as a reliable quantifier should be restricted to such region. It is because of such considerations that only the algorithmic definition has been presented here.

3.2.2. GENERALIZED STABLE SET AND WSB

The idea of considering more intersections with l, in order to study the different stable sets, was first outlined in [35]. In this way, for a given n, a generalized Stable Set $\mathcal{W}_n$ can be introduced (Figure 3.2): it contains the initial conditions for which the orbit makes n stable revolutions around the target. Recalling the definition of stability given above, the n

revolutions are stable if the point mass returns at $l(\theta)$ with negative Kepler energy with respect to P_2 and without making a complete turn around P_1.

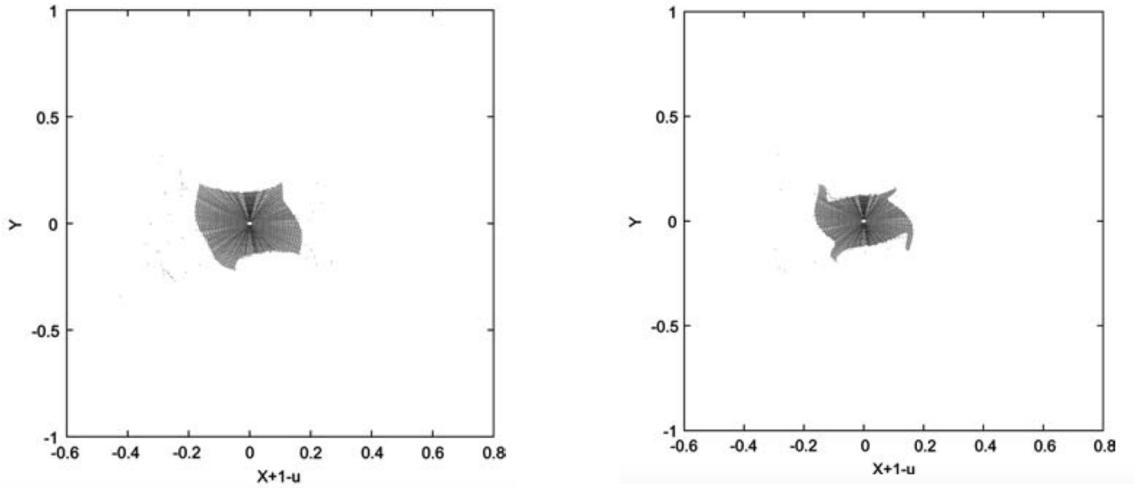

Figure 3.2: Comparison between $\partial\mathcal{W}_3$ and $\partial\mathcal{W}_6$ in the CR3BP, for $\mu = 0.0121506683$, for an initial circular osculating orbit. [35]

The work [2] further develops the idea considering the openness of the Stable Sets. This generalized Stable Set is defined by the same relations given above: only the meaning of stability is different. From $\mathcal{W}$, the Generalized Weak Stability Boundary $\partial\mathcal{W}$ can again be defined as the locus of points $r^*(\theta, e)$, endpoints of an n-stable interval $\left(r^*_{2k-1}, r^*_{2k}\right)$.

3.3. 3D MODEL

While, in the 2D case, the introduction of a radial half-line is enough, in order to study the stability of the particle, the 3D case requires the introduction of an half-plane. This is the case because, according to the stability criterion previously defined, the motion would, otherwise, always be classified as unstable [33].

The work [36], generalizing the considerations in [33], presented an algorithmic definition of the WSB, in the context of the Elliptic Restricted 3-Body Problem (ER3BP). In both these references, however, the half-plane is defined in a rotating reference frame, being related to models naturally described in it.

In [22], the intersection plane, fixed in the inertial reference frame, is defined by the initial position and angular momentum (see Figure 3.3): it is given by all the $\mathbf{r} = (x, y, z)$, such that

$$\mathbf{r} \cdot (\mathbf{h}_0 \times \mathbf{r}_0) = 0 \tag{3.7}$$

A complete revolution is performed at time t_1 if the particle lies on the intersection plane:

$$\mathbf{r}^{(k)}(t_1) \cdot (\mathbf{h}_0 \times \mathbf{r}_0) = 0 \tag{3.8}$$

In particular, it has to lie on the semi-plane of interest:

$$\mathbf{r}^{(k)}(t_1) \cdot \mathbf{r}_0 > 0 \tag{3.9}$$

Finally, the intersection has to be associated to complete revolutions:

$$(\mathbf{v}^{(k)}(t_1) \cdot \mathbf{v}_0)(\mathbf{v}^{(k-1)} \cdot \mathbf{v}_0) > 0 \tag{3.10}$$

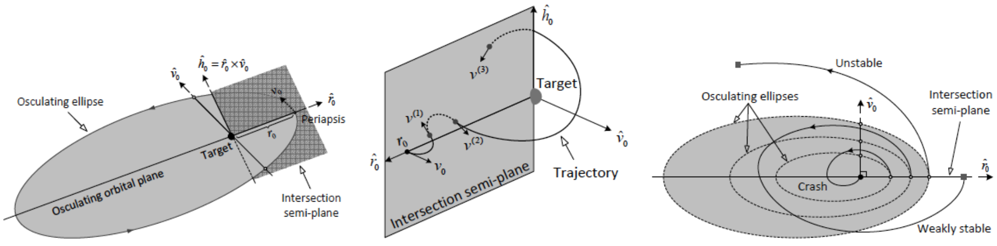

(a) Intersection plane (b) Multiple intersections (c) Orbit categories

Figure 3.3: Definition of Spatial Stability. [22]

Escape is identified by the time t_e in which the Kepler energy H_t becomes positive and, at the same time, the particle is located outside the target Sphere of Influence:

$$H_t(t_e) = \frac{v^2}{2} - \frac{1}{r} > 0 \tag{3.11}$$

$$r(t_e) > R_s \tag{3.12}$$

As previously mentioned, considering only the first of these conditions leads to a non-conservative classification.

3.3.1. ORBIT CLASSIFICATION & RANKING

The set of initial conditions can be divided into four subsets, so that all its elements belong to one and only one of the subsets.

- The n-Weakly Stable Set $\mathcal{W}_n$ contains the elements associated to the orbits performing n complete revolutions around the planet (Figure 3.4).

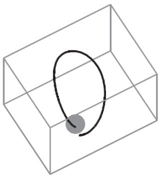

Figure 3.4: Weakly Stable Sample Orbit. [22]

- The n-Unstable Set $\mathcal{X}_n$ contains the elements associated to the orbits that, after $n-1$ complete revolutions, escape the planet (Figure 3.5).

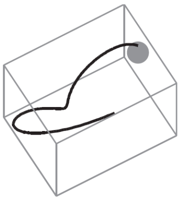

Figure 3.5: Unstable Sample Orbit. [22]

- The n-Crash Set $\mathcal{K}_n$ contains the elements associated to the orbits that, after $n-1$ complete revolutions, impact the planet (Figure 3.6).

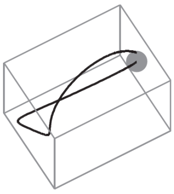

Figure 3.6: Crash Sample Orbit. [22]

- The n-Acrobatic Set $\mathcal{D}_n$ contains the elements associated to the orbits that, after $n-1$ complete revolutions, satisfy none of the above conditions within a given time span (Figure 3.7).

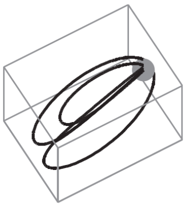

Figure 3.7: Acrobatic Sample Orbit. [22]

This Orbit Classification has been slightly modified from the one given in [25], underlining the generalization by [35]. Also, *backward* stability (and all other behaviours) can be defined, categorizing the orbits integrated backward in time ([37], [38]).
From these definitions, the *Capture Set* can be introduced:

$$\mathcal{C}_{-1}^{n} := \mathcal{X}_{-1} \cap \mathcal{W}_n \tag{3.13}$$

The set $\mathcal{C}_{-1}^{n}$ contains all the conditions associated to orbits that, after being captured by the target body, perform n revolutions around it.

3.3.2. STABILITY INDEX & CAPTURE RATIO

There has always been the need to somehow filter the obtained capture orbits and look for the *ideal* one; while [37] introduced two filters, [22] introduced the Stability Index. It is given by

$$\mathcal{S} = \frac{t_n - t_0}{n} \tag{3.14}$$

with t_n the time at which the n^{th} revolution is completed. Physically, such index represents the mean period of the captured orbit.
In the context of this work, a *normalized* Stability Index has been introduced; this is simply given by:

$$\overline{\mathcal{S}} = \frac{\mathcal{S}}{\mathcal{S}_k} \tag{3.15}$$

where $\mathcal{S}_k$ is the stability index of to the Keplerian elliptic orbit (i.e., its period) associated to the same initial state. It is given by:

$$\mathcal{S}_k = 2\pi \left[\frac{r_0}{1-e_0} \right]^{3/2}$$

Without the proposed normalization, high values of the Stability Index $\mathcal{S}$ would identify not only irregular orbits, but also the regular ones associated to high values of r_0; this can also be inferred from Figure 3.8. The use of $\overline{\mathcal{S}}$, for the categorization of a set of orbits, allows to identify the most regular one, irrespective of its size.

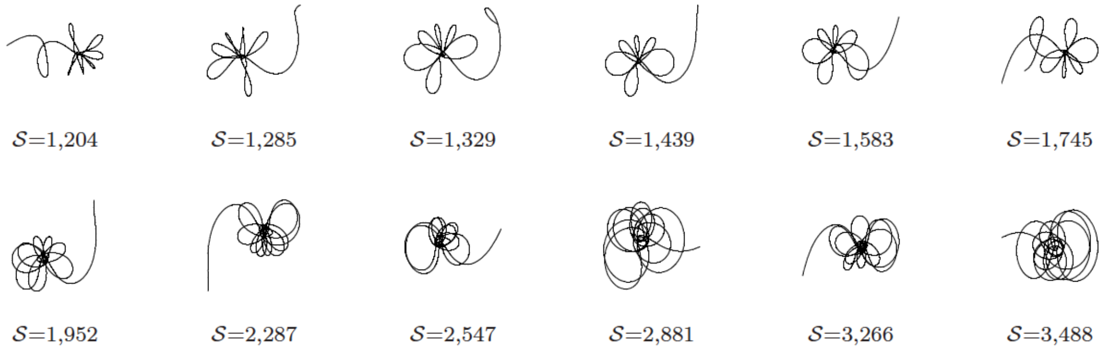

$\mathcal{S}$=1,204 $\mathcal{S}$=1,285 $\mathcal{S}$=1,329 $\mathcal{S}$=1,439 $\mathcal{S}$=1,583 $\mathcal{S}$=1,745

$\mathcal{S}$=1,952 $\mathcal{S}$=2,287 $\mathcal{S}$=2,547 $\mathcal{S}$=2,881 $\mathcal{S}$=3,266 $\mathcal{S}$=3,488

Figure 3.8: Ballistic capture orbits and their stability index. [22]

Finally, the Capture Ratio, introduced in [25], measuring the occurrence of capture orbits, is given by

$$\mathcal{R}_C = \frac{N_{\mathcal{C}^n_{-1}}}{N_{r_0} \times N_{\omega_0}} \tag{3.16}$$

where $N_{\mathcal{C}^n_{-1}}$ is the number of elements in $\mathcal{C}^n_{-1}$ and the denominator is equal to the number of investigated initial conditions.

3.4. FEATURES IN A 3D, N-BODY PROBLEM (EPHE)

Using this model, [25] presents a comparison of the results in the EPHE reference frame with the ones in the simpler CR3BP and ER3BP reference frames. Table 3.1 underlines the importance of taking into account the eccentricity of the target orbit around the Sun, making the CR3BP unsuitable for the study of ballistic capture[2]. Moreover, for some celestial bodies, the inclusion of n-body perturbations leads to different solutions. Because of such considerations, used in defining the Case Studies given in Chapter 5, the development of a flow-informed strategy, suitable for models of different fidelities, is desirable. Finally, analysis like the one conducted in [25] justify the introduction of the RPRnBP.

System	Model	Mercury	Venus	Earth	Mars	Jupiter	Saturn
$\mathcal{R}_c$(‰)	CR3BP	0.020	0.118	0.148	0.203	0.311	0.182
	ER3BP	0.907	0.128	0.161	0.295	0.207	0.223
	EPHE	0.907	0.128	0.160	0.315	0.225	0.264
$\mathcal{S}_{min}(TU)$	CR3BP	3.037	7.367	9.277	15.180	56.809	77.823
	ER3BP	1248	7321	7837	10.143	38.421	71.065
	EPHE	1248	7229	7837	10.143	38.748	70.991

Table 3.1: Capture ratios and minimum stability indices for $\mathcal{C}^6_{-1}$, using different models. [25]

3.4.1. THE ROLE OF TARGET'S ECCENTRICITY

It can be seen (Figure 3.9) that, in general, considering the eccentricity of the target orbit around the Sun leads to larger capture sets. Moreover, for some planets, considering a full n-body problem leads to similar results, with respect to the ER3BP: when accurate enough, the choice of a simplified model should be preferred. Another conclusion is that the capture ratio $\mathcal{R}_c$ increases for increasing planetary eccentricity.

---

[2] More about this, in Section 3.4.1.

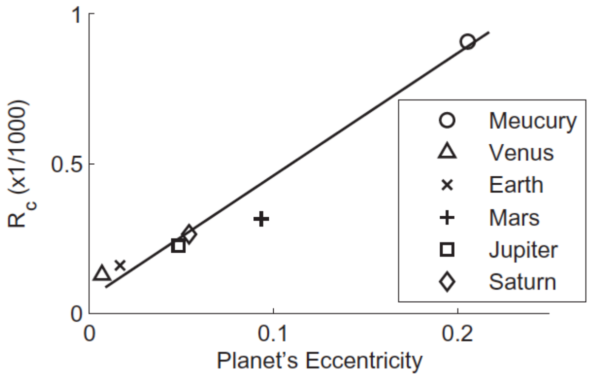

Figure 3.9: Capture ratio versus planetay eccentricity. Also a trendline is shown. [25]

3.4.2. THE ROLE OF TARGET'S TRUE ANOMALY

The previous results have been obtained considering the initial position of the planet to be at perihelion. When the planet true anomaly is allowed to change, larger capture sets (i.e., larger values of $\mathcal{R}_c$) are obtained when:

- the orbit is prograde and $f \in [\pi/2, 3/2\pi]$;
- the orbit is retrograde and $f \in [0, \pi/2] \cap [3/2\pi, 2\pi]$.

Moreover, as it can be seen in Figure 3.10, the Stability index is minimized for $f \in [0, \pi/2]$.

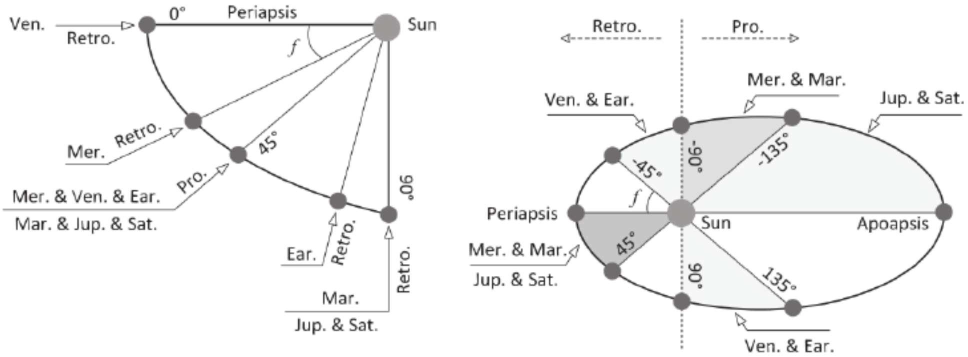

Figure 3.10: True anomalies of maximum $\mathcal{R}_c$ and minimum $\mathcal{S}_{min}$. [25]

3.4.3. THE ROLE OF PARTICLE'S INCLINATION AND ORIENTATION

The role of i_0 and Ω_0 has been investigated in the context of the ER3BP, since negligible discrepancies with higher quality models have been detected. The main results, that can also be inferred from Figure 3.11, 3.12, are:

- the out-of-plane component of motion is crucial for maximizing the chance for capture; two ranges of inclination maximize the capture ratio;
- the post-capture dynamics obtained from prograde orbits is, in general, more regular;
- the initial planes that maximize the chances of capture are the same that produce regular post-capture orbits.

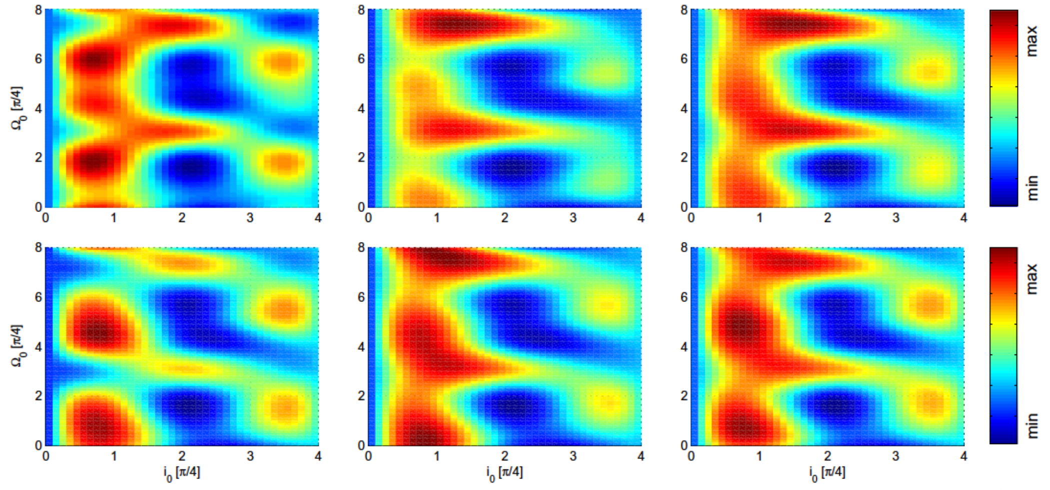

Figure 3.11: Capture ratio $\mathcal{R}_c$ as a function of i_0 and Ω_0 for different planets.[25]

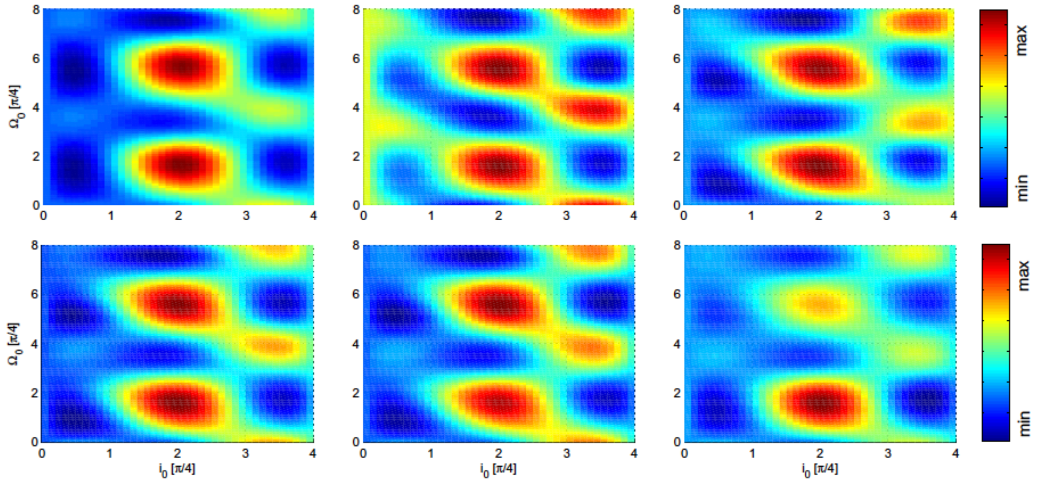

Figure 3.12: Minimum stability index $\mathcal{S}_{min}$ as a function of i_0 and Ω_0 for different planets. [25]

As anticipated, by taking into account these considerations and results, different case studies will be presented in Chapter 5.

3.5. IMPLEMENTATION: BISECTION METHOD

As previously discussed, the Capture Set is computed with a grid of points, expressed in polar coordinates, covering the region of the initial osculating orbital plane around the target body. In order to be able to accurately compute the Weak Stability Boundary, being a dense grid computationally infeasible, a bisection method has been implemented. It is important to state the assumption that made this choice reasonable: the possible Cantor-like structure of the WSB has not been considered in this work[3].

Once the initial osculating orbital plane is given (i.e. Ω and i), for a fixed value of the eccentricity, it is possible to select the argument of perigee ω of interest. In this way it is possible to compute a grid of initial conditions in r_p, and categorize their behaviour as a function of only one variable. The identification of the biggest r_p of the grid associated to a stable orbit, r_{p0}, together with the knowledge of the grid-size Δr, is necessary for the process initialization; the bisection method is described in Algorithm 1.

---

[3] This is addressed, together with its dynamical causes, in [39].

```
Result: $r_{WSB}$
$k = 0$ ;
$a = r_{p0}$, $b = r_{p0} + \Delta r$ ;
$x = (a+b)/2$ ;
$f_x = Stability(x)$ ;
while $(|b-a| > 10^{-10}$ || $f_x == 0)$ && $k < 100$ do
    if $f_x == 0$ then
        $b = x$;
        $x = (a+b)/2$ ;
        $f_x = Stability(x)$ ;
    else
        $a = x$;
        $x = (a+b)/2$ ;
        $f_x = Stability(x)$ ;
    end
    $k = k+1$ ;
end
$r_{WSB} = x$ ;
```

Algorithm 1: Bisection algorithm

In Algorithm 1:

- The *Stability* function, used to compute f_x, propagates the orbit associated to the initial condition given by x, and gives a binary output: 1 if the orbit is n-stable, 0 is it is n-unstable.
- The iteration is performed until convergence *and* until the computed condition is stable. The second condition is necessary, in order not to risk converging to an initial condition close to the WSB, but associated to an unstable orbit.

Based on the content of Chapter 4, this algorithm will be generalized, allowing to refine ω for a fixed r (and, in general, to refine a Kepler element, keeping fixed the other five); it will also be used to study the backward-in-time behaviour of the initial condition.
Finally, the process can be visualized in Figure 3.13:

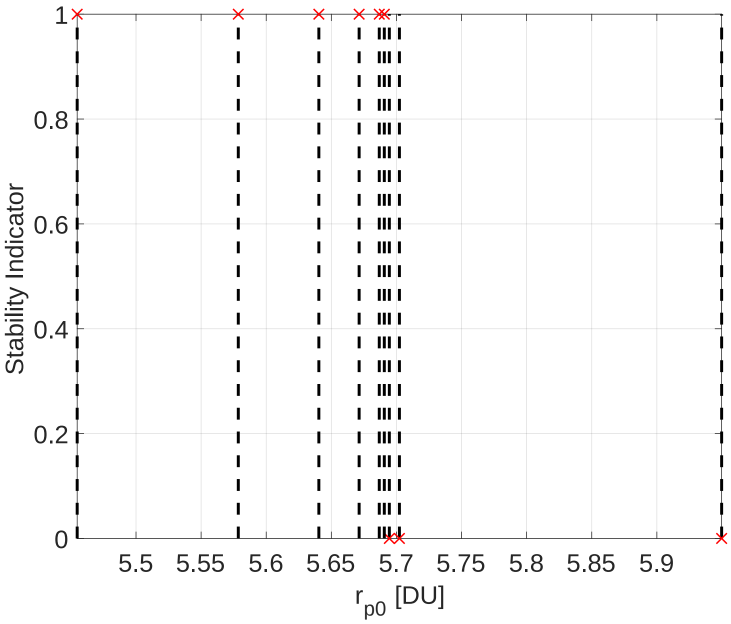

Figure 3.13: Bisection Algorithm

4

LAGRANGIAN COHERENT STRUCTURES

4.1. INTRODUCTION

The understanding of complex mechanical phenomena, modelled as nonlinear and non-autonomous dynamical systems, requires the development of specific tools: in these cases, as presented in Section 1.1.2, one cannot study the qualitative behaviour of the whole system via fixed points and associated invariant manifolds. In recent times, *Lagrangian Coherent Structures* (LCS) have been introduced: [40], [41], [17]. The word *Lagrangian* underlines the spacial evolution of such structures in time, distinguishing this approach from an Eulerian specification of the flow field.

The behaviour of an autonomous dynamical system, with respect to its initial condition, can be studied by looking at fixed points, periodic orbits, invariant manifolds and, from there, qualitatively categorize the motion. The structures presented in this chapter are an attempt to generalize the concept of invariant manifolds, identifying transport barrier, separating regions of the phase space with qualitatively different dynamics: such *Coherent Structures* "represent nearly invariant manifolds even in systems with arbitrary time dependence". [42]

Their utility in astrodynamics can, in some sense, be tracked back to [43][1]: studying the dynamic of a restricted problem as a function of the initial position in phase space is equivalent to study the flow-field of fluid particles in physical space.

It should be noted that Section 4.3 and Section 4.4 will introduce two concepts that are not going to be applied in order to produce results, nor to directly tackle the research questions. Their understanding has nevertheless been crucial in the development of appropriate flow-informed strategies for trajectory design.

4.2. FINITE-TIME LYAPUNOV EXPONENTS

In Section 2.3, the finite time Cauchy-Green Strain Tensor has been introduced; the shorthand definition $\Delta := \Delta(T; \mathbf{x}_0, t_0)$ will now be used. Being $\lambda_n(\Delta)$ its largest eigenvalue, the Finite-Time Lyapunov Exponent (FTLE) is a field defined by

$$\sigma_{t_0}^{T}(\mathbf{x}) = \frac{1}{|T|} \log \sqrt{\lambda_n(\Delta)} \tag{4.1}$$

This metric, measuring the stretching between close trajectories (for a fixed time interval), can be applied to flow analysis ([19] - Section 2.4): its ridges, informally defined as hyper-surfaces along which one sees a smaller change in the value of the scalar field than in directions transverse to it, play the role of invariant manifolds in autonomous dynamical system: they are an heuristic procedure to identify LCS. [40]

This observation, as explained in [44] and [15], is only statistically robust: such procedure ignores the direction of the eigenvector associated to the largest eigenvalue: it could generate also shearing deformations. Still, the fact that the flux across an LCS is negligible, [42], makes this object and interesting tool.

Because of the limitations of the FTLE field, Section 4.5.1 will present some criteria, introduced to distinguish between stretching and shearing deformations.

4.3. POINCARÉ & STROBOSCOPIC MAPS

Taking a section of the flow in $\mathbb{R}^n$ with a codimension-one surface, the map that naturally arises, called *Poincaré map*[2], is a powerful tool to study the general behaviour of a dynamical system (Figure 4.1). These maps can be viewed as dynamical

---

[1] Section 2.7 - Two-dimensional streamline analogy

[2] For an exahustive presentation, see [30], Section 4.12.

systems in which time is allowed to assume discrete values. In the context of the CR3BP, such mapping has been used to relate Invariant Manifolds with the Weak Stability Boundary. [45]

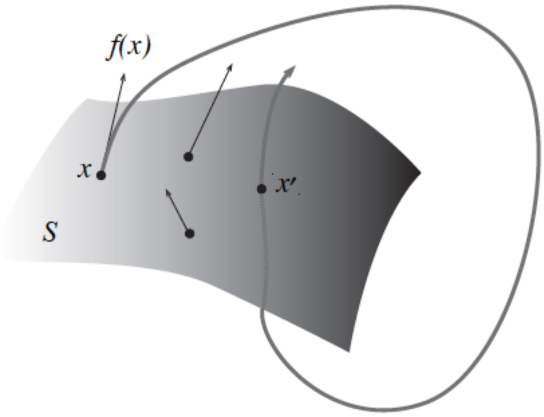

Figure 4.1: Poincaré map from a flow on a section S. [30]

A special case of a Poincaré map, that can be introduced for non-autonomous, periodic dynamical systems (with period T), is the *stroboscopic map*, in which the state of the system is studied in intervals of T time units.

4.4. FINITE-ITERATION LYAPUNOV EXPONENTS

In order to reduce the dimensionality of a four-dimensional problem and allow the representation of relevant results, [17] made use of Poincaré sections. With this approach, a given hyperplane $U \subset \mathbb{R}^4$ can be advected until the orbits intersect the hyperplane N times. From this, the Finite-Iteration Lyapunov Exponent (FILE) field

$$\sigma_{t_0}^{N}(\mathbf{x}) = \frac{1}{|N|} \log \left\| \frac{\mathrm{d}\mathbf{P}^N(\mathbf{x})}{\mathrm{d}\mathbf{x}} \right\| \tag{4.2}$$

can be computed; **P** is the Poincaré map associated with the hyperplane U and the flow Φ.

As anticipated, in the context of this work, Poincaré mapping is not going to be used: in fact, while representability remains an important focus of this work, the concept of FILE has been introduced because of its relation with the way in which capture orbits are categorized and, therefore, with the definition of the WSB. In fact, one could still consider the non-projected flow and introduce a *time-varying FTLE* field

$$\sigma_{t_0}^{T_N(\mathbf{x})}(\mathbf{x}) = \frac{1}{|T_N(\mathbf{x})|} \log \left\| \frac{\mathrm{d}\Phi_{t_0}^{T_N(\mathbf{x})}(\mathbf{x})}{\mathrm{d}\mathbf{x}} \right\| \tag{4.3}$$

where $T_N(\mathbf{x})$, being the time it takes for the propagated orbit to intersect a section of the phase space, is a function of the initial state.

With another conceptual step away from Poincaré mapping, it is possible to consider the intersection of the orbit in physical space with a variable 2D plane, defined by the initial condition of the orbit: this is what has been done for the computation of the capture set. In this way, each stable initial condition will be associated to a time T_N, necessary to perform N revolutions around the target body.

4.5. LCS - DEFINITION AND CLASSIFICATION

Now that different heuristics have been presented, it is possible to formally define Lagrangian Coherent Structures. They are characterized by two properties:

- LCS should be *material surfaces*[3]. They need to have sufficient dimension to have a visible impact on the dynamics and they must move with the flow;
- LCS should be characterized, locally, by the strongest attraction, repulsion or shear in the flow.

Their classification follows the classical invariant manifolds one:

- **Hyperbolic** LCS are the most attracting and repelling structures;

---

[3] See [46] for a formal definition of material surface.

- **Elliptic** LCS are closed material surfaces;
- **Parabolic** LCS are structures characterized by the strongest shearing.

As already stated in Chapter 1, this work deals with hyperbolic Lagrangian Coherent Structures *only*.

4.5.1. VARIATIONAL THEORY

As introduced in Section 4.2, ridges of FTLE are not always associated to underlying structures; moreover, LCS are not necessarily ridges of the FTLE field ([15] - Section 2.3). This Section will therefore present *sufficient and necessary* conditions for the existence of LCS.

For a given initial state $\mathbf{x}_0$ and an arbitrary co-dimension 1 material surface $\mathcal{M}(t)$, it is possible to introduce the tangent space $T_{\mathbf{x}_0}\mathcal{M}(t_0)$ and the one-dimensional normal space $\mathbf{n}_0 := N_{\mathbf{x}_0}\mathcal{M}(t_0)$.
Because of the properties of the linearised flow, the advected tangent space is tangent to $\mathcal{M}(t)$ in $\mathbf{x}_t = \phi^t_{t_0}(\mathbf{x}_0)$. On the other hand, the advected normal space in not necessarily defined in the normal space $N_{\mathbf{x}_t}\mathcal{M}(t)$ (Figure 4.2).

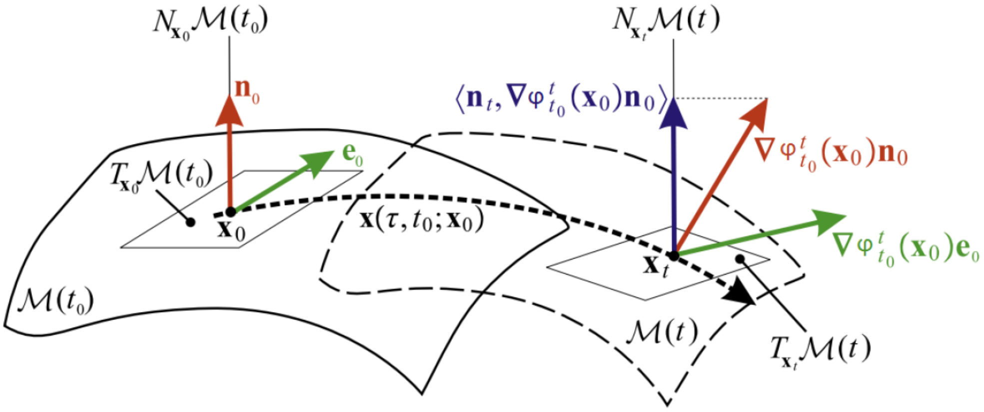

Figure 4.2: Advection of $\mathcal{M}(t_0)$, $T_{\mathbf{x}_0}\mathcal{M}(t_0)$ and $\mathbf{n}_0$. [15]

The advected normal space $D_{\mathbf{x}_0}\phi^t_{t_0}(\mathbf{x}_0)\mathbf{n}_0$ can be expressed by means of

$$D_{\mathbf{x}_0}\phi^t_{t_0}(\mathbf{x}_0)\mathbf{n}_0 = \rho^t_{t_0}(\mathbf{x}_0,\mathbf{n}_0)\cdot\mathbf{n}_t + \pi^t_{t_0}(\mathbf{x}_0,\mathbf{n}_0)\cdot T_{\mathbf{x}_t}\mathcal{M}(t) \tag{4.4}$$

where $\rho^t_{t_0}(\mathbf{x}_0,\mathbf{n}_0)$ is the *repulsion rate*. It can be computed by means of

$$\rho^t_{t_0}(\mathbf{x}_0,\mathbf{n}_0) = \frac{1}{\sqrt{\langle \mathbf{n}_0, \Delta^{-1}\mathbf{n}_0\rangle}} \tag{4.5}$$

where Δ^{-1} is the inverse of the CG strain tensor.

Recalling the observations given in Section 4.2, together with the repulsion rate, the *repulsion ratio* is defined, in order to assess which effect, between repulsion and shearing, is the dominant one. It can be computed by means of the following:

$$\nu^t_{t_0}(\mathbf{x}_0,\mathbf{n}_0) = \min_{|\mathbf{e}_0|=1} \frac{\rho^t_{t_0}(\mathbf{x}_0,\mathbf{n}_0)}{\sqrt{\langle \mathbf{e}_0, \Delta\mathbf{e}_0\rangle}}, \quad \mathbf{e}_0 \in T_{\mathbf{x}_0}\mathcal{M}(t_0) \tag{4.6}$$

It is moreover possible to report the sufficient and necessary conditions, given in [15], for a material surface to be a LCS, based on the invariants of the Finite-Time CG Strain Tensor:
"Given a compact material surface $\mathcal{M}(t) \subset U \subset \mathbb{R}^n$ over the time interval $[t_0, t_0+T]$, it is a repelling LCS over the given time interval *if and only if* the following hold for all $\mathbf{x}_0 \in \mathcal{M}(t_0)$":

- $\lambda_{n-1}(\mathbf{x}_0, t_0, T) \neq \lambda_n(\mathbf{x}_0, t_0, T) > 1$;
- $\xi_n(\mathbf{x}_0, t_0, T) \perp T_{\mathbf{x}_0}\mathcal{M}(t_0)$;
- $D_{\mathbf{x}_0}\lambda_n(\mathbf{x}_0, t_0, T)\cdot\xi_n(\mathbf{x}_0, t_0, T) = 0$;
- $\mathbf{L}(\mathbf{x}_0, t_0, T)$, given in Equation 4.7, is positive definite for all $\mathbf{x}_0 \in \mathcal{M}(t_0)$.

$$\mathbf{L}(\mathbf{x}_0,t_0,T)=\begin{bmatrix} D^2_{\mathbf{x}_0}\Delta^{-1}[\xi_n] & 2\frac{\lambda_n-\lambda_1}{\lambda_1\lambda_n}\left(\xi_1\cdot D_{\mathbf{x}_0}\xi_n\xi_n\right) & \cdots & 2\frac{\lambda_n-\lambda_{n-1}}{\lambda_{n-1}\lambda_n}\left(\xi_{n-1}\cdot D_{\mathbf{x}_0}\xi_n\xi_n\right) \\ 2\frac{\lambda_n-\lambda_1}{\lambda_1\lambda_n}\left(\xi_1\cdot D_{\mathbf{x}_0}\xi_n\xi_n\right) & 2\frac{\lambda_n-\lambda_1}{\lambda_1\lambda_n} & \cdots & 0 \\ \vdots & \vdots & \ddots & \vdots \\ 2\frac{\lambda_n-\lambda_{n-1}}{\lambda_{n-1}\lambda_n}\left(\xi_{n-1}\cdot D_{\mathbf{x}_0}\xi_n\xi_n\right) & 0 & \cdots & 2\frac{\lambda_n-\lambda_{n-1}}{\lambda_{n-1}\lambda_n} \end{bmatrix} \tag{4.7}$$

with

$$D^2_{\mathbf{x}_0}\Delta^{-1}[\xi_n]=-\frac{1}{\lambda_n^2}\left(\xi_n\cdot D^2_{\mathbf{x}_0}\lambda_n\xi_n\right)+2\sum_{q=1}^{n-1}\frac{\lambda_n-\lambda_q}{\lambda_n\lambda_q}\left(\xi_q\cdot D_{\mathbf{x}_0}\xi_n\xi_n\right)^2$$

2D DOMAINS

In the case of a 2-dimensional domain, the four conditions can be reformulated. Following the considerations given in [16], in order to also take into account numerical sensitivity and have a more robust implementation:
"Given a curve $\Gamma(t)\subset U\subset\mathbb{R}^2$, repelling LCS over the time interval $[t_0,t_0+T]$, for all $\mathbf{x}_0\in\Gamma(t_0)$":

1. $\lambda_1(\mathbf{x}_0,t_0,T)\neq\lambda_2(\mathbf{x}_0,t_0,T)>1$;
2. $\xi_2(\mathbf{x}_0,t_0,T)\cdot D^2_{\mathbf{x}_0}\lambda_2(\mathbf{x}_0,t_0,T)\xi_2(\mathbf{x}_0,t_0,T)<0$;
3. $\xi_1(\mathbf{x}_0,t_0,T)\parallel T_{\mathbf{x}_0}\Gamma(t_0)$;
4. $\overline{\lambda}_2(\Gamma(t_0))$, the average of λ_2 over $\Gamma(t_0)$, is maximal among all nearby curves $\gamma(t_0)$, such that their tangent at $\mathbf{x}_0$ is parallel to $\xi_1(\mathbf{x}_0,t_0,T)$.

4.6. STRAINLINES

Because of condition (3), given in Section 4.5.1, Lagrangian Coherent Structures are necessarily tangent to ξ_1: the eigenvector associated to the smallest eigenvalue λ_1 of the Cauchy-Green strain tensor $\Delta_{t_0}^{t_0+T}(\mathbf{x}_0)$. For a given two-dimensional projection of the phase space, such structures are 1-dimensional curves, called *strainlines*: [16] - p. 3.
A strainline $\gamma(t_0)\subset\Omega\subset\mathbb{R}^2$ is obtained solving the following Cauchy problem:

$$\begin{cases}\mathbf{x}'(s) & = & \xi_1(\mathbf{x}(s),t_0,T)\\ \mathbf{x}(0) & = & \mathbf{x}_0\in\Omega\\ |\xi_1| & = & 1\end{cases}\tag{4.8}$$

Following [16], the system of equations can be scaled:

$$\begin{cases}\mathbf{x}'(s) & = & \tilde{\xi}_1(\mathbf{x}(s),t_0,T)\\ \mathbf{x}(0) & = & \mathbf{x}_0\in\Omega\end{cases}\tag{4.9}$$

with

$$mathbf\tilde{\xi}_1(\mathbf{x}(s),t_0,T(s))=sign(\mathbf{x}(s))\alpha(\mathbf{x}(s))\xi_1(\mathbf{x}(s),t_0,T(s))\tag{4.10}$$

- $\alpha(\mathbf{x}(s))$, allowing to stop the procedure, if a degenerate point is approached, is given by

$$\alpha(\mathbf{x}(s))=\left(\frac{\lambda_2(\mathbf{x}(s))-\lambda_1(\mathbf{x}(s))}{\lambda_2(\mathbf{x}(s))+\lambda_1(\mathbf{x}(s))}\right)^2$$

- $sign(\mathbf{x}(s))$ ensure the smoothness of the strainline: in fact, at each integration step k, it is necessary for the tangent vector to verify

$$\tilde{\xi}_1(\mathbf{x}(s),t_0,T(s))\cdot\left(\mathbf{x}_{k-1}-\mathbf{x}_k\right)\geq 0$$

As given in [19] - Equation 5.1, the latter condition can be equivalently implemented by studying the eigenvector used for the previous integration step. Finally, in order to ensure the strainline to start in the direction of interest, with respect to the origin of the reference frame, the sign of the eigenvector associated to the first integration is modified, if necessary, in order to verify the following:

$$\mathbf{x}_k\times\tilde{\xi}_1(\mathbf{x}(s),t_0,T(s))>0$$

Since, as stated, strainlines associated to the FTLE field lead to the definition of ridges dividing the plane in dynamically distinct regions (at least statistically), and since the WSB displays a similar role in the categorization of stable and unstable orbits, [47] (Chapter 4) investigated the similarities between these two objects. The main advantage of doing so is that computing a LCS is, potentially, computationally less expensive then constructing a capture set: the separatrix can

be computed, starting from *one* initial point of the WSB, and reducing by one the dimensionality of the problem.
The work [47], whose results are shown in Figure 4.3, analysed the Capture Set of an Elliptic Restricted Three-Body Problem (ER3BP), characterized by:

- Mass parameter: $\mu = 3.226208 \times 10^{-7}$;
- Eccentricity of the primaries: $e_p = 0.093418$;
- Initial true anomaly of the primaries: $f_0 = 0$ rad.

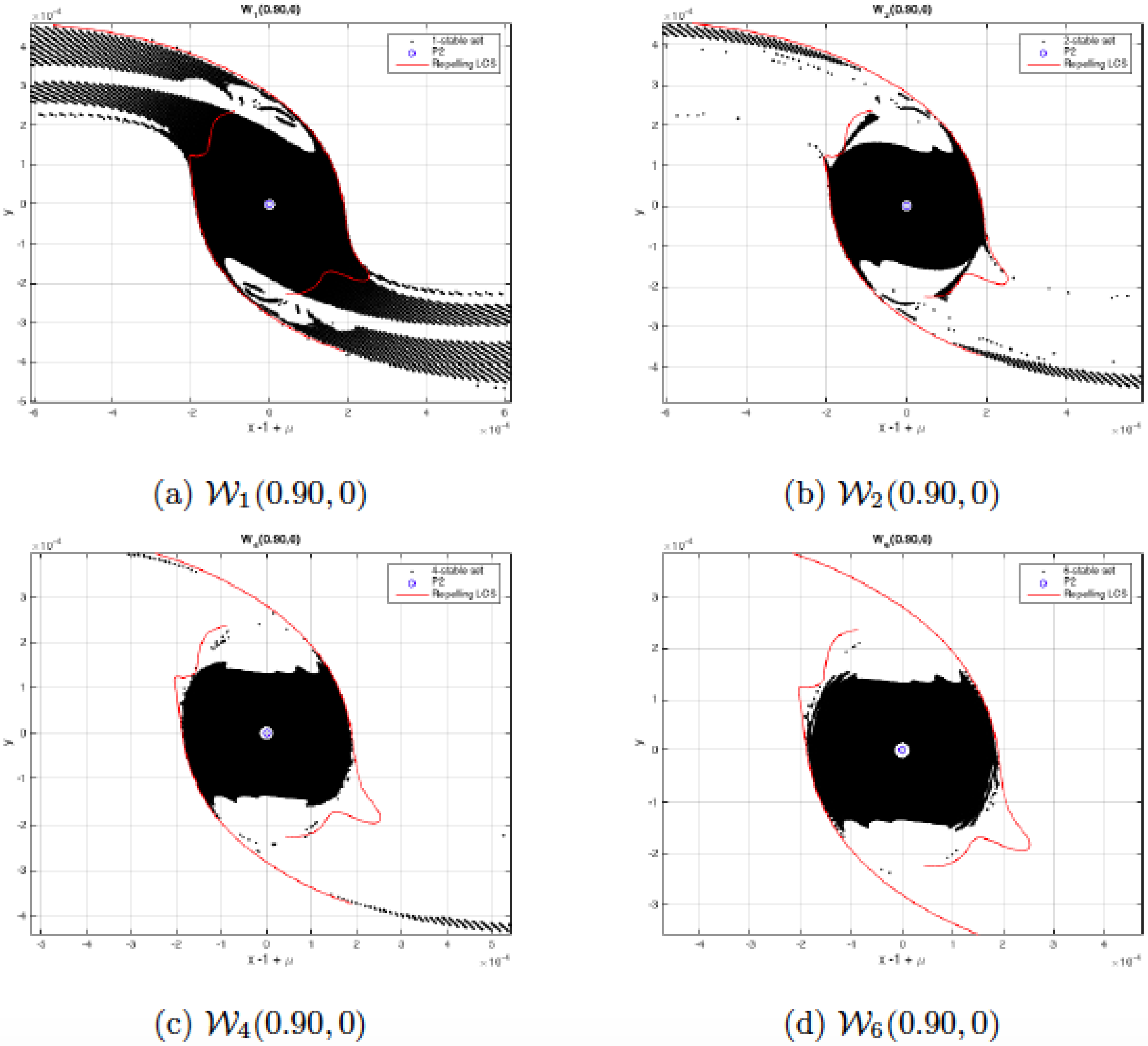

(a) $\mathcal{W}_1(0.90, 0)$

(b) $\mathcal{W}_2(0.90, 0)$

(c) $\mathcal{W}_4(0.90, 0)$

(d) $\mathcal{W}_6(0.90, 0)$

Figure 4.3: n-stable sets and repelling LCS for the Sun-Mars system. In some regions, the LCS bounds the Stable set. [47]

The use of the same strainline, for different n-stable sets, does not appear consistent with the way in which the different Stable Sets are computed. Moreover, as also [48] recently noticed, "poor matching is due to the fact that the LCS are computed using a fixed integration time, whilst the integration time of each particle in the stable set varies".

4.6.1. 2D PROJECTION

A number of works are focusing on the application of Lagrangian Coherent Structures in high degrees-of-freedom systems; however, because of the simplifications arising from the reduction of the dimensionality (Section 4.5.1), but also in order to be consistent with previous works (e.g., [47], [48]), a 2-dimensional flow will be considered here.
As previously discussed, the dynamical system is characterized by six degrees of freedom; some additional mapping needs

to take place in order for the Streamline to be defined in a 2D space, as Capture Sets with fixed eccentricity are. Generalizing the mapping introduced by [47] (Section 4.2.2), it is possible to introduce ψ, which is related to the physical flow by:

$$\psi = \pi \circ XX2S \circ I2XX \circ \phi \circ XX2I \circ S2XX \circ \mathcal{M}$$

It is representable by means of:

$$\begin{tikzcd}
\mathbb{R}^2 \arrow[r, "\mathcal{M}"] & \mathbb{R}^6 \arrow[r, "S2XX"] & \mathbb{R}^6 \arrow[r, "XX2I"] & \mathbb{R}^6 \arrow[r, "\Phi"] & \mathbb{R}^6 \arrow[r, "I2XX"] & \mathbb{R}^6 \arrow[r, "XX2S"] & \mathbb{R}^6 \arrow[r, "\pi"] & \mathbb{R}^2
\end{tikzcd}$$

$$\left\{\begin{array}{c} x_0^{OP} \\ y_0^{OP} \end{array}\right\} \mapsto \left\{\begin{array}{c} x_0^{OP} \\ y_0^{OP} \\ 0 \\ \dot{x}_0^{OP} \\ \dot{y}_0^{OP} \\ 0 \end{array}\right\} \mapsto \left\{\begin{array}{c} x_0^{XX} \\ y_0^{XX} \\ z_0^{XX} \\ \dot{x}_0^{XX} \\ \dot{y}_0^{XX} \\ \dot{z}_0^{XX} \end{array}\right\} \mapsto \left\{\begin{array}{c} x_0 \\ y_0 \\ z_0 \\ \dot{x}_0 \\ \dot{y}_0 \\ \dot{z}_0 \end{array}\right\} \mapsto \left\{\begin{array}{c} x_T \\ y_T \\ z_T \\ \dot{x}_T \\ \dot{y}_T \\ \dot{z}_T \end{array}\right\} \mapsto \left\{\begin{array}{c} x_T^{XX} \\ y_T^{XX} \\ z_T^{XX} \\ \dot{x}_T^{XX} \\ \dot{y}_T^{XX} \\ \dot{z}_T^{XX} \end{array}\right\} \mapsto \left\{\begin{array}{c} x_T^{OP} \\ y_T^{OP} \\ z_T^{OP} \\ \dot{x}_T^{OP} \\ \dot{y}_T^{OP} \\ \dot{z}_T^{OP} \end{array}\right\} \mapsto \left\{\begin{array}{c} x_T^{OP} \\ y_T^{OP} \end{array}\right\} \tag{4.11}$$

In Equation (4.11), OP stands for "Orbital Plane", identified by the initial osculating orbital parameters. Its x-axis (positive side) is associated to $\omega = 0$ rad. For a given value of the perigee distance r_p and its argument (i.e. given the polar coordinates), it is straightforward to obtain Cartesian coordinates of any point in such place, which are used as an input for the given mapping.

- The function $\mathcal{M}$ allows to compute the velocity vector, in the same reference frame, for a given value of the eccentricity. The velocity vector at perigee is given by
$$\mathbf{V_p} = V\mathbf{e_V}$$
with
$$V_p = \sqrt{\frac{1+e}{r_p}}, \quad \mathbf{e_V} = [-e_{r2}, e_{r1}], \quad \mathbf{e_r} = \frac{1}{r_p}[e_{r1}, e_{r2}]$$
Since the z-component of both the position and velocity vectors is zero, it is possible to obtain the initial state of the spacecraft in the OP reference frame;
- S2XX is a reference frame transformation, relating the orbital plane with a generic reference frame, XX, the one with respect to which the orbital parameters of the spacecraft are defined. As discussed in the previous chapters, one may be interested in defining the initial osculating orbital plane with respect to some non-inertial reference frame (e.g., RTN@t_0), and this intermediate transformation is therefore necessary. This linear transformation is given by ([23], Section 11.8)
$$S2XX = \begin{bmatrix} \eta & 0_{3x3} \\ 0_{3x3} & \eta \end{bmatrix}$$
with $\eta = AB$,
$$A = \begin{bmatrix} \cos\Omega & -\sin\Omega & 0 \\ \sin\Omega & \cos\Omega & 0 \\ 0 & 0 & 1 \end{bmatrix}, \quad B = \begin{bmatrix} 1 & 0 & 0 \\ 0 & \cos i & -\sin i \\ 0 & \sin i & \cos i \end{bmatrix}$$
XX2S is its inverse transformation;
- XX2I is the reference frame transformation relating XX, in which the state of the spacecraft is given, with I, the inertial reference frame, in which the equations of motion are formulated. The different relations, depending on which XX is used, are given in Chapter 2. I2XX is its inverse transformation. Of course, in the case in which the generic XX frame is inertial, the XX2I transformation is the identity.
- ϕ is the flow of the system, described by the equations given in Chapter 2;
- π is the projection from the state to the 2D position, simply given by
$$\pi(x, y, z, \dot{x}, \dot{y}, \dot{z}) = (x, y)$$
It should be underlined that here the OP reference plane is not identified by the osculating orbital parameters at epoch T, but its the same given above.

ψ is therefore a 2D flow, and its strainlines can easily be computed. Being the strainlines associated to this mapping, and not to ϕ, the Cauchy-Green strain tensor is given by

$$\Delta = \Psi^T \Psi \tag{4.12}$$

where Ψ is the Jacobian of ψ. The Jacobian of this 2D-flow is computed using the chain rule:

$$\Psi = J_\psi = J_\pi J_{S2XX}^T J_{XX2I}^T \Phi J_{XX2I} J_{S2XX} J_{\mathcal{M}} \tag{4.13}$$

- Φ, the State Transition Matrix, is computed propagating the variational equations of the system, as discussed in Section 2.3;
- Because S2XX and XX2I are linear transformations and, in particular, rotations, their Jacobian is given by the rotation matrix itself, and their inverse is equal to their transpose;
- The Jacobian of the projection is given by

$$J_\pi = \begin{bmatrix} 1 & 0 & 0 & 0 & 0 & 0 \\ 0 & 1 & 0 & 0 & 0 & 0 \end{bmatrix}$$

- The Jacobian of $\mathcal{M}$, computed analytically, is given by:

$$J_{\mathcal{M}} = \begin{bmatrix} 1 & 0 \\ 0 & 1 \\ 0 & 0 \\ \frac{\partial \dot{x}}{\partial x} & \frac{\partial \dot{x}}{\partial y} \\ \frac{\partial \dot{y}}{\partial x} & \frac{\partial \dot{y}}{\partial y} \\ 0 & 0 \end{bmatrix} \tag{4.14}$$

with

$$\begin{aligned} \frac{\partial \dot{x}}{\partial x} &= \sqrt{1+e}\frac{3xy}{2(x^2+y^2)^{7/4}} \\ \frac{\partial \dot{y}}{\partial y} &= -\sqrt{1+e}\frac{3xy}{2(x^2+y^2)^{7/4}} \\ \frac{\partial \dot{x}}{\partial y} &= \sqrt{1+e}\left(\frac{3y^2}{2(x^2+y^2)^{7/4}} - \frac{1}{(x^2+y^2)^{3/4}}\right) \\ \frac{\partial \dot{y}}{\partial x} &= \sqrt{1+e}\left(\frac{1}{(x^2+y^2)^{3/4}} - \frac{3x^2}{2(x^2+y^2)^{7/4}}\right) \end{aligned} \tag{4.15}$$

REPRESENTATION IN DIFFERENT SPACES

The modularity of the process allows to change the investigated space, without varying the core of the process.
An alternative mapping (that may require a generalization in the definition of the Stable Set) is presented here. For fixed values of e, ω, r_p, one can study how the stability is influenced by Ω, the Right Ascension of the Ascending Node and i, the inclination. The choice of these two variables was driven by Figure 3.11 and 3.12.

In order to do this, only the outer functions of the given mapping need to be changed:

$$\psi = \pi_{i\Omega} \circ XX2K \circ I2XX \circ \Phi \circ XX2I \circ \mathcal{M}_{i\Omega}$$

Representable by means of:

$$\mathbb{R}^2 \xrightarrow{\mathcal{M}_{i\Omega}} \mathbb{R}^6 \xrightarrow{XX2I} \mathbb{R}^6 \xrightarrow{\Phi} \mathbb{R}^6 \xrightarrow{I2XX} \mathbb{R}^6 \xrightarrow{XX2K} \mathbb{R}^6 \xrightarrow{\pi_{i\Omega}} \mathbb{R}^2$$

$$\left\{ \begin{matrix} i_0 \\ \Omega_0 \end{matrix} \right\} \mapsto \left\{ \begin{matrix} x_0^{XX} \\ y_0^{XX} \\ z_0^{XX} \\ \dot{x}_0^{XX} \\ \dot{y}_0^{XX} \\ \dot{z}_0^{XX} \end{matrix} \right\} \mapsto \left\{ \begin{matrix} x_0 \\ y_0 \\ z_0 \\ \dot{x}_0 \\ \dot{y}_0 \\ \dot{z}_0 \end{matrix} \right\} \mapsto \left\{ \begin{matrix} x_T \\ y_T \\ z_T \\ \dot{x}_T \\ \dot{y}_T \\ \dot{z}_T \end{matrix} \right\} \mapsto \left\{ \begin{matrix} x_T^{XX} \\ y_T^{XX} \\ z_T^{XX} \\ \dot{x}_T^{XX} \\ \dot{y}_T^{XX} \\ \dot{z}_T^{XX} \end{matrix} \right\} \mapsto \left\{ \begin{matrix} a_T \\ e_T \\ i_T \\ \omega_T \\ \Omega_T \\ f_T \end{matrix} \right\} \mapsto \left\{ \begin{matrix} i_T \\ \Omega_T \end{matrix} \right\} \tag{4.16}$$

Here $\mathcal{M}_{i\Omega}$ is the transformation that gives, for fixed values of r_p, e, ω, f, the relation between (i, Ω) and the Cartesian state, expressed in the same reference frame (XX). For this, the SPICE built-in function *cspice_conics* has been used.
XX2K is the inverse transformation, giving the Kepler elements as a function of the Cartesian State. Using again SPICE, this is given by *cspice_oscelt*.
The Jacobians of these transformation have been computed numerically, allowing to compute the CG Strain Tensor associated to a different space that, limited to the $[0,\pi]\times[0,2\pi]$ region, is associated to the surface of a sphere in physical space.

The presented transformation is just an example; it should now be clear how general the procedure is and how straightforward, because of the modularity of the process, it is to analyse different 2D subsets of the phase space.

4.6.2. STROBOSCOPIC STRAINLINES

Inspired by the introduction of a relation between strainlines and Finite Iteration Lyapunov Exponent, *Stroboscopic Strainlines* can now be defined. The introduction of this object is the core of this work. The name comes from the fact that each point of the strainline is associated to a different time, associated to the orbit of the spacecraft around the target body. While it should be noted that the motion of the spacecraft is not properly periodic, this name should capture the main idea, at the same time showing how it has has been formulated.

A Stroboscopic Strainline, again given by $\gamma(t_0) \subset \Omega \subset \mathbb{R}^2$, is the solution to a more general Cauchy problem:

$$\begin{cases} \mathbf{x}'(s) & = & \xi_1(\mathbf{x}(s), t_0, T(s)) \\ \mathbf{x}(0) & = & \mathbf{x}_0 \in \Omega \\ |\xi_1| & = & 1 \end{cases} \tag{4.17}$$

The innovation of this work lies in the fact that, in the first equation of (4.17), the integration time $T(s)$ is a function of the independent variable s through $\mathbf{x}(s)$: recalling the definition of stability given in Section 3.2.2, $T(s)$ is the final integration time of an n-stable orbit in physical space.

This generalization allows to relate the concept of Lagrangian Coherent Structures with the way in which capture orbits are defined. The utility of this tool, in the study of the phenomenon, should be now clear: the concept of *Weak Stability Boundary*, presented in Chapter 3 is expected to be strictly related to the stroboscopic streamline here introduced.

4.7. IMPLEMENTATION

Figure 4.4 shows the conceptual steps, taken for the computation of the strainlines:

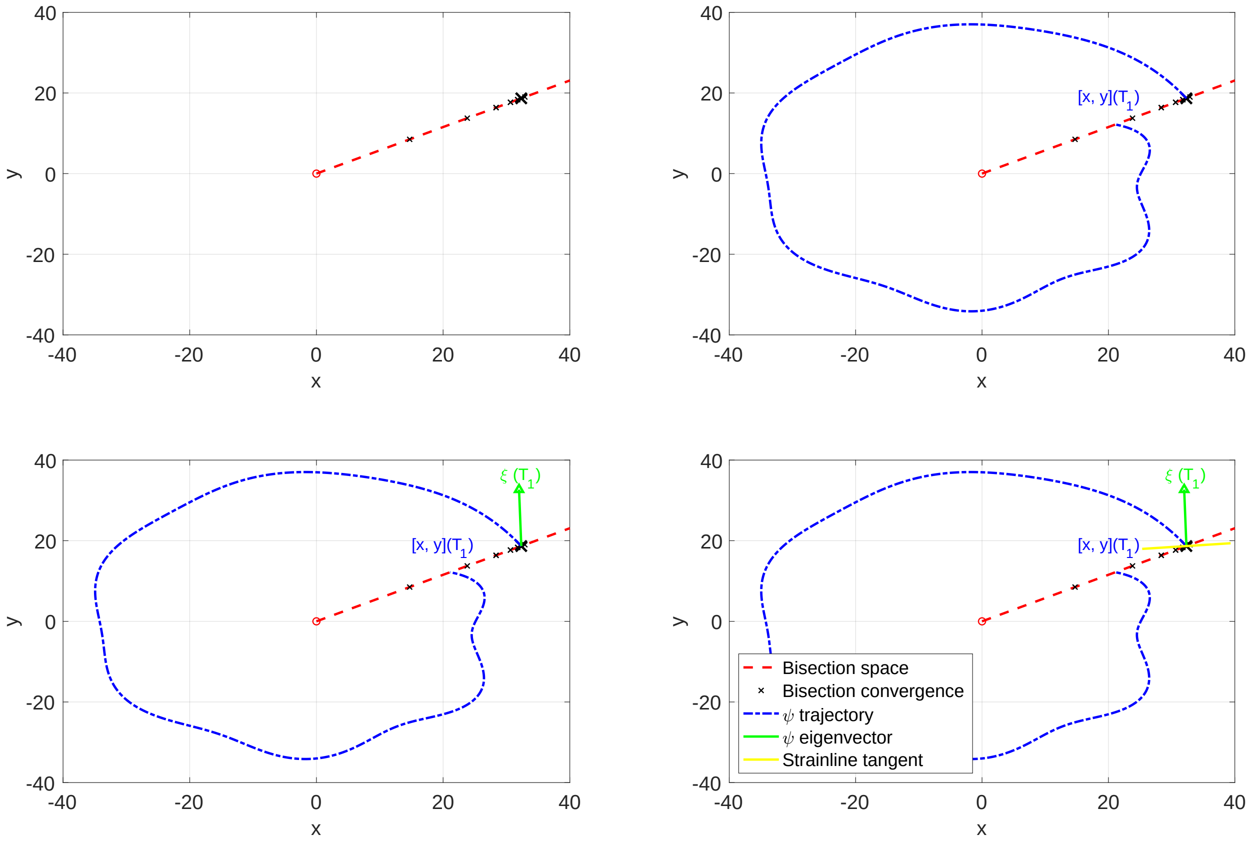

Figure 4.4: Stroboscopic Strainlines - Conceptual Steps

1. First, a bisection algorithm is applied on a 1-dimensional space, in order to find a point on the Weak Stability Boundary. In the schematic representation of Figure 4.4, this is performed varying the radius of perigee, for a constant argument ω. As discussed in Section 4.7.1, however, also the opposite is possible.

2. Once the initial point is obtained, the spacecraft can be propagated under ϕ, until n revolutions around the target body are performed (or until the escape condition is satisfied). It should be noted that time T_1 comes from the investigation of ϕ, not ψ.

3. The variational equations are propagated until time T_1, and the Jacobian of ψ, at such epoch, is used to compute the CG strain tensor, together with its eigenvectors.

4. The identification of the eigenvector associated to the biggest eigenvalue allows to identify the tangent to the strainline in the initial point.

This routine, also given in Algorithm 2, is therefore used to compute the tangent to the strainline on every point: its integration solves Equation (4.17), leading to the Stroboscopic Strainline computation.
The same integrator used for the propagation of the orbits has been used to compute the strainline: for different cases, its length, absolute and relative tolerance have been varied; their values will be presented in the following Chapter.

```
Result: $\mathbf{x}'(s)$
$\mathbf{x}_0^s = [r_{WSB}\cos\omega_{WSB}, r_{WSB}\sin\omega_{WSB}]$ ;
$\mathbf{x}_0^{OP} = \mathcal{M}(\mathbf{x}_0^s)$ ;
$\mathbf{x}_0^{XX} = S2XX(\mathbf{x}_0^{OP})$ ;
$\mathbf{x}_0 = XX2I(\mathbf{x}_0^{XX})$ ;
$T_n(\mathbf{x}_0)$: Orbit Integration and analysis ;
$\Phi(T_n)$: Variational Equations integration ;
$\Psi = J_\psi = J_\pi J_{S2XX}^T J_{XX2I}^T \Phi J_{XX2I} J_{S2XX} J_{\mathcal{M}}$ ;
$\Delta = \Psi^T \Psi$ ;
$(\xi_1, \xi_2, \lambda_1, \lambda_2)$: $\Delta$ Eigendecomposition ;
$\tilde{\xi}_1(\mathbf{x}(s), t_0, T(s))$: Equation (4.10) ;
$\mathbf{x}'(s) = \tilde{\xi}_1(\mathbf{x}(s), t_0, T(s))$ ;
```

Algorithm 2: Strainline tangent computation

The notation $\mathbf{x}^s$ has been here used to identify the position on the 2D plane, not to be confused with the associated state of the spacecraft in physical space, $\mathbf{x}$.

4.7.1. INITIALIZATION AND BISECTION: GENERALIZATION

The streamline is integrated into segments and, because of this, the streamline integration process is (re-)initialized. The main reasons for doing so are:

- avoiding divergence associated to numerical instability, while maintaining an integration tolerance leading to feasible computation times;

- allow the process to identify a new boundary, once the strainline reaches a point in the vicinity of which no stable orbit exists.

The initial point of the new segment is obtained with a Bisection method (Section 3.5) that requires an initial guess as well. This is obtained using a local grid search, made of 150 samples equally spaced; for the first strainline segment and if the local grid search does not lead to the identification of stable orbits, a wider grid search is performed, using 100 equally spaced values of $r_p \in [1, 50]$. The value of argument of perigee, for this, is fixed, and given by

$$\omega = \text{atan2}(y_f, x_f)$$

where atan2 is a four quadrant inverse tangent and y_f, x_f are the coordinates of the final point of the previous strainline segment.

In order to select which variable, between r_p and ω, is used as a constant during the following bisection algorithm, the local grid search is performed using the variables initialization given in Algorithm 3:

```
$\alpha = \text{atan2}(\xi_{f2}, \xi_{f1})$ ;
$\beta = \text{atan2}(y_f, x_f)$ ;
$R = \sqrt{x_f^2 + y_f^2}$ ;
if $|mod(\alpha,\pi) - mod(\beta,\pi)| < 20.0°$ then
    $r_p = R$ ;
    $\omega = \beta + linspace(-5°, 5°, 150)$ ;
else
    $\omega = \beta$ ;
    $\mathbf{r}_p = R + linspace(-0.1, 0.1, 150)$ ;
end
```

Algorithm 3: Generalized initialization algorithm

where

- ξ_f is the eigenvector of the Cauchy-Green tensor associated to the final integration step of the previous strainline segment.
- α allows to compute the local direction of the previous strainline segment at its final point; β gives the angular position of the final point of the previous strainline segment.
- R and β therefore identify the point, in polar coordinates, around which a local grid search should be performed: which of the two variables (radius and argument of perigee) has to be used is decided using the if-condition given above: if the strainline is close-to-radial, the search should be performed varying ω; r_p otherwise.

Once the set of orbits, associated to the set of initial conditions given by Algorithm 3, is propagated, the inputs for the following bisection algorithm can be identified. Because of presented variable generalization, this can be given by ($\omega = \beta, r_{p0}, \Delta r$) or by $r_p = R, \omega_0, \Delta\omega$. For the latter case, in which the search is performed along an arc of fixed radius, the bisection procedure is given in Algorithm 4.

```
Result: $\omega_{WSB}$
$k = 0$ ;
$a = \omega_0$, $b = \omega_0 + \Delta\omega$ ;
$x = (a+b)/2$ ;
$f_x = Stability(x)$ ;
while ($|b-a| > 10^{-10}$ || $f_x == 0$) && $k < 100$ do
    if $f_x == 0$ then
        $b = x$;
        $x = (a+b)/2$ ;
        $f_x = Stability(x)$ ;
    else
        $a = x$;
        $x = (a+b)/2$ ;
        $f_x = Stability(x)$ ;
    end
    $k = k+1$ ;
end
$\omega_{WSB} = x$ ;
```

Algorithm 4: Bisection algorithm: ω case.

This is done because, as shown in the preliminary result given in Figure 4.5, as soon as the strainline becomes (close to) radial, the refinement used to reinitialize the strainline leads to diverging from the WSB. Moreover, once the strainline leaves the vicinity of the WSB, reaching an unstable region, the algorithm is not able to find the time associated to the stability in that point, and it breaks down (as displayed in the top-left corner of the second plot).

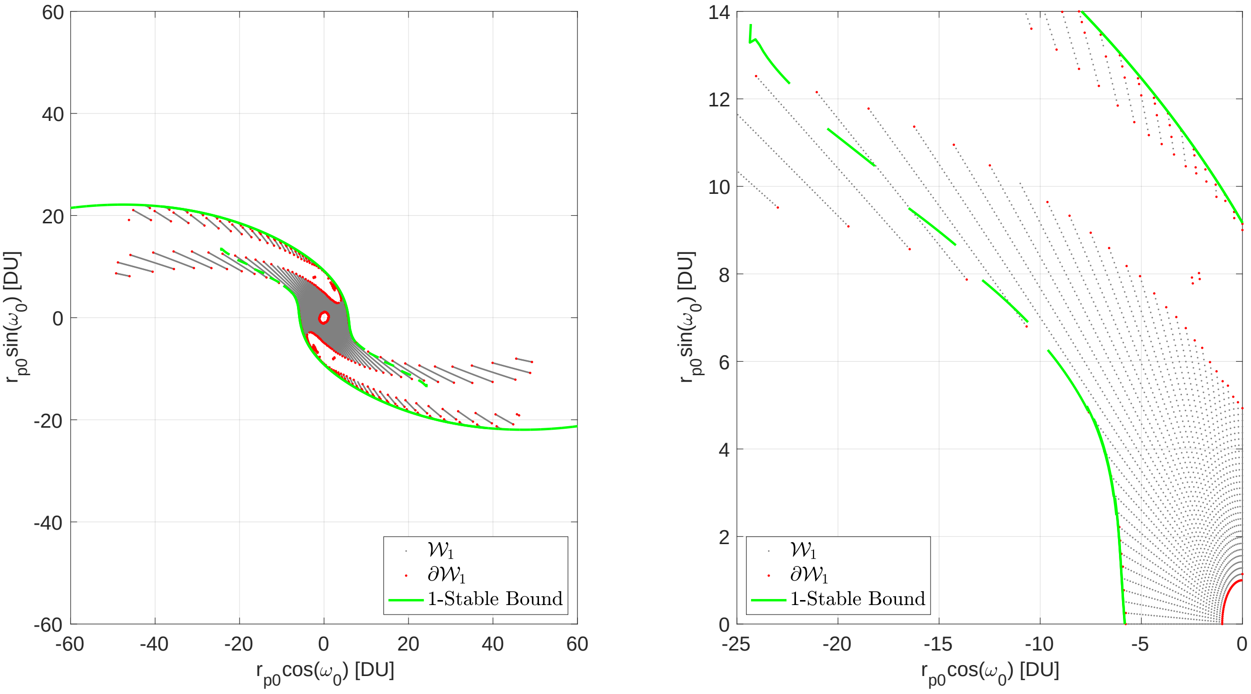

Figure 4.5: Preliminary result, motivating a generalized refinement.

5

RESULTS

5.1. INTRODUCTION

In this chapter, various results, coming from the application of the developed tools for different problems, will be given. The first part of the chapter will present the capture sets associated to different models. The chapter will then focus on the application of *Stroboscopic strainlines*, introduced in Chapter 4, to compute, for different problems and conditions, the *Weak Stability Boundary*. This will be done for different numbers of revolutions, both forward and backward in time. Moreover, the definition of the Capture Set will be translated geometrically, by computing the intersection of -1-Unstable and n-Stable Stroboscopic Strainlines; finally, some orbits associated to the computed Capture Sets will be given.

5.1.1. CASE STUDIES DEFINITION

Different simulations have been set up, mainly in order to test the robustness of the introduced technique with respect to different choices of model fidelities. For continuity reasons with respect to the majority of previous works in the field (e.g., [27], [47]), Mars has been chosen as the target body, located at the origin of the reference frame.

- Case 1:
  As a first case study, the initial epoch (i.e. Mars' position along its orbit) has been randomly selected: In UTC, the epoch is: 6^{th} September $2020, 10:40:00.0$, corresponding to $T_0 = 6.526608692 \times 10^8$ seconds past J2000. Its dynamics is closely related to a planar elliptic restricted three-body problem: in fact, while real ephemerides have been used, only the gravitational influence of Mars and of the Sun have been considered. Moreover, since the inclination of the set of initial osculating orbital parameters, expressed in a radial-tangent-normal reference frame, is zero, the initial osculating orbit always lies in the plane of the two primaries.
  The set of initial conditions, again expressed in a Mars-centered RTN reference frame, are given by:

  $$e = 0.95;$$

  $$\Omega = \theta = i = 0 \;\; rad;$$

  The 2D grid of initial states is given, in terms of radius [DU] and argument of perigee [deg], by:

  $$r_p = \{1, 1+49/348, 1+2\cdot 49/348 \ldots 50\}, \quad \omega = \{0, 2.5, 5\ldots 357.5\} \tag{5.1}$$

  This grid will be used for the following cases as well.

  The choice of an highly eccentric orbit comes from energetic considerations: numerical experimentation shows that, while close-to-circular orbits are highly stable, forward in time, their -1-escape set $\mathcal{X}_{-1}$ is small, leading to small capture sets.
- Case 2:
  For the second case study, only the initial epoch of the simulation has been modified, such that Mars is at its perihelion, at the initial simulation epoch. This is therefore set at 3^{rd} August $2020, 04:43:14.5$, corresponding to $T_0 = 6.497018637 \times 10^8$ seconds past J2000. This value can be obtained, making use of the SPICE $spkpos\_s$ function, and looking for the epoch associated to the minimum distance between Mars and the Sun.
  This condition has been selected because, as given in [22], configurations with the planet at aphelion or perihelion are of particular interest, favouring the capture phenomenon.
- Case 3:
  With respect to the previous case, perturbations have been included, while Mars is still located at its perihelion, at

the initial simulation epoch. In order to define the dynamical model, the environmental analysis performed in [27] (Section 4.6) has been taken as a reference. While such analysis is only a preliminary one, making use of a number of assumptions, it is enough to define a hierarchy of influence, and to therefore select the main environmental features. The environment of this case study can has been modelled taking into account, in order of importance:

- Mars point-mass gravity;
- Sun point-mass gravity;
- Solar Radiation Pressure;
- Phobos and Deimos point-mass gravity;
- Mars spherical harmonics, up to degree and order 20;
- Earth point-mass gravity;
- Jupiter point-mass gravity.

It should be underlined that, for planetary systems such as Jupiter, the considered position is the barycenter of the whole system, not just the central body's one.

While, following the same analysis (Figure 5.1), [27] included all planets, from Mercury to Neptune, in the context of this work only the main ones have been considered: in fact, the aim of this work is not *primarily* to compute accurate capture orbits, but to demonstrate the robustness and flexibility of the proposed technique, with respect to models of different fidelities.

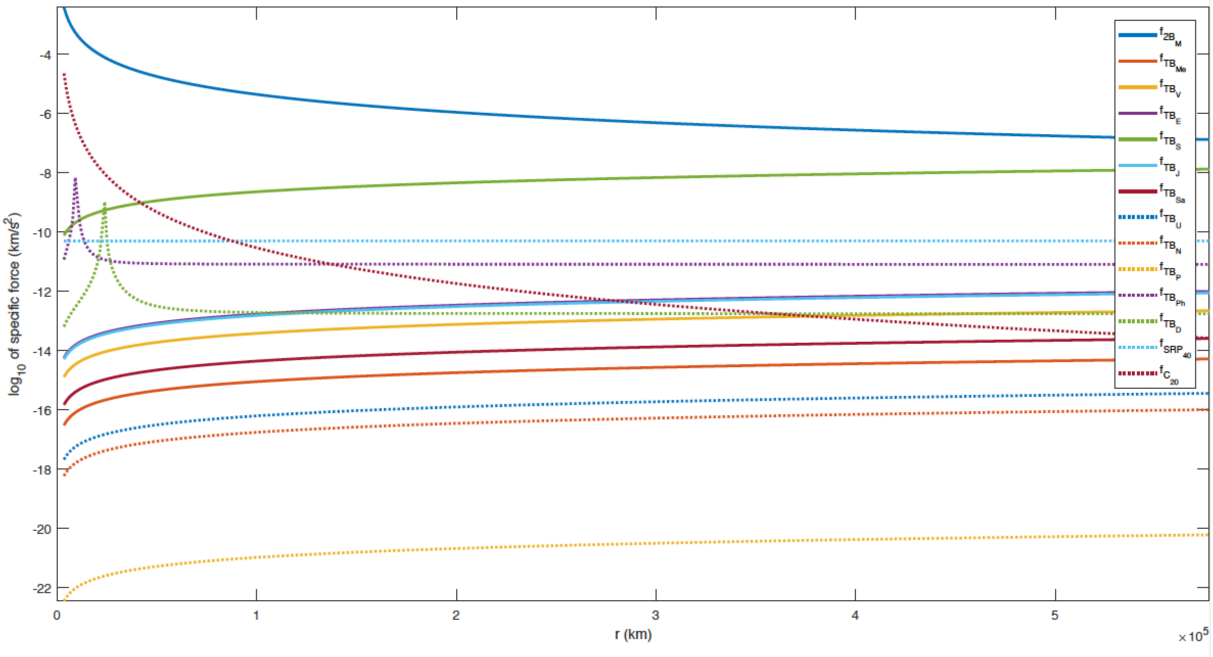

Figure 5.1: Environmental analysis, in the vicinity of Mars, of [27]. Accelerations are due to: Mars, Mercury, Venus, Earth, Sun, Jupiter, Saturn, Uranus, Neptune, Pluto, Phobos, Deimos, SRP (mass-to-area ratio = 40 kg/m^2), NSG (up to degree and order 20).

- Case 4:
  The same perturbations and initial simulation epoch, introduced in the previous case, define the dynamical model used here. Here, the orbital plane of the initial osculating orbit of the spacecraft is inclined with respect to the one in which Mars and the Sun lie. In fact, as discussed in Section 3.4.3 and shown in Figures 3.11, 3.12, the inclination and the Right Ascension of the Ascending Node have a big influence on the capture phenomenon. Because of this, the inclination and the RAAN of the initial osculating orbit, for this case, are be given by:

$$i = 0.7 \cdot \frac{\pi}{4} = 31.5\,\text{deg}$$

$$\Omega = \frac{\pi}{4} = 45\,\text{deg}$$

  In fact, both values are associated to high values of the capture ratio (i.e., capture is more likely to occur).

As previously discussed, the computation of the Capture Set involves the study of the dynamics both forward and backward in time: this will be done, separately, in the following sections.

5.2. FORWARD STABILITY

Before introducing Stroboscopic Strainlines, the results of the GRATIS toolbox alone will be given: for each case study, the 1-Stable, 2-Stable, 4-Stable and 6-Stable Sets will be given. All the results have been obtained from the propagation of 50400 initial conditions, defined by the polar coordinates introduced in the previous section. The following plots will also make use of the Normalized Stability Index, introduced in Section 3.3.2.

5.2.1. CASE 1

Figures 5.2 and 5.3 show the Stable Sets of the first case study. A relevant consideration is that the stable set is not a connected one, and it is not possible to define all of its points looking for *one* boundary; the majority of its points are nevertheless connected, and the computation of the "main" Weak Stability Boundary allows for a good approximation of the set of stable solutions.

One should also notice that the non-connected regions of the set are characterized, on average, by an higher Normalized Stability Index: this implies that the orbits associated to such points are highly non-Keplerian.

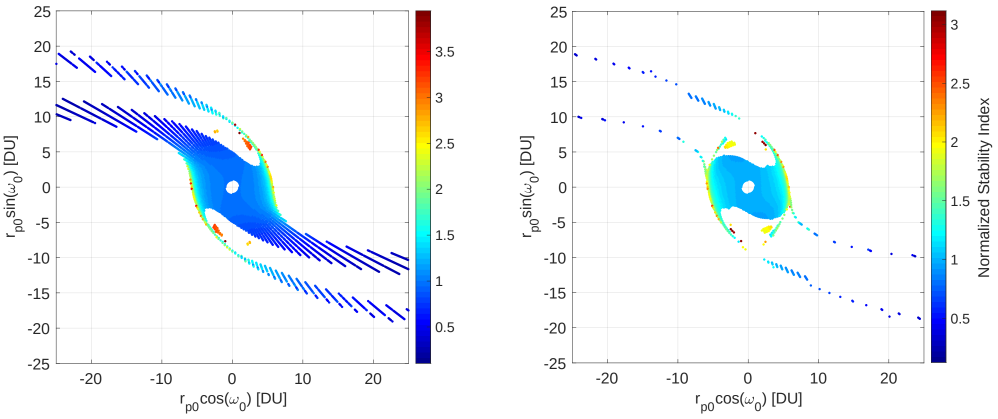

Figure 5.2: 1-stable and 2-stable sets of Case Study 1 and their Normalized Stability Index

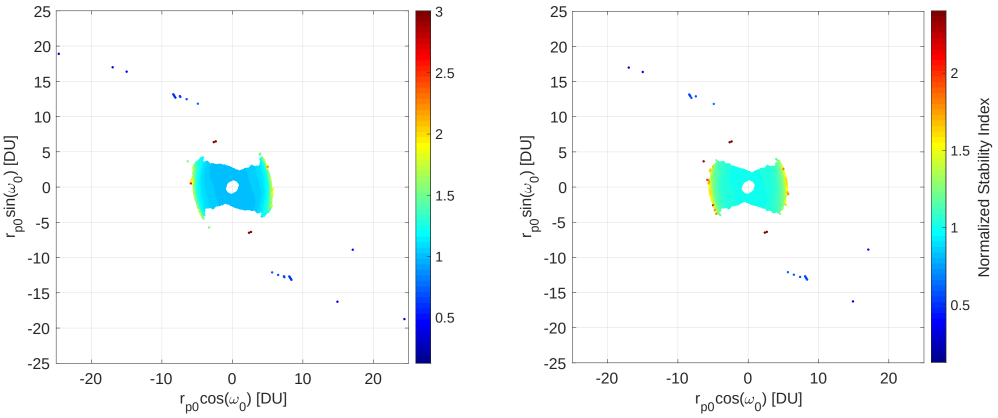

Figure 5.3: 4-stable and 6-stable sets of Case Study 1 and their Normalized Stability Index

The propagations necessary to build these sets required a computation time of approximately 4 hours. The machine used for all the simulations is made of 80 "Intel(R) Xeon(R) CPU E5-4620 v4 @ 2.10GHz" processors, each with a cache size of 25600 KB. If not differently stated, each simulation, by means of parallel computing, made use of approximately 10 processors.

5.2.2. CASE 2

The same considerations given above hold for Figures 5.4 and 5.5 as well. The propagations required approximately 4.4 hours; because the model is the same, the computations necessary to obtain a Stable Set with the same size are of the same order of magnitude as the previous case.

For all the n-stable sets considered in these first two cases, the Normalized Stability Index increases in the vicinity of the Weak Stability Boundary. This, however, appears to be true only for small values of r_{p0}, and for certain intervals of ω_0. It is not clear whether or not the former limitation is a consequence of the fact that the grid gets less dense for greater values of r_{p0}, leading to a less accurate estimation of the n-Stable set. Nevertheless, the latter limitation, which can be appreciated by looking at the internal limit of the 1-Stable Sets, is interesting from a dynamical point of view.

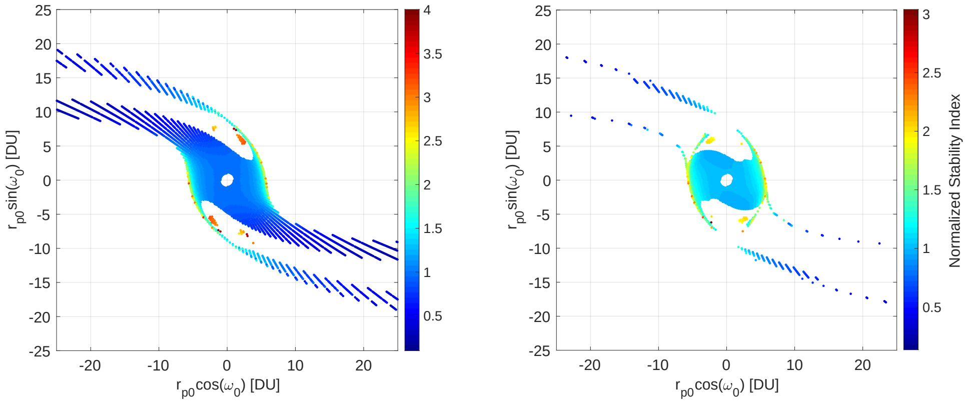

Figure 5.4: 1-stable and 2-stable sets of Case Study 2 and their Normalized Stability Index

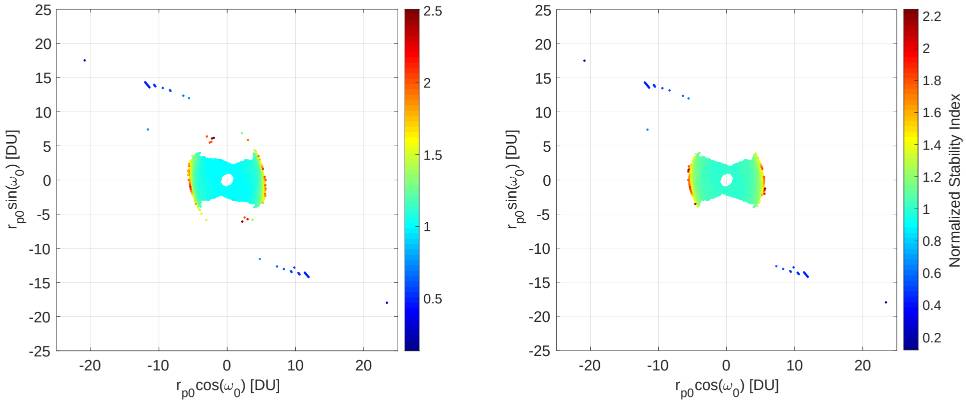

Figure 5.5: 4-stable and 6-stable sets of Case Study 2 and their Normalized Stability Index

5.2.3. CASE 3

In this case perturbations have been introduced. As far as the geometry of the capture set is concerned (Figures 5.6 and 5.7), only minor variations, with respect to the previous case, are present. The same is true for the value of the normalized stability index. In fact, [25] concluded that, while "the CR3BP is not adequate for constructing ballistic capture orbits,the ERTBP is a good approximation of the real model".

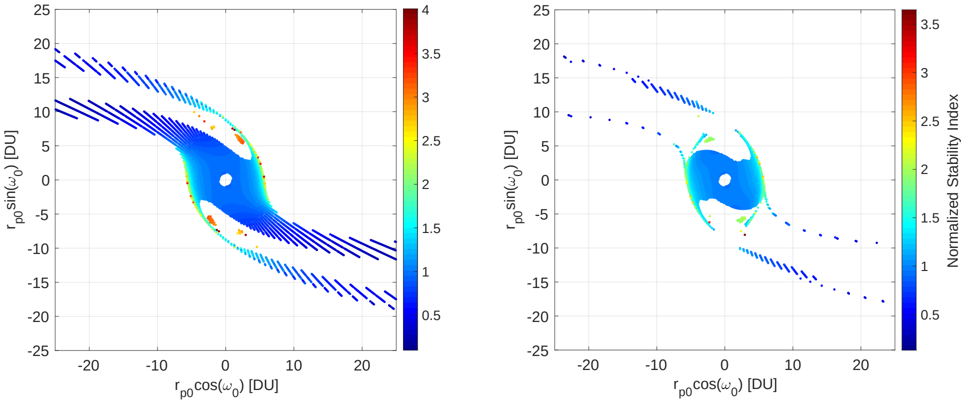

Figure 5.6: 1-stable and 2-stable sets of Case Study 3 and their Normalized Stability Index

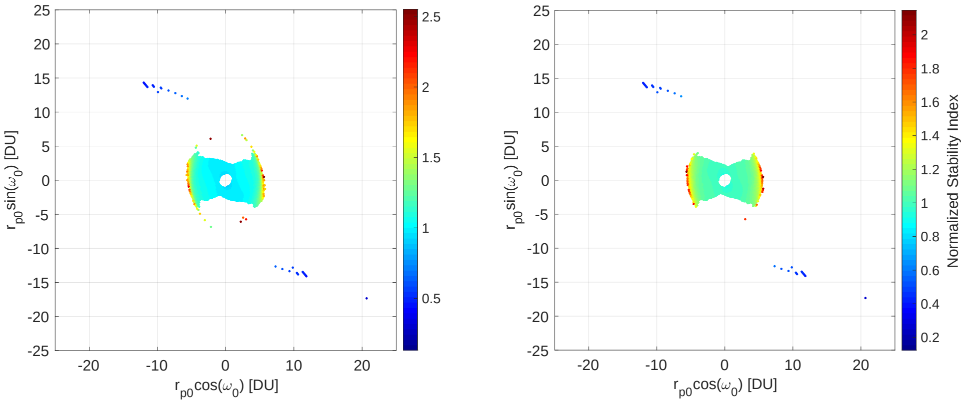

Figure 5.7: 4-stable and 6-stable sets of Case Study 3 and their Normalized Stability Index

The introduction of perturbations increased the computation time to approximately 5 *days*. This is because, every time the acceleration of the spacecraft has to be computed, the relative position of different celestial bodies needs to be retrieved from SPICE: ephemerides retrieval remains the bottleneck of the procedure.

5.2.4. Case 4

The geometry shown in Figure 5.8, 5.9 is fairly different from the previous cases; in fact, the depicted plane is inclined with respect to the one in which the Mars and the Sun lie. The computation required approximately 6 days.

It is interesting to notice that, in this case, the 1-Stable Set is connected, with a few exceptional cases in the bottom-left (and top-right) of the figure, where more than one stable-unstable transition is occurring. It is also relevant to underline that, in this geometry (in which the initial osculating orbital plane it inclined with respect the the one in which the Mars orbit lies) a non-negligible number of initial conditions is associated to a Normalized Stability Index lower than 1: the perturbations acting on the associated trajectories are increasing the spacecraft angular velocity around Mars. This may be a desired feature, from a design point of view.

Finally, it looks like to knowledge of the Normalized Stability Index associated to an n-Stable Set cannot be used to estimate the $(n+1)$-Stable Set.

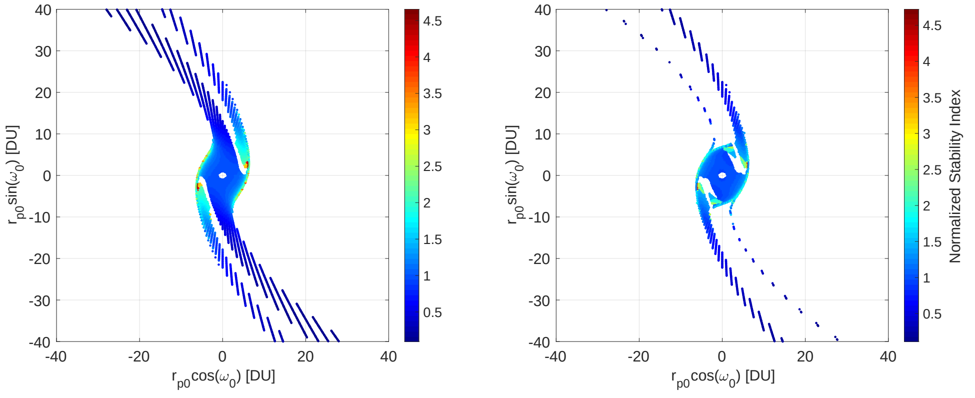

Figure 5.8: 1-stable and 2-stable sets of Case Study 4 and their Normalized Stability Index

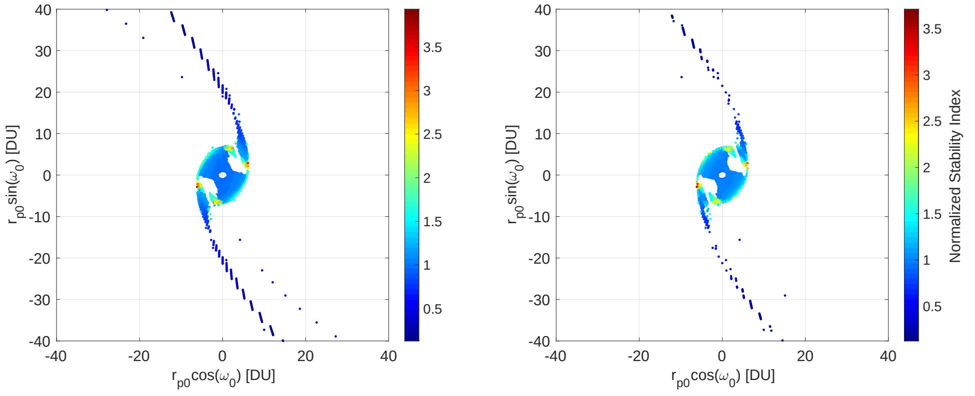

Figure 5.9: 4-stable and 6-stable sets of Case Study 4 and their Normalized Stability Index

5.3. BACKWARD BEHAVIOUR ANALYSIS

As previously discussed, the computation of the Capture Set requires the study of the behaviour of the set of initial conditions *both* forward and backward in time. This section will present the -1-Unstable Sets of the four case studies defined above. No index, analogous to the (Normalized) Stability Index has been used to characterize the set.
Figures 5.10 and 5.11 display the set $\mathcal{X}_1$ associated to the case study problems 1,2,3 and 4, respectively.

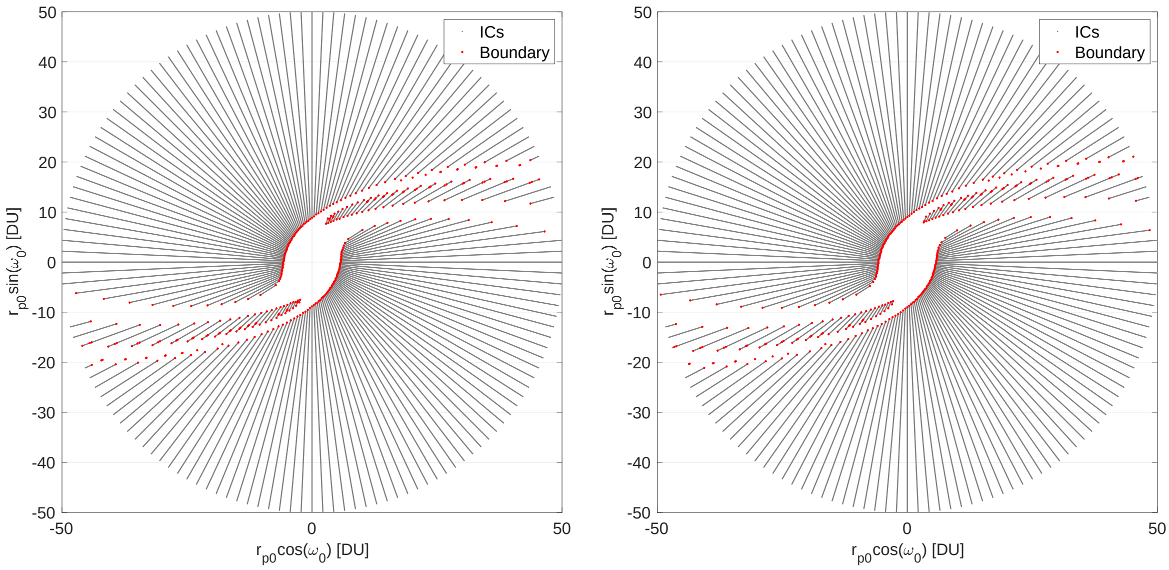

Figure 5.10: -1-unstable set of Case Study 1 & 2.

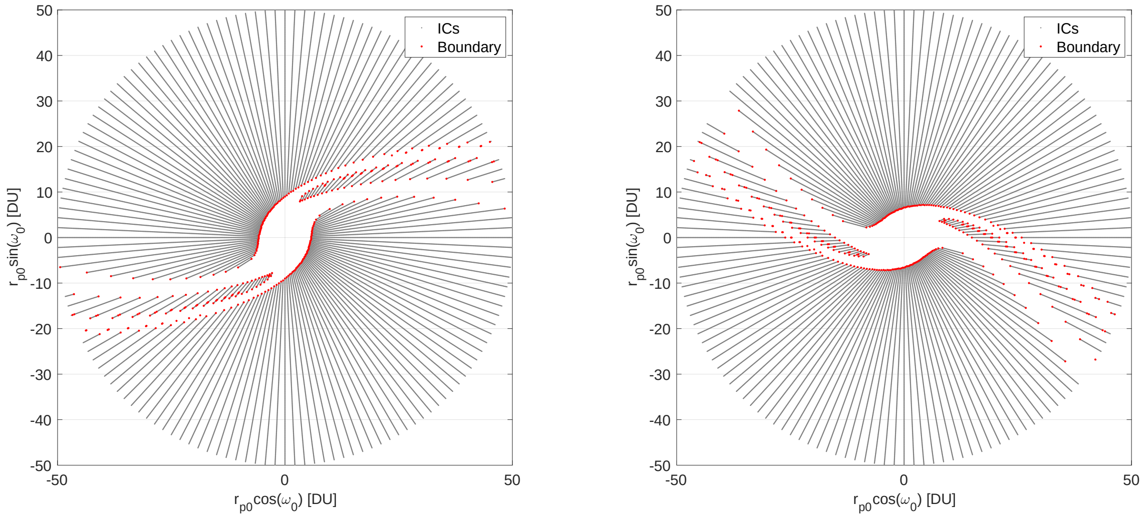

Figure 5.11: -1-unstable set of Case Study 3 & 4.

Following from the considerations given in 5.2.2, one could have speculated that the boundary of the Stable Set characterized by an high value of the Normalized Stability Index, identifies the region of the plane in which a Stable-Unstable transition occurs. Moreover, because of the fact that other parts of the boundary are not displaying such a sudden variation in such index, one could have concluded that such regions identify Stable-Crash or Stable-Acrobatic transitions. From the shapes in Figures 5.10 and 5.11, whose boundaries recall the ones given in the previous section, it not clear whether this is the case or not, since $\mathcal{X}_{-1} \bigcup \mathcal{W}_{-1}$ may approximately cover the entire plane, with a few exception. This consideration will be used, in order to produce a number of results associated to the $\mathcal{X}_{-1}$ (Section 5.4).

The black-and-white representation used here also allows to appreciate the multiple transitions, for a given ω_0; for some values (e.g. $\omega_0 \approx \pi/4$) six transitions can be identified.

From these results, it is finally clear how a sampling, performed in polar coordinates, is not accurate in the estimation of the boundary region associated to large r_{p0}.

5.4. STROBOSCOPIC STRAINLINES

The algorithms and the theories presented in Chapters 3-4 can now be applied for the analysis of the case studies presented above. Different combinations of the number of segments used to compute the Strainline, their number and the tolerance of its integrations have been used to obtain the results given in this section.

5.4.1. CASE 1

For the first case study, the following design choices have been made:

- $\mathcal{W}_1$ in Figure 5.12: 7 segments for each quadrant, each of length 6.0, obtained with absolute and relative integration tolerances of 10^{-1};
- $\mathcal{W}_2$ in Figure 5.12: 10 segments for each quadrant (length 3.0), absolute and relative integration tolerances of 10^{-2};
- $\mathcal{W}_4$ in Figure 5.13: 15 per quadrant (length 1.5), integration tolerances of 10^{-3};
- $\mathcal{W}_6$ in Figure 5.13: 10 per quadrant (length 1.5), integration tolerances of 10^{-4}.

The expression "for each quadrant"implies that, for every problem, four initial conditions are defined: two points, characterized by $\omega_0 = 0$ and $\omega = \pi$ respectively, are used to initialize different Strainlines. Moreover, for both points, two different integrations, clockwise and counter-clockwise, are performed. The number of segments, together with their lengths, identifies the termination condition of the Strainline integration process.

Finally, the combination of integration tolerance and of the length of each Strainline segment has been determined by means of numerical experimentation.

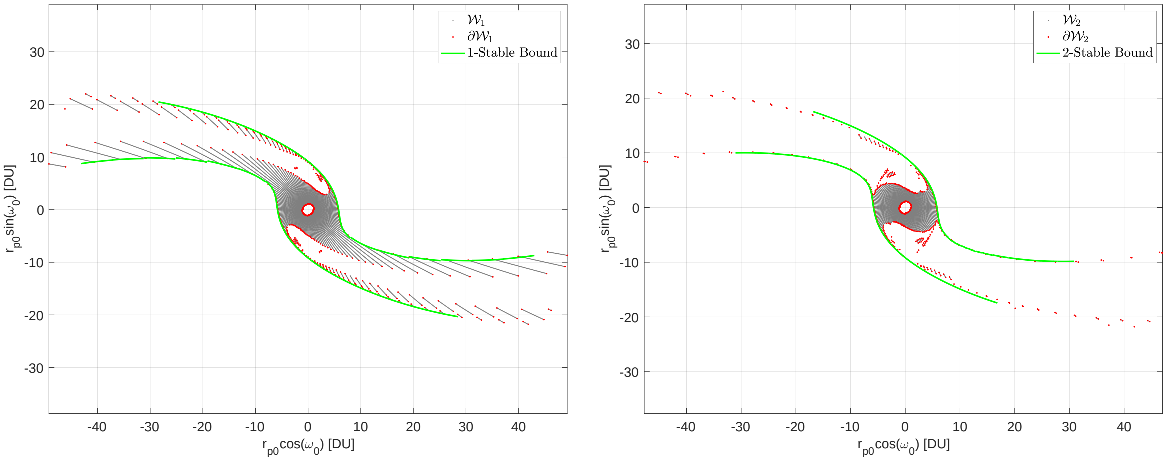

Figure 5.12: 1-stable & 2-stable stroboscopic strainlines with the associated sets.

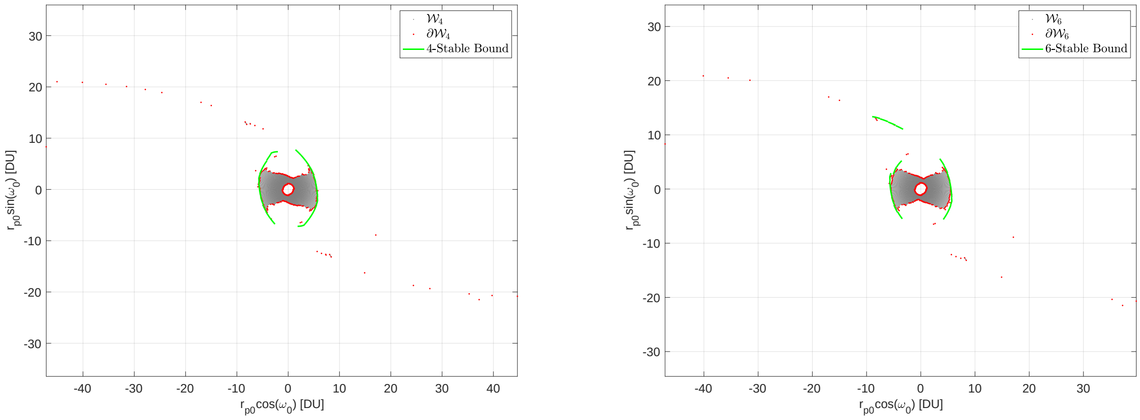

Figure 5.13: 4-stable & 6-stable stroboscopic strainlines with the associated sets.

The fact that, in Figure 5.12, the transitions associated to the re-initialization and bisection process cannot easily be detected, implies that the final point of the previous Strainline is close to the WSB. This positive result allows to increase the length of each segment and, at the same time, work with higher tolerances, allowing to further reduce the computational cost of the process.

From the Figure associated to the 6-stable set, the effect of the generalization discussed in Section 4.7.1 can be appreciated. Once a strainline segments reaches a region in which no stable orbits can be found, the local search is substituted with a wider one: because of this, the big radial discontinuity from approximately [-4,5] to [-9, 14] is obtained. In the Figure associated to the 1-stable set, the branches associated to quadrant 2 and 4 are characterized by minor discontinuities, resulting from the re-initialization in ω.

Strainlines can also be superimposed onto dynamical systems propagating the state of the spacecraft backward in time. In this way, it is possible to identify the boundary of the set $\mathcal{X}_{-1}$. Following the hypothesis given at the end of Section 5.3, the set of conditions in $\mathcal{K}_n \bigcup \mathcal{D}_n$ is negligible, compared to $\mathcal{X}_n \bigcup \mathcal{W}_n$. This implies that the boundary region of the two almost complementary sets is approximately the same: the same algorithms can therefore be used to identify the unstable set.

It is again important for the the bisection method to converge to a point associated to a stable orbit: this allows to identify the final integration time at which to compute the CG strain tensor. Therefore, the implementation allows to estimate the boundary of $\mathcal{X}_{-1}$ "from the outside".

Figure 5.14 shows the results approximating $\mathcal{X}_{-1}$, obtained by integrating 7 strainline segments for each quadrant, for a length of 6.0 and absolute and relative integration tolerances of 10^{-1}.

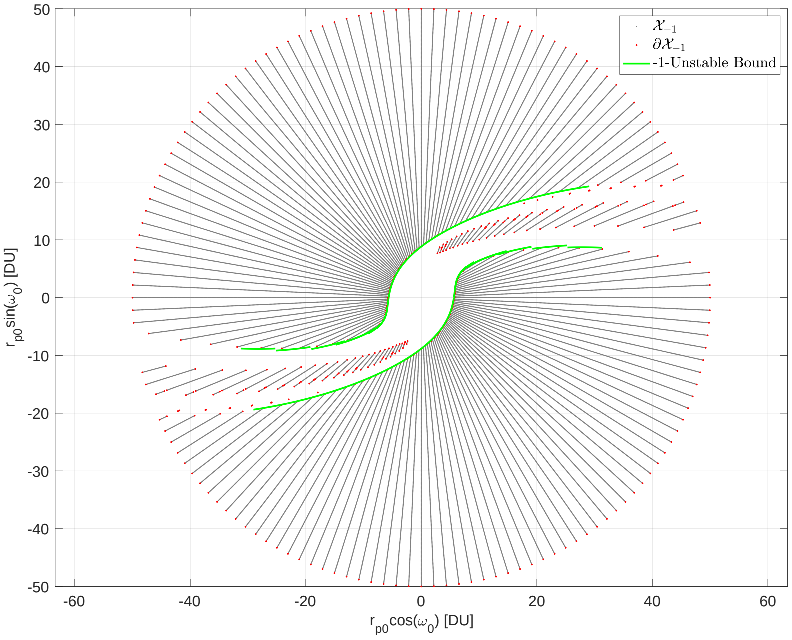

Figure 5.14: -1-unstable stroboscopic strainline with the associated set

The discontinuities associated to the quadrant-1 branch are the more evident ones: since both bisections have been used for its computation, there's a correlation between the Strainline being close-to-radial and its divergence from the boundary region.

Moreover, the good matching between the boundary of $\mathcal{X}_{-1}$ and the strainlines supports the previously stated hypothesis.

STROBOSCOPIC STRAINLINES AND INVARIANT MANIFOLDS

An additional propagation, whose results are shown in Figure **??**, has been performed using 110 segments per quadrant, each of length 6.0; because of lack of convergence, however, the propagation of the branches associated to quadrant 2 and 4 was prematurely terminated. The absolute and relative tolerance of the streamline integrator have been again set to 10^{-1}. The computation required approximately 57 hours, and it has been performed to investigate the relation between the final radial distance and the computation time. In fact, the (potential) computational advantage of this approach can be appreciated for big values of r_p where, in order to get a good coverage, the grid would require a big number of points (ideally proportional to the square of the maximum radius considered).

Depending on the desire size of the post-capture orbit around the target body, the use of Stroboscopic Strainlines leads to a computational advantage, even with the "primitive" implementation used for this work.
Moreover, this propagation has been performed to investigate the potential similarities between Invariant Manifolds and Stroboscopic Strainlines, and to understand their potential as a generalizing tool for non-autonomous systems. In particular, the resulting geometry recalls [35], and particularly Figure 5.15b. While it should be underlined that [35] worked with a CR3BP model (in order to simulate the Earth–Moon system), where the theory of invariant manifolds applies, and investigated the elements of the 2-stable set with a fixed Jacobi constant, also the points defining the strainlines in Figure **??** are associated to stable orbits. This consideration appears to justify a further investigation into Stroboscopic Strainlines, in order to understand their relations with Lagrangian Coherent Structures.

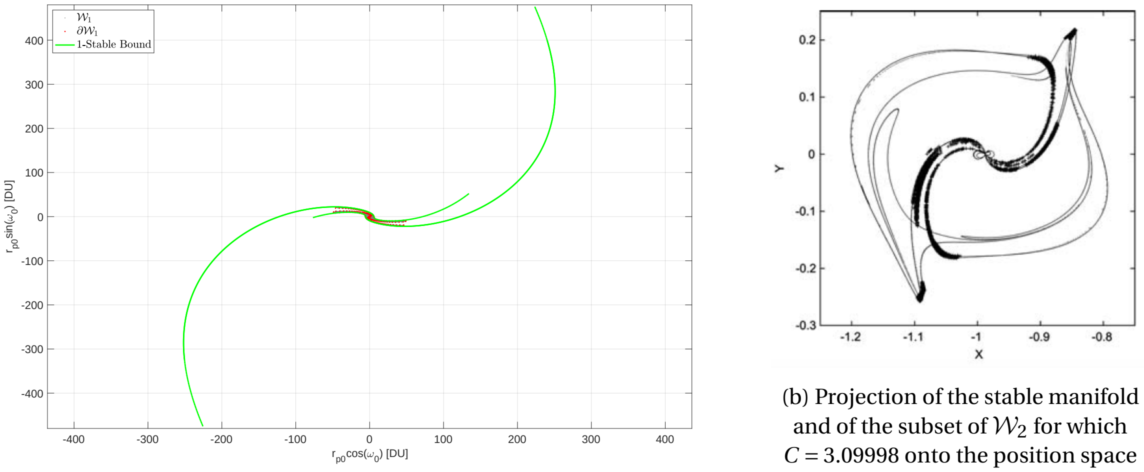

(a) 1-stable stroboscopic strainlines; longer branches.

(b) Projection of the stable manifold and of the subset of $\mathcal{W}_2$ for which $C = 3.09998$ onto the position space [35].

Figure 5.15: Comparison of Stroboscopic Strainlines and Invariant Manifolds.

5.4.2. CASE 2

For case study 2, slightly different design choices, with respect to Case 1, have been made. This has been done, in order to test the requirements of the proposed technique. As a general rule, as in the previous case, lower tolerances have been associated to higher numbers of revolutions, defining the stable set of interest: the WSB of a given $\mathcal{W}_n$ is expected to be "less well-behaving", the higher the value of n.

- $\mathcal{W}_1$ in Figure 5.16: 10 segments for each quadrant, each of length 6.0, obtained with absolute and relative integration tolerances of 10^{-1};
- $\mathcal{W}_2$ in Figure 5.16: 10 segments for each quadrant (length 3.0), absolute and relative integration tolerances of 10^{-2};
- $\mathcal{W}_4$ in Figure 5.17: 15 per quadrant (length 1.5), integration tolerances of 10^{-4};
- $\mathcal{W}_6$ in Figure 5.17: 10 per quadrant (length 1.5), integration tolerances of 10^{-5};
- $\mathcal{X}_{-1}$ in Figure 5.18: 15 per quadrant (length 4.0), integration tolerances of 10^{-1}.

As in the previous case, there's no matching between the computed Strainlines and the regions of $\partial\mathcal{W}_4$ and $\partial\mathcal{W}_4$ associated to a low value of the Normalized Stability Index. It is not clear why, but these two facts may be produced by a common cause.

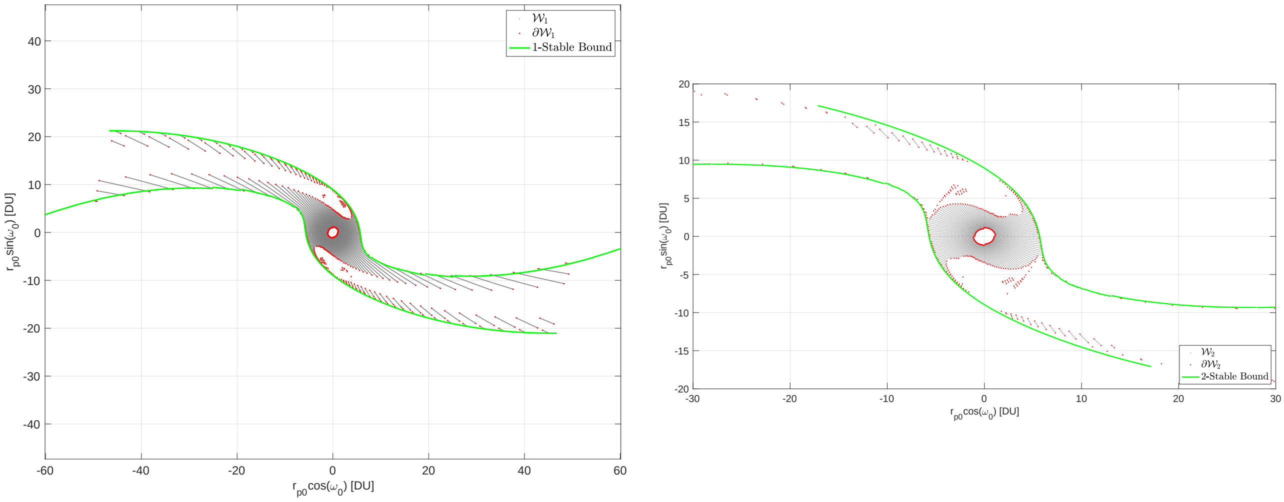

Figure 5.16: 1-stable & 2-stable stroboscopic strainlines with the associated sets.

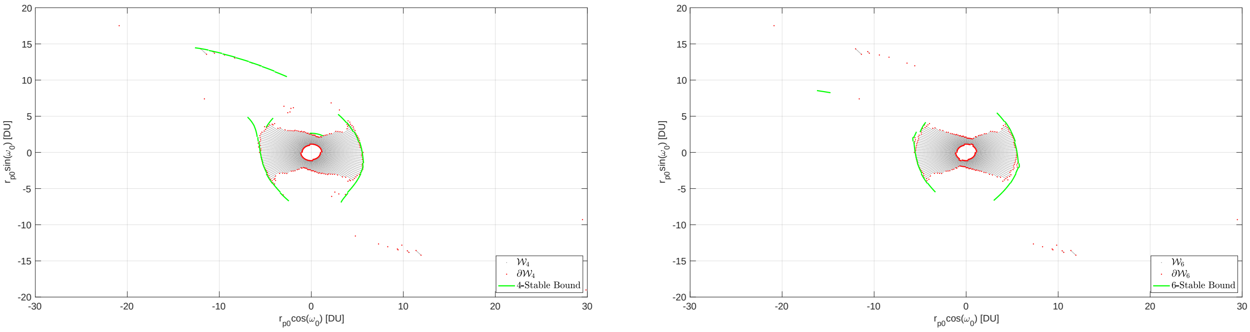

Figure 5.17: 4-stable & 6-stable stroboscopic strainlines with the associated sets.

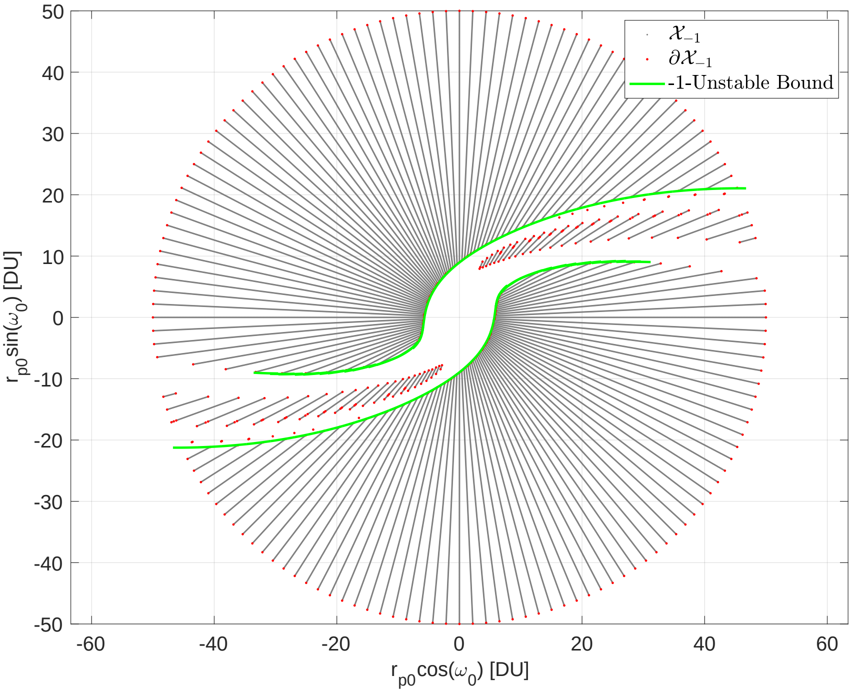

Figure 5.18: -1-unstable stroboscopic strainline with the associated set

As previously noticed, for some radial directions, more than one transition occurs. In principle, the Strainline should be able to approximate the boundary of the two "internal" regions of Figure 5.18 as well, once the new initial points are identified.

5.4.3. CASE 3

For the last two cases, in which perturbations have been included, similar design choices have been made for the computation of the strainlines. This is because the strainlines, being informed by the flow, reside in a more abstract domain and are not directly influenced by the formulation of the equations of motion: in fact, the accuracy requirements associated to their computation is merely a function of the WSB shape, not of the dynamical system complexity, which is treated as a "black box" by the superimposed approach (this can also be understood, recalling the nested structure of the two integration processes).

- $\mathcal{W}_1$ in Figure 5.19: 10 segments for each quadrant, each of length 6.0, obtained with absolute and relative integration tolerances of 10^{-1};

- $\mathcal{W}_2$ in Figure 5.19: 10 segments for each quadrant (length 3.0), absolute and relative integration tolerances of 10^{-2};

- $\mathcal{W}_4$ in Figure 5.20: 15 per quadrant (length 1.0), integration tolerances of 10^{-3};

- $\mathcal{W}_6$ in Figure 5.20: 10 per quadrant (length 1.0), integration tolerances of 10^{-4};

- $\mathcal{X}_{-1}$ in Figure 5.21: 15 per quadrant (length 4.0), integration tolerances of 10^{-1}.

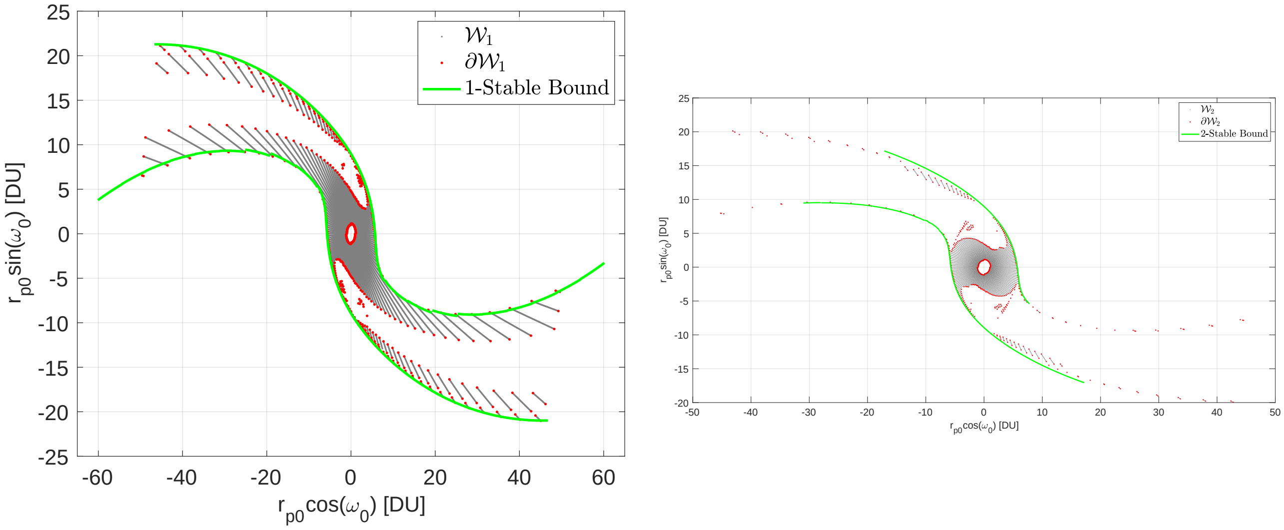

Figure 5.19: 1-stable & 2-stable stroboscopic strainlines with the associated sets.

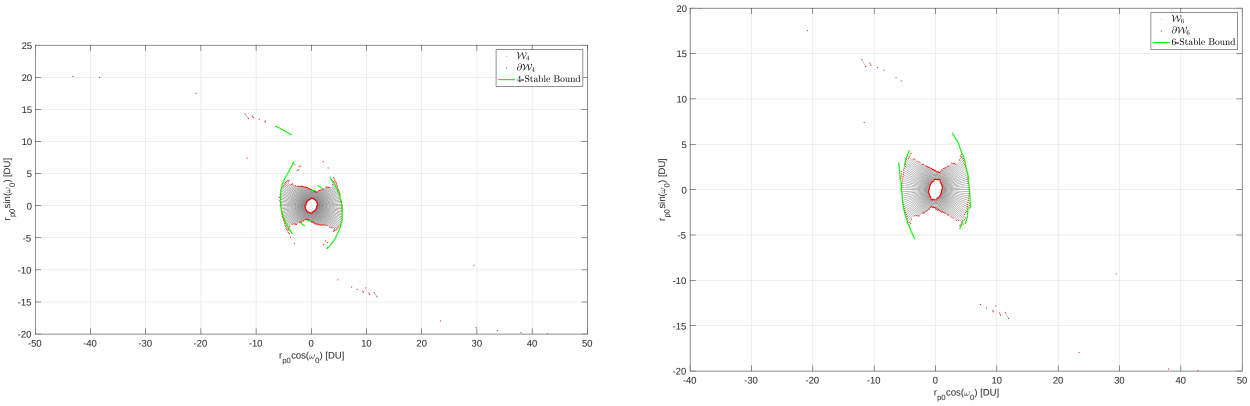

Figure 5.20: 4-stable & 6-stable stroboscopic strainlines with the associated sets.

The computation of the bottom-right branch of the Strainline associated to $\partial\mathcal{W}_2$ has been manually terminated. In confronting the second figure with the third one, it is interesting to notice how the strainline associated to $\partial\mathcal{W}_4$ appears to follow the inner boundary of $\mathcal{W}_2$. Again, for an high number of revolutions, some regions of the WSB couldn't be identified.

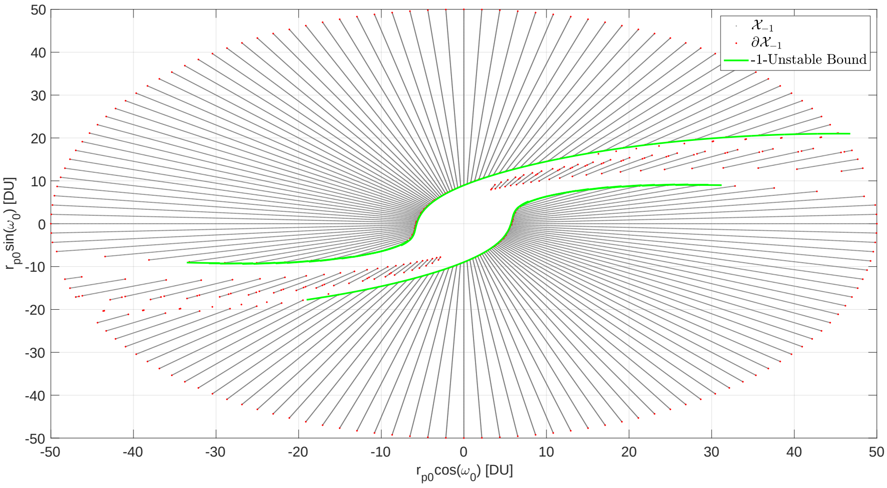

Figure 5.21: -1-unstable stroboscopic strainline with the associated set

As a general consideration, the level of accuracies of these results is comparable to the one of of the previous cases; this fact confirms the fact assumption presented at the beginning of the Section, according to which the strainlines accuracy requirements are not a function of the underlying dynamical complexity.

5.4.4. CASE 4

Finally, the computations associated to Case 4, are characterized by:

- $\mathcal{W}_1$ in Figure 5.22: 10 segments for each quadrant, each of length 6.0, obtained with absolute and relative integration tolerances of 10^{-1};
- $\mathcal{W}_2$ in Figure 5.22: 12 segments for each quadrant (length 3.0), absolute and relative integration tolerances of 10^{-1};
- $\mathcal{W}_4$ in Figure 5.23: 15 per quadrant (length 2.0), integration tolerances of 10^{-1};
- $\mathcal{W}_6$ in Figure 5.23: 20 per quadrant (length 1.5), integration tolerances of 10^{-1};
- $\mathcal{X}_{-1}$ in Figure 5.24: 7 per quadrant (length 6.0), integration tolerances of 10^{-1}.

The choice of higher tolerances and longer strainline segments, with respect to the previous Section, has mainly been driven by the need to reduce the computational cost of the simulations.

The results given in Figure 5.22 are of particular interest, in order to underline the positive effect of dividing the propagation into multiple branches. Dealing with $\mathcal{W}_1$, the Strainline at the top identifies a stable-unstable transition that, for high values of r_p is not the "main" one: its re-initialization allows to move back to the relevant transition, containing the majority of the stable conditions, and hence better approximating the associated Stable set. Again, the computation of the strainline associated to $\partial\mathcal{W}_2$ has been manually terminated.

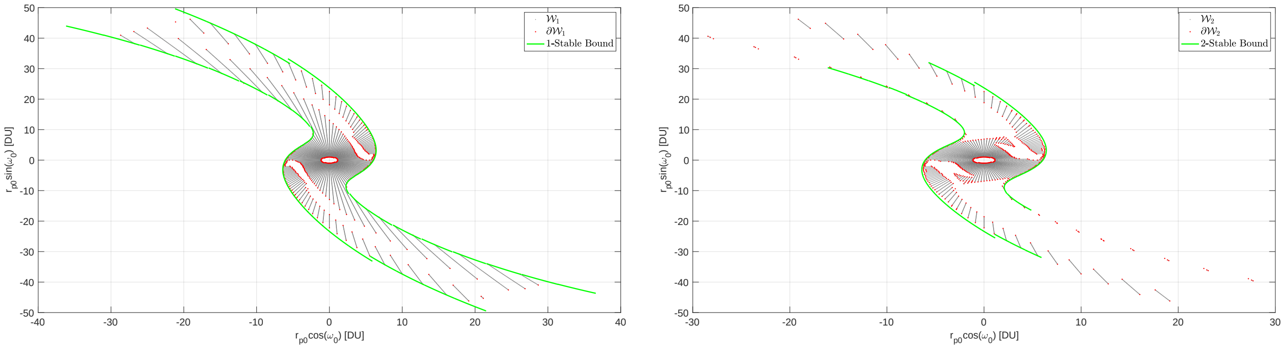

Figure 5.22: 1-stable & 2-stable stroboscopic strainlines with the associated sets.

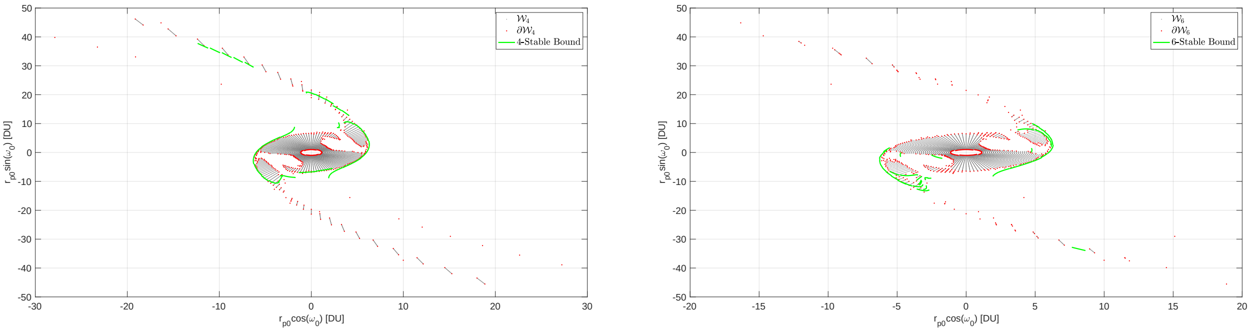

Figure 5.23: 4-stable & 6-stable stroboscopic strainlines with the associated sets.

An additional, general consideration can be made, recalling again [35]. In the mentioned work, the stable set has been computed for a fixed value of the Jacobi constant C, together with the invariant manifolds associated to the Lyapunov orbits around L_1, L_2 (Figure 5.15b). Such procedure lead to the following conclusion:

$$\partial\mathcal{W}_n(C) \subset \overline{S} \tag{5.2}$$

where $\overline{S}$ is the clausure of the union of the two branches of the stable manifold. In this work, a similar relation appears to hold, i.e. the set of stable orbits is a subset of the space defined by the associated Stroboscopic strainlines.
As predictable, because of the higher value of the strainline integration tolerance, the results associated to a high number of revolutions around the Mars, are less accurate than the ones of the previous Cases.

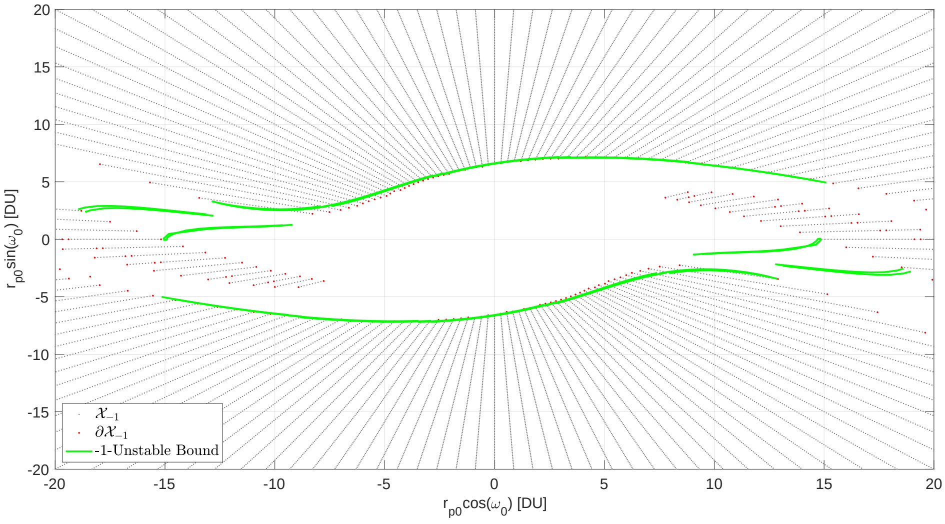

Figure 5.24: -1-unstable stroboscopic strainline with the associated set

Dealing with the results shown in Figure 5.24, while the majority of the output approximates the boundary of the set of unstable conditions, unexpected branches can be seen on both sides of the figure. These results should be further investigated, to understand whether they are simply an error, resulting from a too specific implementation and/or wrong tolerances, or whether the given results describe some additional features of the problem, not directly associated to, in this specific case, $\mathcal{X}_{-1}$.

5.5. CAPTURE SETS & STROBOSCOPIC STRAINLINES

The fact that a Capture Set is defined as the intersection of two other sets, $\mathcal{W}_n$ and $\mathcal{X}_1$, can easily be translated, using the strainline approach, by considering the intersection of the spaces that each strainline defines: of course, in the case of strainlines identifying the stable set, the space of interest is the one close to the target body, while, in the case related to the unstable set, the space of interest is "outside" the associated strainline.

5.5.1. CASE 1

Figures 5.25 and 5.26 show the intersection of the previously computed Stroboscopic Strainlines and the different Capture Sets. It is interesting to notice how the majority of the initial conditions, leading to capture, are located close to the intersection between the stable and unstable Strainline; this is particularly relevant for a high number of revolutions around the target.

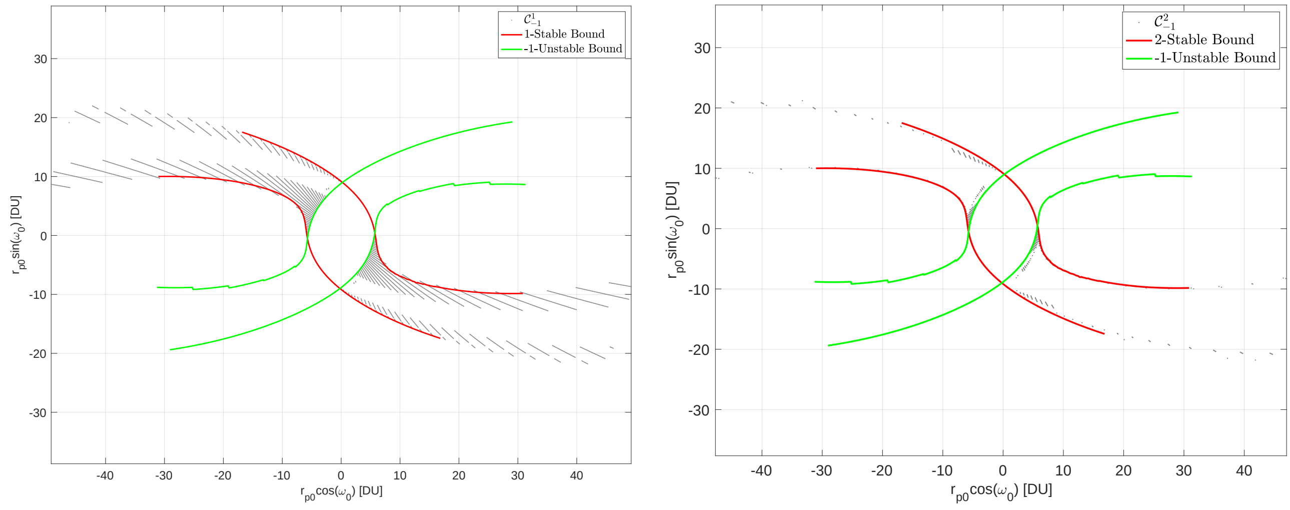

Figure 5.25: 1- & 2-Capture Set and the associated stroboscopic strainlines

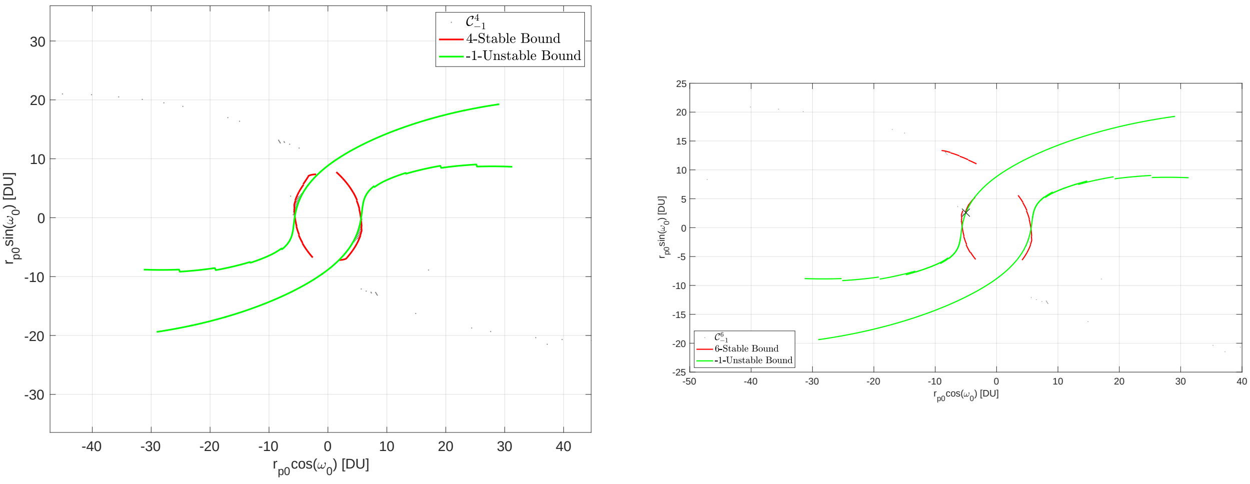

Figure 5.26: 4- & 6-Capture Set and the associated stroboscopic strainlines

In the left figure of 5.26, the x identifies the initial condition of the 6-Capture Set associated to the minimum Stability

Index:

$$S_{min} = 9538.4 \quad TU$$

The initial state is identified by:

$$r_{p0} = 5.63350 \quad DU, \qquad \omega_0 = 152.5^\circ$$

and it is therefore characterized by the following Normalized Stability Index, identifying a close-to-Keplerian orbit:

$$\overline{S} = 1.2694$$

5.5.2. CASE 2

Figures 5.27 and 5.28 show the same results, for the second case study. The results shown are qualitatively the same as the ones given in Section 5.5.1.

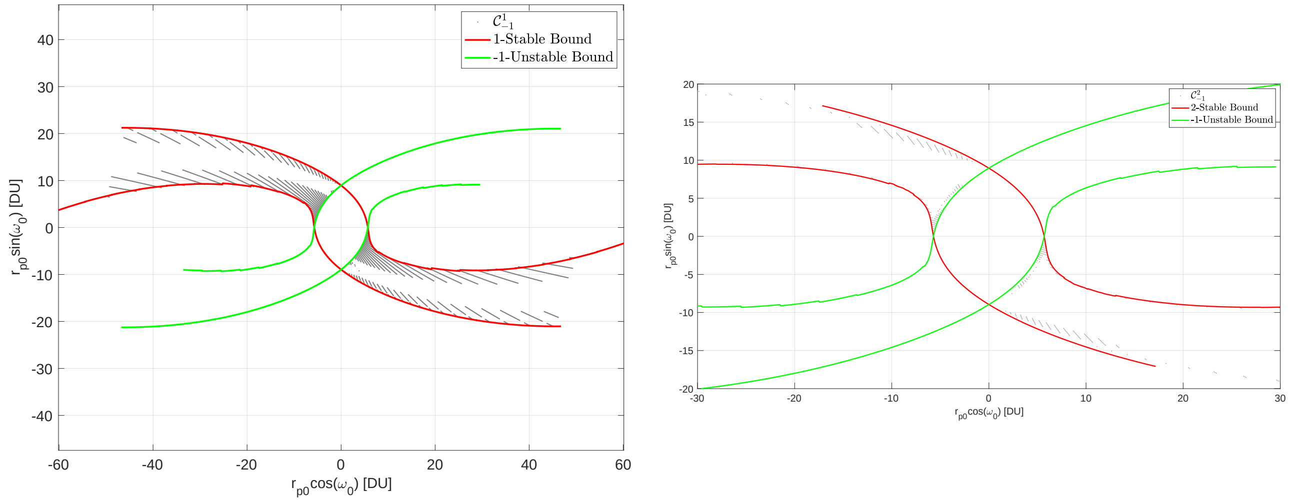

Figure 5.27: 1- & 2-Capture Set and the associated stroboscopic strainlines

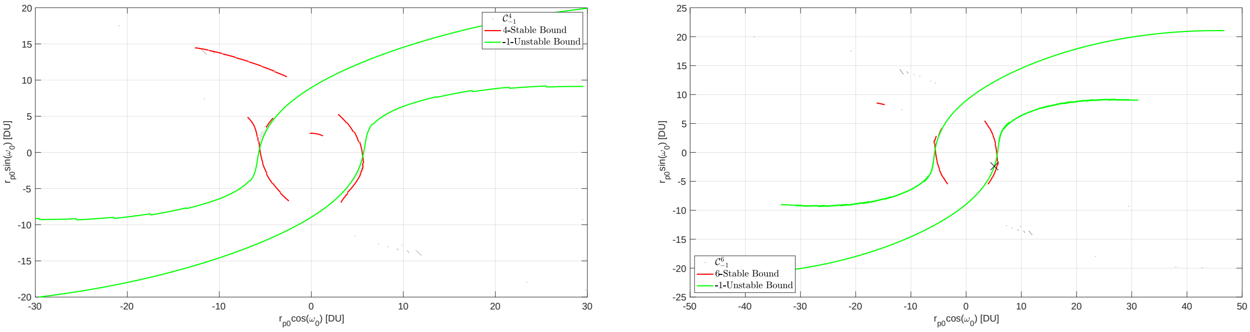

Figure 5.28: 4- & 6-Capture Set and the associated stroboscopic strainlines

The x point is now associated to the following values:

$$S_{min} = 10451.7 \quad TU$$

$$r_{p0} = 5.63350 \quad DU, \qquad \omega_0 = 335^\circ$$

$$\overline{S} = 1.3909$$

From the given results, its clear that stroboscopic strainlines associated to $\partial\mathcal{X}_{-1}$ are relevant, in the identification of the Capture Set, only for a small portion of the plane.

5.5.3. CASE 3

From Figures 5.29 and 5.30 it can be seen that the majority of Capture conditions are located close to the -1-Unstable bound; this is particularly true for more than one revolution around the target body.

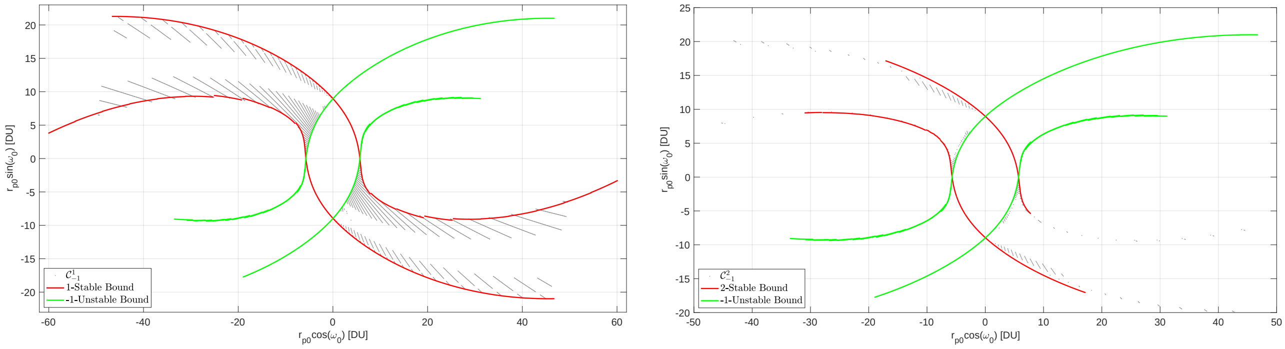

Figure 5.29: 1- & 2-Capture Set and the associated stroboscopic strainlines

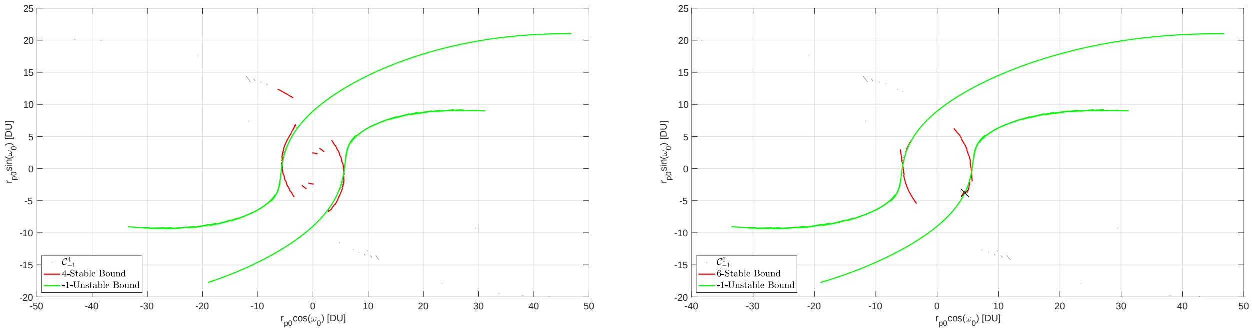

Figure 5.30: 4- & 6-Capture Set and the associated stroboscopic strainlines

Again, the x point is associated to the following values:

$$S_{min} = 10362.3 \quad TU$$

$$r_{p0} = 5.91430 \quad DU, \qquad \omega_0 = 320^\circ$$

$$\overline{S} = 1.2820$$

The condition associated to the minimum stability index is again located in the proximity of the strainline associated to $\partial\mathcal{X}_{-1}$. Building on previous considerations, an effective routine for ballistic capture trajectory design would be:

1. compute short branches of the strainlines associated to an n-Stable Set of interest;
2. compute the branches of the strainlines associated to $\partial\mathcal{X}_{-1}$ *inside* the stable region identified by the previous results;
3. perform a small but dense sampling of the resulting space, in the vicinity of the unstable strainline.

5.5.4. CASE 4

Figures 5.31 and 5.32 confirm what's been stated in the previous section. It appears that a big number of capture conditions can easily be found, investigating the region in the proximity of the -1-Unstable bound, located inside the stable region identified by the n-Stable Strainlines.

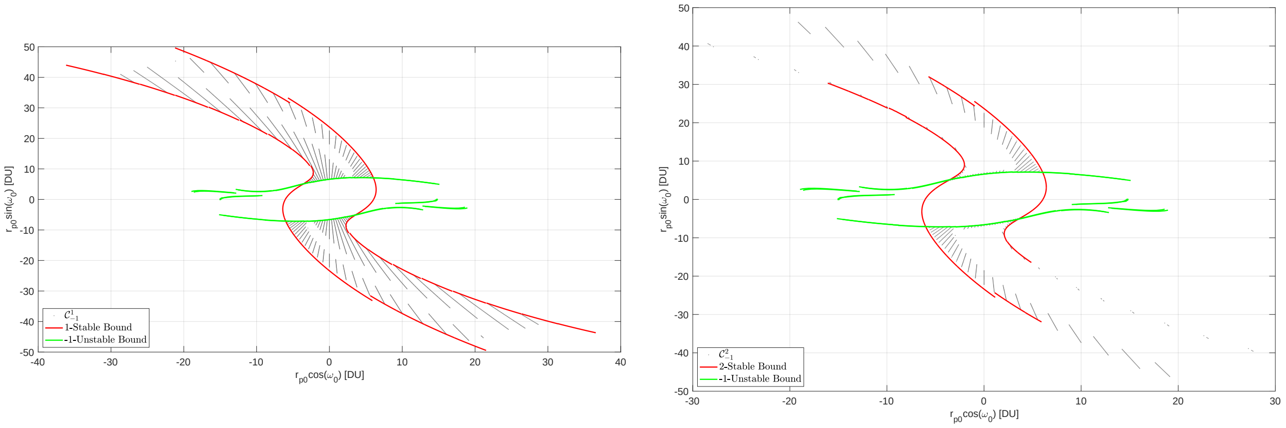

Figure 5.31: 1- & 2-Capture Set and the associated stroboscopic strainlines

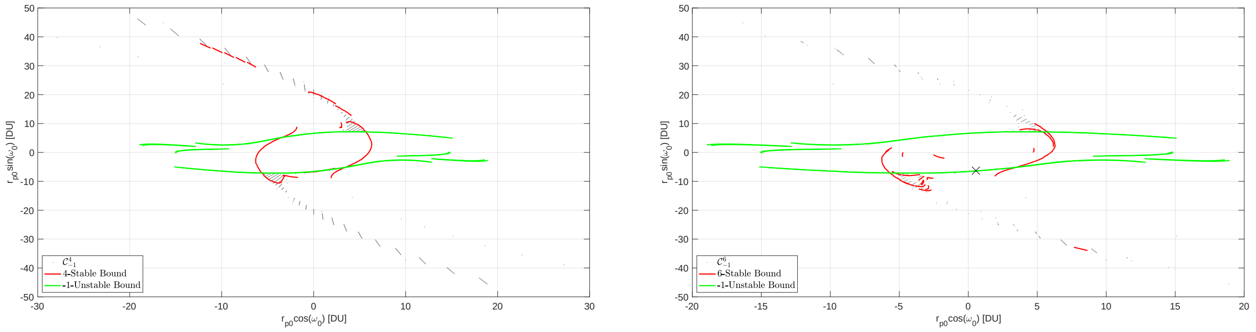

Figure 5.32: 4- & 6-Capture Set and the associated stroboscopic strainlines

Finally, the x point is associated to the following values:

$$S_{min} = 11004.4 \quad TU$$

$$r_{p0} = 6.33550 \quad DU, \qquad \omega_0 = 275^\circ$$

$$\overline{S} = 1.2279$$

5.6. TRAJECTORIES

This section presents the geometries of the trajectories associated to the Capture Sets given above. The initial conditions used to obtain them are the ones given in the previous section and identified by the lowest Normalized Stability Index (Section 3.3.2) in $\mathcal{C}^6_{-1}$. The initial conditions are propagated both forward and backward in time, and their stable and unstable branches can be easily identified.
While Figures 5.33 and 5.34, showing the trajectories of Case study 1,2,3,4, are associated to an inertial reference frame, the results given in Figures 5.35 and 5.36 represent the same trajectories in a roto-pulsating reference frame, as introduced in Section 2.4.

The initial states associated to the four orbits, expressed in the inertial reference frame, are (in normalized units):

$$\mathbf{x}_1 = \begin{bmatrix} -4.88346 \\ 2.50060 \\ 1.27873 \\ -0.29296 \\ -0.46671 \\ -0.20616 \end{bmatrix}, \qquad \mathbf{x}_2 = \begin{bmatrix} 3.69276 \\ -3.82839 \\ -1.85563 \\ 0.44407 \\ 0.35519 \\ 0.15093 \end{bmatrix};$$

$$\mathbf{x}_3 = \begin{bmatrix} 2.58933 \\ -4.80638 \\ -2.27444 \\ 0.51606 \\ 0.23385 \\ 0.09333 \end{bmatrix}, \quad \mathbf{x}_4 = \begin{bmatrix} 2.36010 \\ -2.98829 \\ -5.06347 \\ 0.50178 \\ 0.20939 \\ 0.11031 \end{bmatrix};$$

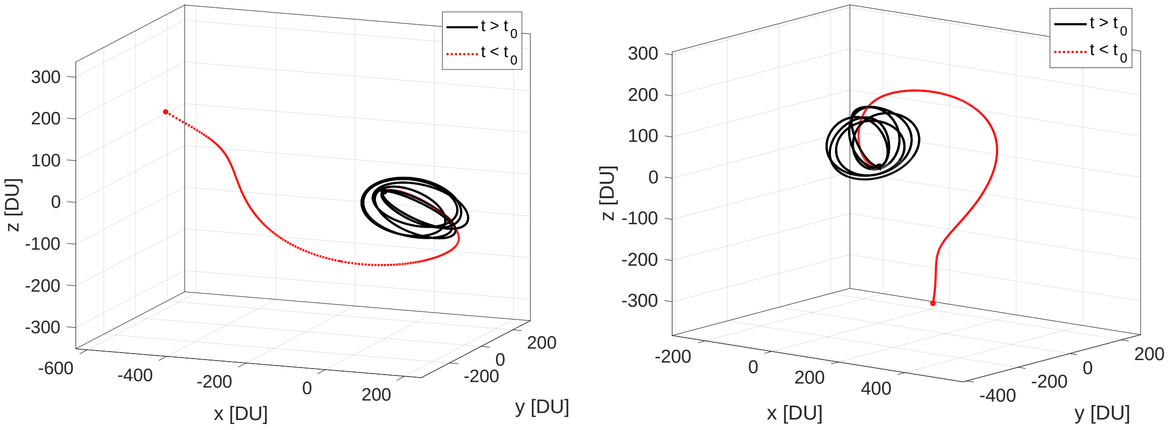

Figure 5.33: Orbits, associated to the minimum Normalized Stability Index of $\mathcal{C}^6_{-1}$ for Case 1 & 2, in an inertial reference frame.

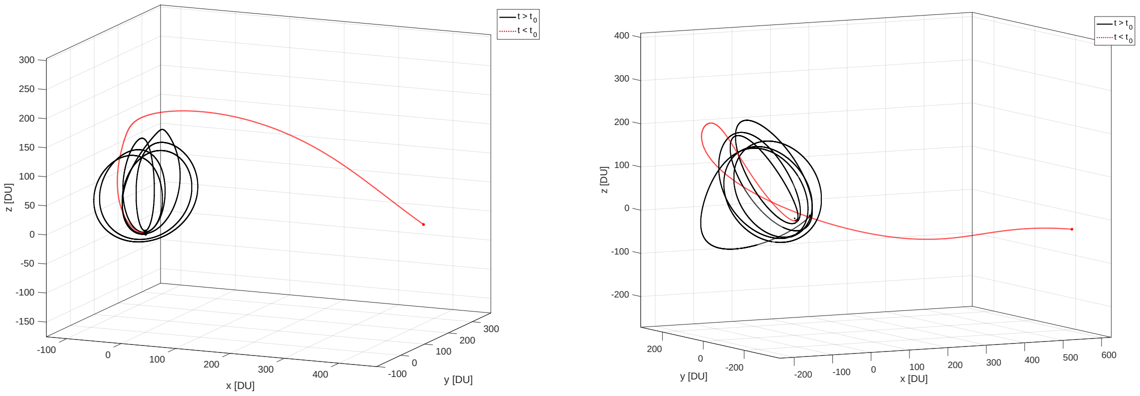

Figure 5.34: Orbits, associated to the minimum Normalized Stability Index of $\mathcal{C}^6_{-1}$ for Case 3 & 4, in an inertial reference frame.

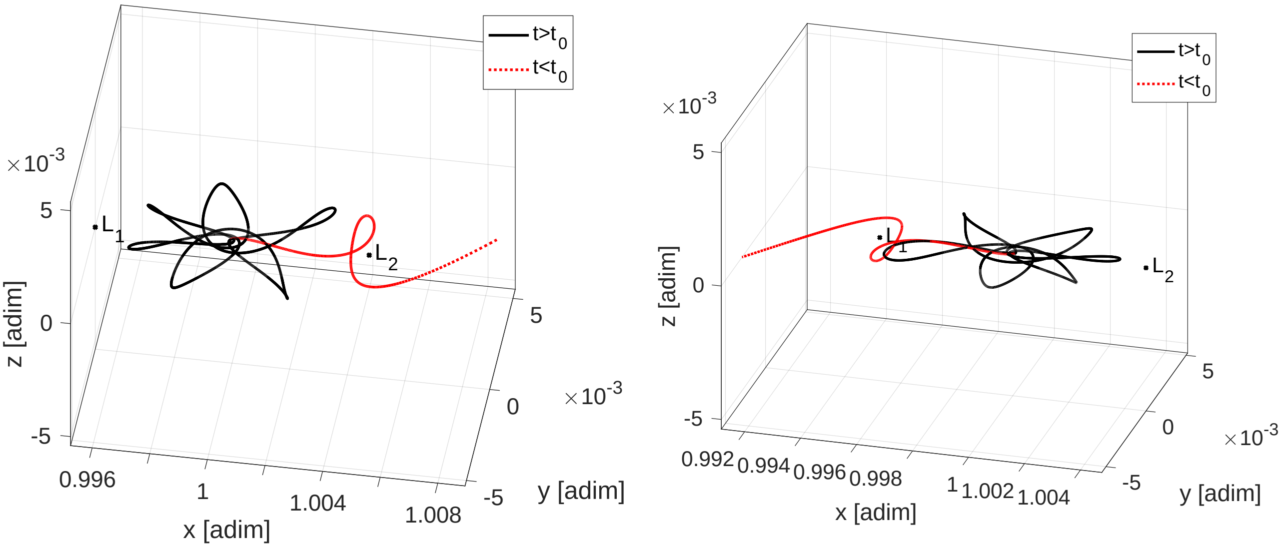

Figure 5.35: Orbits, associated to the minimum Normalized Stability Index of $\mathcal{C}^{6}_{-1}$ for Case 1 & 2, in a Roto-pulsating reference frame.

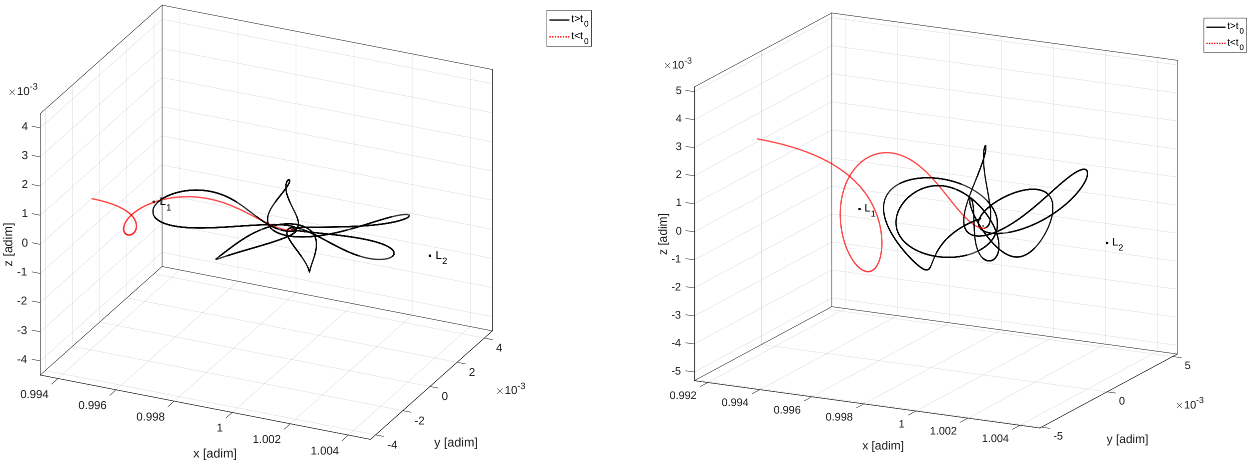

Figure 5.36: Orbits, associated to the minimum Normalized Stability Index of $\mathcal{C}^{6}_{-1}$ for Case 3 & 4, in a Roto-pulsating reference frame

5.7. REPRESENTATION IN DIFFERENT SPACES

As discussed in Section 4.6.1, in order to be able to investigate results from previous works, like the ones given in Figures 3.11, 3.12, alternative mappings can be introduced, without a substantial variation of the technique, in order to investigate structures present in different 2D subsets of the phase space.
A preliminary result of this approach is shown in Figure 5.37, where a Stroboscopic Strainline is plotted over $[0,\pi]\times[0,2\pi]$, the space in which a grid search has been performed, studying the stability of the orbits as a function of the inclination and Right Ascension of the Ascending Node associated to the initial osculating orbit. For this specific simulation, the following values, expressed with respect to a Body Mean Equator reference frame, have been used:

$$e = 0.99; \quad \omega = 0.0 \ rad; \quad r_p = 1.2 \quad f = 0 \ rad$$

The initial simulation epoch is the 8^{th} May 2024, 12 : 36 : 08.64 (UTC).
In order to perform the same routine, the bisection algorithm has been further generalized, in order to take i and Ω as input variables. The result of the strainline integration are given in Figure 5.37:

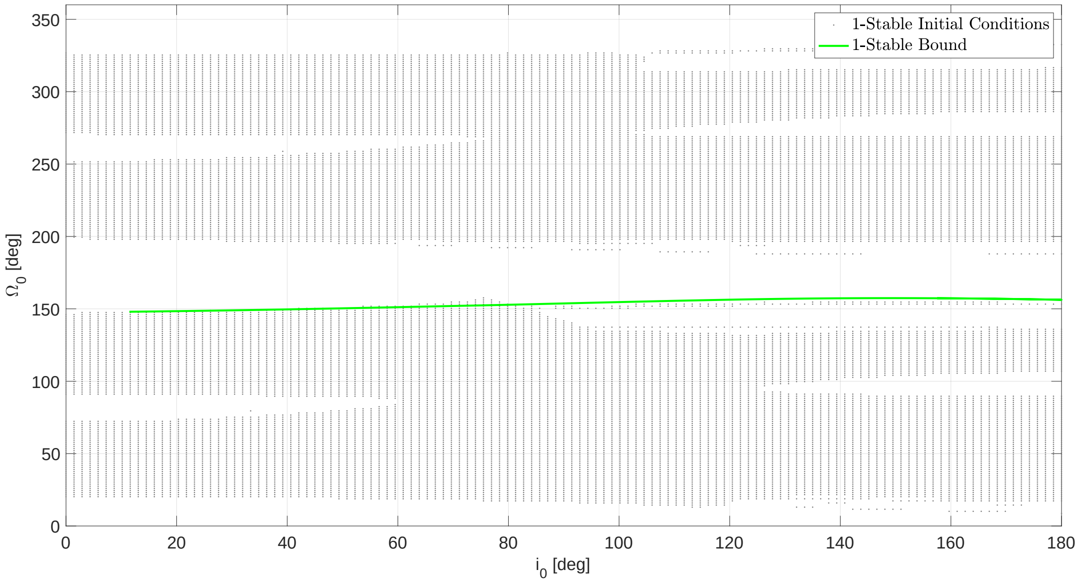

Figure 5.37: Set of 1-stable initial conditions and associated stroboscopic strainline in the (i, Ω) space.

The possibility of applying the proposed technique to difference 2D spaces is useful, from a mission design point of view. Because of the uncertainties characterizing the dynamics (e.g., associated to the initial state of the spacecraft) in the trajectory design process, it is important to select a robust solution. Based on the dynamical quantity characterized by the main uncertainty (e.g. the target-relative initial energy of the spacecraft, its speed ...), this approach allows to use it as one of the two variables associated to the 2D strainline computation. In this way, since the strainline would identify the boundary of the capture set as a function of the variable characterized by epistemic uncertainty, the results could be used to select a conservative nominal value, for such variable.

5.8. FINAL CONSIDERATIONS

In this Chapter, a number of results have been presented. These allowed to show the robustness of the proposed technique with respect to:

- the model fidelity describing the underlying dynamical model;
- the number of revolution associated to the forward-in-time Stable Set;
- the direction of the integration (forward and backward in time);
- the 2D subset of the phase space.

The results also triggered some ideas, that could in the future be used to build a more efficient toolbox for the computation of ballistic capture orbits.

6

CONCLUSIONS AND RECOMMENDATIONS

6.1. CONCLUSIONS

As discussed in Section 1.3, this work aims at tackling the following research question:

Is it possible to characterize the ballistic capture mechanism, based on the initial osculating orbital parameters of the target-relative geometry, making use of the theory of Lagrangian Coherent Structures?

The results presented in Chapter 5 allow to reply positively, since the theory of Lagrangian Coherent Structures informed a new technique, applicable in the trajectory design process of ballistic capture orbits. It has been shown how the study of tools and heuristics associated to such theory can help characterizing the mechanics of ballistic capture; with the introduction of *Stroboscopic Strainlines*, an approximation of the Weak Stability Boundaries of given problems have been computed. This has been done mainly in the domain in which the Capture Set is defined, but the flexibility of the technique allows to introduce alternative subsets of the phase space, whose investigation could lead to a clearer understanding of the ballistic capture phenomenon and of its features.

The presented results show how the effectiveness of the technique is independent of the fidelity of the underlying dynamical model, onto which the flow-informed strategy is superimposed: its applicability covers complex, non-periodic (and, in general, time-dependent) dynamical systems in astrodynamics. Particularly for highly complex models, e.g. taking into account n-body perturbations, solar radiation pressure and non-spherical gravity, the technique has the potential of greatly reducing the cost of the Capture Set computation, and hence to increase the applicability of Ballistic Capture in trajectory design.

This research project aims at contributing in opening up the field of low-energy transfers in space mission design, allowing for new concepts to redefine the domain of feasible missions for human space exploration.

6.2. RECOMMENDATIONS

While, when relevant, the assumptions and the design choices made have been underlined throughout the work, and while many recommendations have been given in commenting the results in the previous chapter, they will be summarized here. Moreover, some high-level considerations, which have not been included in the core of this document for readability, will be given here.

Based on this work, future research efforts are required:

- the proposed technique appears to potentially reduce the cost associated to the computation of a Capture Set of interest. Quantifying the optimal trade-off between the accuracy of the WSB estimation and its efficiency, as a function of different design parameters, may be relevant: for example, an informed selection of the best strainline integrator is missing from this work; it is conceivable for the strainline to require much less accurate integration routine, e.g. fixed step size RK schemes, whose implementation may allow the reduction of the tolerances associated to the integration of the equations of motion and hence a more accurate estimation of the State Transition Matrix;
- the applicability of the proposed technique to different 2D subsets of the phase space should be exploited, in order to understand some features of the capture phenomenon, given in previous works (e.g. [35] - Figure 4). This could also increase the applicability of ballistic capture orbits: many scientific missions may be characterized by

requirements associated to the average, minimum and maximum distance of the spacecraft from a target body. Because of this, it is desirable to use the semi-major axis of the orbit as an input of the design process, and look for capture conditions as a function of other variables, defining the geometry of the orbit;

- as discussed in 2.3.2, alternative approaches for the computation of the Jacobian of the physical flow should be investigated, together with their accuracy and efficiency;
- as given in Algorithm 2, two different integrations are performed: first, the 6-dimensional state is propagated until the n^{th} revolution is completed; then, the final integration time is used as an input for the integration of the variational equations. The implementation of the termination condition into the variational equations propagation would be beneficial, in terms of computational advantage;
- translating the developed toolbox, written in Matlab, in C++ would allow its implementation inside TUDAT: this would make the simulator much faster and an analysis of its performance would further help clarifying its applicability inside GNC routines;
- as previously stated, retrieving the ephemerides proved to be the bottleneck of the simulations, irrespective of the language used. A more in-depth understanding of the ephemerides retrieval may be desirable: for example, [49] presented an approach between 70 and 250 times faster then SPICE;
- following the discussion comparing Figures 5.15a and 5.15b, it may be relevant to get a global picture of the structures associated to stroboscopic strainlines: this would allow understanding to what extent they generalize the concept of invariant manifolds for more general systems;
- investigating to what extent the proposed solution allows for a robust design. Following [10], "a second challenge for these spacecraft is the large amount of uncertainty associated with the deployment state. Accordingly, a robust strategy to deliver the spacecraft [..] is desired";
- generalizing the proposed techniques to higher dimensions spaces, following, e.g., [50], or more simply the solution proposed by [17] - Section 4.2, dealing with 3D representability;
- to verify whether Stroboscopic Strainlines are Lagrangian Coherent Structures or not. For their formulation, only the third condition given in 4.5.1 has been used. Studying whether these objects verify the other conditions may be interesting, from a theoretical point of view.

A

THE SPICE SYSTEM

A.1. CONSTANTS

The main constant values, used in the simulation set-up, are given in table A.1:

Symbol	Name	Value [units]
AU	Astronomical Unit	149597870700 [m][1]
SC	Solar Constant	1367.5 [W/m^2][2]
L_S	Sun Luminosity	$3.8458 \cdot 10^{26}$ [W]
c	Speed of light	299792458 [m/s]

Table A.1: Main constants

A.1.1. NON-SPHERICAL GRAVITY COEFFICIENTS

Table A.2 contains the values of the NSG coefficients of Mars, up to degree and order 5. These values are stored in the Geosciences Node of the NASA Planetary Data System [3], and result from the analysis of data collected by the Mars Reconnaissance Orbiter.

While the listed terms lead to the main contribution to the perturbing force, it should be remembered that, when NSG has been included in the simulations, terms up to degree and order 20 have been included.

---

[3] `https://pds-geosciences.wustl.edu/mro/mro-m-rss-5-sdp-v1/mrors_1xxx/data/shadr/` (visited on 26/09/19)

n	**m**	$\bar{\mathbf{C}}_{\mathbf{nm}}$	$\bar{\mathbf{S}}_{\mathbf{nm}}$
2	0	$-8.75022092453700 \cdot 10^{-4}$	0
2	1	$4.02233330638200 \cdot 10^{-10}$	$2.30318385355200 \cdot 10^{-11}$
2	2	$-8.46330265598300 \cdot 10^{-5}$	$4.89394183216700 \cdot 10^{-5}$
3	0	$-1.18970150373000 \cdot 10^{-5}$	0
3	1	$3.80499819910100 \cdot 10^{-6}$	$2.51771177076300 \cdot 10^{-5}$
3	2	$-1.59474319237200 \cdot 10^{-5}$	$8.36239397846700 \cdot 10^{-6}$
3	3	$3.50562983603300 \cdot 10^{-5}$	$2.55713254573700 \cdot 10^{-5}$
4	0	$5.12909583013400 \cdot 10^{-6}$	0
4	1	$4.21639115821700 \cdot 10^{-6}$	$3.76326435612200 \cdot 10^{-6}$
4	2	$-9.53066952998400 \cdot 10^{-7}$	$-8.98079684180800 \cdot 10^{-6}$
4	3	$6.45685198413000 \cdot 10^{-6}$	$-1.93772122841600 \cdot 10^{-7}$
4	4	$3.08249362477000 \cdot 10^{-7}$	$-1.28730569773800 \cdot 10^{-5}$
5	0	$-1.72677024042600 \cdot 10^{-6}$	0
5	1	$4.83842156306600 \cdot 10^{-7}$	$2.12311297539500 \cdot 10^{-6}$
5	2	$-4.29817604567900 \cdot 10^{-6}$	$-1.16569544408600 \cdot 10^{-6}$
5	3	$3.31266700855500 \cdot 10^{-6}$	$2.71440977857900 \cdot 10^{-7}$
5	4	$-4.64076084741200 \cdot 10^{-6}$	$-3.38155362224900 \cdot 10^{-6}$
5	5	$-4.44926452689700 \cdot 10^{-6}$	$3.78047894095200 \cdot 10^{-6}$

Table A.2: NSG coefficients of Mars, up to degree (n) and order (m) 5.

In order to include NSG in the dynamics of the problem, a target-fixed rotating reference frame should be used. For the case of Mars, this is the IAU-Mars frame (from International Astronomical Union); this frame is available in SPICE and has been used in GRATIS for the formulation of the dynamics.
In the IAU-Mars frame:

- the +z-axis points towards the North of the Mars rotational axis;
- the +x-axis points at the prime meridian of Mars;
- the +y-axis completes the right-handed reference frame.

Finally, the reference radius of Mars is 3396 km.

A.2. EPHEMERIDES

Since, in the more general case, a RnBP is going to be considered and, because of the Restricted aspect of it, the solution of the problem can be split into two phases:

- first, the n-1 interacting bodies are considered and the general problem is (numerically) solved;
- then, the motion of the spacecraft, guided by the gravity field of the primaries, is considered.

Among others, JPL has allowed the space community not to solve the first part of the problem every time; this is possible because of the restricted nature of all the models considered. A database of ephemeris can be use to retrieve the position of the celestial bodies of interest at a certain time, in the *Earth Mean Equator and Equinox of J2000* reference frame.

A.2.1. ČEBYŠËV APPROXIMATION

Since the ephemeris are a discrete set of position and velocity, one needs to efficiently and accurately interpolate them. This is done ([51] - 3.3.3) with a least-square fit using the Čebyšëv polynomials

$$T_n(\tau) = \cos(n \cdot \arccos \tau)$$

with $|\tau| \leq 1$, that can be computed recursively by

$$T_0(\tau) = 1$$
$$T_1(\tau) = \tau$$
$$T_{n+1}(\tau) = 2\tau T_n(\tau) - T_{n-1}(\tau) \quad for n \geq 1$$

In order to make use of the behaviour of this functions in $[-1, 1]$, time is mapped to the new variable τ with

$$\tau = 2\frac{t - t_1}{t_2 - t_1} - 1$$

where $[t_1, t_2]$ define the time interval of interest.
The reason for not using a more common Taylor approximation

$$f(t) \approx \sum_{i=0}^{n-1} b_i \tau^i$$

but, instead,

$$f(t) \approx \sum_{i=0}^{n-1} a_i T_i(\tau)$$

is that the truncation error in the Taylor approach is pronounced for some values of τ and negligible for others, while, in the Čebyšëv approximation, the error is more uniformly distributed.
In [52] the procedure to generate the coefficients is shown: starting from a discrete set of position and velocity (p, v) of a certain body, a least-square problem has to be solved.

$$\begin{bmatrix} T_0(1) & T_1(1) & T_2(1) & \cdots & T_N(1) \\ \dot{T}_0(1) & \dot{T}_1(1) & \dot{T}_2(1) & \cdots & \dot{T_N}(1) \\ \vdots & \vdots & \vdots & \ddots & \vdots \\ T_0(-1) & T_1(-1) & T_2(-1) & \cdots & T_N(-1) \\ \dot{T}_0(-1) & \dot{T}_1(-1) & \dot{T}_2(-1) & \cdots & \dot{T_N}(-1) \end{bmatrix} \begin{pmatrix} a_0 \\ a_1 \\ \vdots \\ a_{N-1} \\ a_N \end{pmatrix} = \begin{pmatrix} p(1) \\ v(1) \\ \vdots \\ p(-1) \\ v(-1) \end{pmatrix}$$

The coefficients can also be found by means of Lagrange multipliers: this is because, in addition to the fact that a least-square is a minimization procedure, the initial and final values of the state are constrained to assume the exact value obtained from the integration.

A.2.2. THE SPICE SYSTEM

Developed by the Navigation and Ancillary Information Facility (NAIF) of the Jet Propulsion Laboratory (JPL), the SPICE system was built to assist engineers involved in modelling, planning and executing activities necessary, in order to conduct planetary exploration missions.[4]
This toolkit has been used to read the ephemerides in, among others, [25]. It is composed of both data files (called *kernels*) and a suite software (the SPICE Toolkit), used to read SPICE data files. The main components of the system, relevant for the goals of this work, are:

- Satellite and Planet Kernel - SPK. It mainly contains ephemerides of many objects of the solar system, as a function of time;
- a frames kernel (FK) contains specifications for the assortment of reference frames that are typically used by flight projects;
- Leap Seconds Kernel - LSK relates different time measurement systems: the TDB and the UTC;
- PCK, DSK contain informations about sizes and shapes of the bodies, together with other informations about atmosphere and gravity;
- APIs are the main components of the "SPICE Toolkit" Software. It's used to read the kernel files;
- WebGeocalc - WGC provides a GUI to a SPICE geometry engine.

A.2.3. DEVELOPMENT EPHEMERIDES

The Development Ephemerides (DE), provided by JPL, are given in the form of Čebyšëv approximations and can be retrieved with this toolkit. The DE400 series is referred to the International Celestial Reference Frame (ICRF), whose difference with the EME2000 can be neglected for the aims of this work ([51], Section 3.3.4).
They are obtained from numerical integration, taking into account, together with point-mass interactions, the perturbations from asteroids, relativistic corrections and torques. For example, the Development Ephemerides DE430 and DE431 have been used in [25]; they are described in [53]. The state of all celestial bodies is stored, as Čebyšëv polynomial coefficients, in 32-day-long segments.
DE430, including the interaction between the differential rotation of the core and the mantle, leads to difficultly defined initial conditions: for this reason the time span of this model is limited, as the error grows in backward integrations. DE431 does not take into account this effect: in this way it can cover several thousand years.

---

[4] `https://naif.jpl.nasa.gov/naif/spiceconcept.html`

BIBLIOGRAPHY

[1] E. Belbruno and J. Miller, *Sun-perturbed Earth-to-Moon transfers with Ballistic Capture,* Journal of Guidance, Control, and Dynamics 16, 770-775 (1993).

[2] F. Topputo and E. Belbruno, *Computation of weak stability boundaries: Sun-Jupiter system,* Celestial Mechanics and Dynamical Astronomy 105, 3-17 (2009).

[3] W. Koon, M. Lo, J. Marsden, and S. Ross, *Low Energy Transfer to the Moon,* Celestial Mechanics and Dynamical Astronomy 81, 63-73 (2001).

[4] J. Schoenmaekers, *Post-launch Optimisation of the SMART-1 Low-thrust Trajectory to the Moon,* 18th International Symposium on Space Flight Dynamics (2004).

[5] R. Jehn, S. Campagnola, D. Garcia, and S. Kemble, *Low-Thrust Approach and Gravitational Capture at Mercury,* 18th International Symposium on Space Flight Dynamics (2004).

[6] J. Elliot and L. Alkalai, *Lunette: a network of lunar landers for in-situ geophysical science,* Acta Astronautica 68, 1201-1207 (2011).

[7] W. Koon, M. Lo, J. Marsden, and S. Ross, *Constructing a low energy tranfer between Jovian moons,* Contemporary Mathematics 292, 129-146 (2001).

[8] F. Topputo and E. Belbruno, *Earth-Mars transfers with Ballistic Capture,* Celestial Mechanics and Dynamical Astronomy 121, 329-346 (2015).

[9] D. Mazanek, J. Brophy, and R. Merrill, *Asteroid retrieval mission concept - Trailblazing our future in space and helping to protect us from Earth impactors,* Planeraty Defence Conference (2013).

[10] A. D. Cox, K. C. Howell, and D. C. Folta, *High-energy Lunar capture via low-thrust dynamical structures,* AAS/AIAA Astrodynamics Specialist Conference, Portland, Maine (2019).

[11] C. Conley, *Low-energy transit orbits in the restricted three-body problem,* SIAM Journal on Applied Mathematics 16, 732-746 (1968).

[12] W. Koon, M. Lo, J. Marsden, and S. Ross, *Dynamical Systems and Space Mission Design,* California Institute of Technology (2000).

[13] F. Topputo, *Fast numerical approximation of invariant manifolds in the circular restricted three-body problem,* Communications in Nonlinear Science and Numerical Simulation 32, 89-98 (2016).

[14] C. Short, D. Blazevsky, K. Howell, and G. Haller, *Stretching in phase space and applications in general nonautonomous multi-body problems,* Celestial Mechanics and Dynamical Astronomy 122, 213-238 (2015).

[15] G. Haller, *A variational theory of hyperbolic lagrangian coherent structures,* Physica D 372, 31-51 (2010).

[16] M. Farazmand and G. Haller, *Computing Lagrangian Coherent Structures from their variational theory,* Chaos 22, 1-12 (2012).

[17] E. Gawlik, J. Marsden, P. D. Toit, and S. Campagnola, *Lagrangian coherent structures in the planar elliptic restricted three-body problem,* Celestial Mechanics and Dynamical Astronomy 103, 227-249 (2009).

[18] M. Manzi, *Literature Review: Lagrangian Coherent Structures in Ballistic Capture,* Delft University of Technology (2018).

[19] C. Short, *Flow-informed strategies for trajectory design and analysis,* Purdue University - Ph.D. Dissertation (2016).

[20] A. Hadjighasem, M. Farazmand, D. Blazevski, G. Froyland, and G. Haller, *A critical comparison of lagrangian methods for coherent structure detection,* Chaos: An Interdisciplinary Journal of Nonlinear Science, 27 (2017).

[21] S. Balasuriya, N. Ouellette, and I. Rypina, *Generalized lagrangian coherent structures,* Physica D: Nonlinear Phenomena 372, 31-51 (2018).

[22] Z. Luo, F. Topputo, F. Bernelli-Zazzera, and G. Tang, *Constructing Ballistic Capture orbits in the real Solar System model,* Celestial Mechanics and Dynamical Astronomy 120(4), 433-450 (2014).

[23] K. Wakker, *Fundamentals of Astrodynamics* (Delft University of Technology - Institutional Repository, 2015).

[24] B. A. Archinal and al., *Report of the IAU Working Group on Cartographic Coordinates and Rotational Elements: 2009,* Celestial Mechanics and Dynamical Astronomy, 109, 101–135 (2011).

[25] Z. Luo and F. Topputo, *Analysis of Ballistic Capture in Sun-planet models,* Advances in Space Research 56, 1030-1041 (2015).

[26] L. F. Shampine and M. W. Reichelt, *The MATLAB ODE Suite,* SIAM Journal of Scientific Computing, 18(1), 1-22 (1997).

[27] G. C. C. de Aguiar, *Earth-Mars low-thrust transfers with ballistic capture,* Delft University of Technology - M.Sc. Dissertation (2017).

[28] R. H. Battin, *Introduction to the Mathematics and Methods of Astrodynamics* (American Institute of Aeronautics and Astronautics. Reston, VA, USA, 2000).

[29] D. A. D. Tos and F. Topputo, *Trajectory refinement of three-body orbits in the real solar system model,* Advances in Space Research, 59, 2117–2132 (2017).

[30] J. D. Meiss, *Differential Dynamical Systems* (Society for Industrial and Applied Mathematics. Philadelphia, PA, USA, 2007).

[31] A. Milani and G. F. Gronchi, *Theory of Orbit Determination* (Cambridge University Press, New York, 2004).

[32] E. Belbruno, *Capture Dynamics and Chaotic Motions in Celestial Mechanics* (Princeton University Press, 2004).

[33] D. Romagnoli and C. Circi, *Earth-Moon Weak Stability Boundary in the restrected three- and four-body problem,* Celestial Mechanics and Dynamical Astronomy 103, 79-103 (2009).

[34] P. S. Silva and M. Terra, *Applicability and Dynamical Characterization of the Associated Sets of the Algorithmic Weak Stability Boundary in the Lunar Sphere of Influence,* Celestial Mechanics and Dynamical Astronomy 113, 141-168 (2012).

[35] F. García and G. Gómez, *A note on Weak Stability Boundaries,* Celestial Mechanics and Dynamical Astronomy 97, 87-100 (2007).

[36] Z. Makó, F. Szenkovits, J. Salamon, and R. Oláh-Gál, *Stable and unstable orbits around Mercury,* Celestial Mechanics and Dynamical Astronomy, 108, 357–370 (2010).

[37] N. Hyeraci and F. Topputo, *Method to Design Ballistic Capture in the Elliptic Restricted Three-Body Problem,* Journal of Guidance, Control, and Dynamics 33, 1814-1823 (2010).

[38] N. Hyeraci and F. Topputo, *The role of true anomaly in Ballistic Capture,* Celestial Mechanics and Dynamical Astronomy, 116, 175–193 (2013).

[39] P. S. Silva and M. Terra, *Diversity and Validity of Stable-Unstable Transitions in the Algorithmic Weak Stability Boundary,* Celestial Mechanics and Dynamical Astronomy 113, 453-478 (2012).

[40] G. Haller, *Lagrangian coherent structures,* The Annual Review of Fluid Mechanics 47, 134-161 (2015).

[41] C. Short, K. Howell, and X. Tricoche, *Lagrangian Coherent Structures in the Restricted Three-Body Problem,* 21st AAS/AIAA Space Flight Mechanics Meeting, New Orleans, Louisiana (2011).

[42] S. Shadden, F. Lekien, and J. Marsden, *Definition and properties of Lagrangian Coherent Structures from finite-time Lyapunov exponents in two-dimensional flows,* Physica D 212, 271-304 (2005).

[43] V. Szebehely, *Theory of Orbits: The Restricted Problem of Three Bodies* (New York: Academic Press, 1967).

[44] D. H. Kelley, M. R. Allshouse, and N. T. Ouellette, *Lagrangian coherent structures separate distinct regions in fluid flows,* Physical Review, 88, 1-4 (2013).

[45] E. Belbruno, M. Gidea, and F. Topputo, *Weak Stability Boundary and Invariant Manifolds,* SIAM Journal on Applied Dynamical Systems 9, 1061-1089 (2010).

[46] G. Haller and G. Yuan, *Lagrangian Coherent Structures in two-dimensional turbulence,* Physica D, 147, 352-370 (2000).

[47] X. R. Roca, *Computation of Lagrangian Coherent Structures with Application to Weak Stability Boundaries,* Politecnico di Milano - B.Sc. Dissertation (2015).

[48] A. S. Parkash, *Application of Lagrangian Coherent Structures to the computation and understanding of ballistic capture trajectories,* Delft University of Technology - M.Sc. Dissertation (2019).

[49] N. Arora and R. P. Russell, *A fast, accurate, and smooth planetary ephemeris retrieval system,* Celestial Mechanics and Dynamical Astronomy, 108, 107–124 (2010).

[50] F. Leiken, S. C. Shadden, and J. E. Marsden, *Lagrangian coherent structures in n-dimensional systems,* Journal of Mathematical Physics, 48, 1-19 (2007).

[51] O. Montenbruck and E. Gill, *Satellite Orbits: Models, Methods, and Applications* (Springer-Verlag. Berlin, Germany, 2001).

[52] X. Newhall, *Numerical Representation of Planetary Ephemerides,* Celestial Mechanics 45, 305 (1988).

[53] W. M. Folkner and al., *The Planetary and Lunar Ephemerides DE430 and DE431,* Technical report, IPN Progress Report 42-196 (2014).